2014

Boundary Effects and Shear Thickening of Colloidal Suspensions; A Study based on measurement of Suspension Microstructure

Mukundadura Tharanga Damayantha Perera
Lehigh University

Boundary Effects and Shear Thickening of Colloidal Suspensions; A study based on measurement of Suspension Microstructure

By

M.Tharanga D Perera

Presented to the Graduate and Research Committee
of Lehigh University
in Candidacy for the Degree of
Doctor of Philosophy
in
Chemical Engineering

Lehigh University
September 2014

Certificate of Approval

Approved and recommended for acceptance as a dissertation in partial fulfillment of the requirements of the degree of Doctor of Philosophy.

_____
Date

_____
James F. Gilchrist, Ph.D.
Dissertation Advisor

_____
Accepted Date

Committee Members:

_____
James F. Gilchrist, Ph.D.
Committee Chair

_____
Anthony J. McHugh, Ph.D.
Committee Member

_____
Mark A. Snyder, Ph.D.
Committee Member

_____
Jeffrey Morris, Ph.D.
Committee Member

Acknowledgements

I owe my deepest gratitude to Professor James F. Gilchrist for his teaching, inspiration and guidance throughout my research work at Lehigh University. Without him, this thesis will never become possible. His guidance and advice not only limited to my research, but also my career and other extracurricular activities in my life here at Lehigh. Thank you! I would also like thank my committee members, Professor Anthony J. McHugh, Professor Mark A. Snyder and Professor Jeffrey F. Morris from the City College of New York, for their insight and guidance in my research.

My research work at Lehigh had many challenges, especially when I was a first year doctoral student. I would like to thank several people in training me and helping me understand principles behind research work; Dr. Bu Xu for training me and helping me understand all the principles behind experiments, microchannels, rheology when I joined the Gilchrist lab back in September 2010. The success behind most of my experiments should go to Dr. Bu Xu for his valuable advice when I was a first year student. Dr. Pao Kummnorkaew for his valuable advice as a Post Doctoral researcher in the Gilchrist lab, in ways to keep an active research eye when performing research work in the lab. In addition, my lab mates were of great help in assisting me with work related to SEM characterization, particle synthesis as well as motivating me and always making sure that we also had a little fun throughout the time here at Lehigh. A Big thanks to Dr. Alex Weldon, Tanyakorn Muagnapoh, Midhun Joy, Kedar Joshi and Yajun Ding. I would also like to thank Dr. Hasan Zerze and David Gildea for helping

me with the use of the Rheometer and Midhun Joy for the computer programming and coding work especially related to the work presented in Chapter 3 of this thesis.

The Faculty in the Department of Chemical Engineering especially the Professors who taught me the First year courses in the PhD program owe my thanks for making me a successful student. Professors Jeetain Mittal, Anand Jagota, Mayuresh Kothare, Phillip Blythe, Mark Snyder and Manoj Chaudhury are to name a few of the teachers who taught me the fundamental coursework that benefitted me in my research work. Also, thanks to the Chemical Engineering Staff including Barbara Kessler, Janine Jekels, Tracey Lopez, Paul Bader and John Caffrey.

Finally, I am grateful to my Father, Mother, my sisters and brother-in-laws for their everlasting support and love in my life. Thank you!

Table of Contents

List of Tables ix

List of Figures x

Abstract 1

Chapter 1: Introduction .....

1.1 Summary 3

1.2 Motivations 5

1.3 Suspensions Rheology & Microstructure 6

1.4 3D Confocal Imaging 16

1.4.1: Microstructure study in Simple Hydrodynamic Flows 21

1.4.2: Effect of Electrostatics on Microstructure 28

Chapter 2: Experimental Methods and Techniques .....

2.1: Fabrication of Microchannels 36

2.2: Cleaning of Glass Slides with Piranha Solution 39

2.3: Particle Synthesis 39

2.4: Suspension Preparation 42

2.5: Imaging Protocol 44

2.6: Particle Image Velocimetry 47

2.7: Particle Tracking 49

2.8: Data Analysis 51

2.9: Rheometry 52

Chapter 3: Hydrocluster Analysis of Suspensions .....

3.1: Introduction and Previous Work 53

3.2: Results and Discussion 56

3.2.1: Suspension Microstructure 56

3.2.2: Investigation of Particle Clustering and Effects on Viscosity 60

3.2.3: Probability Distribution of Cluster Size 67

3.2.4: Angular Dependence of particles constituting to a cluster 70

3.3: Conclusions 76

Chapter 4: Effect of Smooth & Rough Boundaries on Suspension Microstructure .....

4.1: Introduction and Background 78

4.2: Results & Discussion 84

4.2.1: Experimental Technique 84

4.2.2: Suspension Microstructure 87

4.2.3: Viscometric Calculations 91

4.2.4: Lubrication Slip Layer 97

4.3: Conclusions 102

Chapter 5: Microstructure of Suspension flow in a Well Structured micro-porous medium

5.1: Introduction and Background 103

5.2: Results & Discussion 105

5.2.1: Experimental Technique 105

5.2.2: Suspension Microstructure in upstream and downstream flows 107

5.2.3: Suspension Microstructure between the posts 115

5.3: Conclusions 120

Chapter 6: Summary and Future Directions .....

6.1: Summary 121

6.2: Future Directions 124

Bibliography 128

Vita 137

List of Tables

Table 3.1 The bond order parameter, Ψ_6 obtained for the different Pe number experiments. The value remains constant regardless of the Pe in our experiments. 65

Table 4.1 Estimating the lubrication thickness, δ, from experimental data. V_s correspond to the slip velocity, η_S the solvent viscosity and σ_p the particle stress estimated by the addition of the Hydrodynamic and Brownian stress contributions..... 98

List of Figures

Figure 1.1 The viscosity of a colloidal latex dispersion, Laun (1984). Suspension structure changes with applied shear stress from equilibrium, shear thinning and shear thickening. This effect is demonstrated in this figure at different volume fraction of particles.....8

Figure 1.2 (a) Shear Induced particle migration as seen on a confocal microscope image. The concentration of particles is higher at the center of the channel than near the walls of the channel due to shear induced particle migration. (b) Velocity profile for shear induced particle migration. The velocity is greatest at the center of the channel due to shear induced particle migration; Lyon and Leal (1998). 11

Figure 1.3 Suspension structure for increasing *Pe* (Foss and Brady, 2000). An anisotropic ring starts forming along the velocity gradient velocity plane as Pe increases.....17

Figure 1.4 Comparison between experimental and simulation g(r) plots, (a) original experimental results show signature anisotropy but lack in detail in microstructure; (b) modified experimental results compared with simulation studies. Experimental results closely agree with simulation results from Kulkarni & Morris 20

Figure 1.5 Effect of hydrodynamic force on microstructure. An isotropic ring starts to form with reducing hydrodynamic force. The appearance of a second and third outer ring corresponds to the reducing hydrodynamic forces as well (Xu & Gilchrist 2014). 21

Figure 1.6 Relative viscosity vs. *Pe*, rescaled. Red symbols represent experimental data while the black symbols represent simulation data from Foss & Brady (2000) Figure was adapted from Xu & Gilchrist (2014). 24

Figure 1.7 First Normal Stress Difference vs. *Pe*, rescaled. Red symbols represent experimental data while the black symbols represent simulation data from Foss & Brady (2000) Figure was adapted from Xu & Gilchrist (2014).....26

Figure 1.8 Second Normal Stress Difference vs. *Pe*, rescaled. Red symbols represent experimental data while the black symbols represent

simulation data from Foss & Brady (2000) Figure was adapted from Xu & Gilchrist (2014)..... 27

Figure 1.9 Plot showing how zeta potential varies with pH for a system of colloidal particles..... 29

Figure 1.10 Effect of debye length on microstructure. When the debye length is increased from 8 nm to 30 nm the structure is being dissipated and attenuated. When the debye length is further increased a more symmetric and ordered structure can be observed 30

Figure 1.11 Effect of zeta potential on microstructure at k^{-1}= 8 nm. At this debye length you see the structure getting dissipated based on the g(r) plots 32

Figure 1.12 Effect of zeta potential on microstructure at k^{-1}= 80 nm. A more structured ring is formed when the pH is increased from 6 to 8. 33

Figure 2.1 (a) Side view of the typical microchannel. The PDMS microchannel is attached with a glass coverslip at the bottom and has a flow inlet and outlet. This is a straight channel with dimensions of 500 µm X 94 µm X 4000 µm (W x H x L) utilized to achieve constant shear rate profiles when flowing. This channel was used for the studies of chapter 3 and 4 of this thesis.
(b) Channel that contains a porous network structure. The silicon wafer that contained this patterned structure was obtained from Professor Xuanghong Cheng's Laboratory at Lehigh University. This channel was used for the study described in Chapter 5 of this thesis. 38

Figure 2.2 Scanning Electron Microscopy (SEM) Images of 1 micron Fluorescent Silica particles. The particles are monodisperse and impurities have been washed away (images taken before washing). 41

Figure 2.3 Set up of the confocal microscope platform. Compressed nitrogen was used via the electropneumatic converter to drive the suspension using pressure-driven flow (for experiments described in Chapters 4 and 5). A syringe pump set up was used to perform experiments described in Chapter 3 of this thesis.. 43

Figure 2.4 Stop flow scan procedure displayed with time. The suspension was flowed for a few minutes till it reached a certain velocity and

then the flow was arrested and the scan was performed. The blue arrows show the points at which the scans were taken 45

Figure 2.5 (a) Example of a Z-stack image capture series. The dimensions of the images taken are shown. Images were taken every 0.1 μm at 100 fps for the velocimetry and stop flow scan procedures. (b) This image shows a typical fluorescent image of particles as seen on the confocal microscope. 46

Figure 2.6 Velocity profile obtained of the suspension by comparing displacement of particles in IDL. Shear rate can be obtained by calculating the gradient of velocity over the distance from the bottom layer. The shear rate profile is also shown in this figure..... 48

Figure 2.7 A 3D reconstruction of particles obtained using the particle tracking coordinates from IDL. The image above shows a true 3D rendering of particle structure similar to if it was flown in the actual microchannel..... 50

Figure 3.1 Velocity profiles of particles flowing in the suspension from 0 to 20 μm away from the channel bottom (wall). The velocity profiles shown correspond to different shear rates and thus have been plotted for different *Pe* numbers. Symbols span data for *Pe* of 14, 51, 103, 166, 230, 310 and 350 as shown. 57

Figure 3.2 g(r) plots for the y vs. x, z vs. x and y vs. z planes for *Pe*= 350, 310, 230, 166, 103, 51 and 14. The pair distribution functions shown are averaged between 6 μm to 12 μm from the channel bottom..... 58

Figure 3.3 A flowing particle suspension with a few Hydroclusters identified (in red*)* 60

Figure 3.4 Number of clusters constituting to 5 or more particles in a cluster (N) plotted against *Pe*. The results suggest an exponential increase of clusters that fits an exponential profile of N= 8.7577 exp (0.0056*Pe)* 62

Figure 3.5 Relative viscosity (η_r) plotted against *Pe*. The graph shows a shear thinning and thickening trend in which you see the shear thickening to start at a *Pe*~50 63

Figure 3.6 Brownian contribution to the relative viscosity (η_B) plotted against *Pe*.....66

Figure 3.7 Probability of Cluster size distributions for *Pe* (a) 350, (b) 310, (c) 230, (d) 166, (e)103, (f) 51, (g) 14.....68

Figure 3.8 Angular dependence of clusters defined with coordinates as shown. The angle between the x and y planes will be defined as Ø while the angle between the x and z planes will be defined as θ.....70

Figure 3.9 Probability of finding a particle having an angle Ø for all particles constituting the $N \geq 5$ clusters. (i) and (ii) represent the results for Pe = 350, 310, 230, 166, 103, 51 and 14.....73

Figure 3.10 Probability of finding a particle having an angle θ for all particles constituting the $N \geq 5$ clusters. (i) and (ii) represent the results for Pe = 350, 310, 230, 166, 103, 51 and 14.....75

Figure 4.1 Structure and particle chaining in the flow direction observed near the walls. The g(r) plots correspond to 4,6,8 and 10 μm away from the wall. The plots correspond to (a) Glycerine-Water Suspension at $\dot{\gamma}$=9 s^{-1}, (b) DMSO suspension at $\dot{\gamma}$=12 s^{-1}, (c) PAM Dissolved in Glycerine-Water at $\dot{\gamma}$=20 s^{-1} and (d) λ-DNA in DMSO at $\dot{\gamma}$=25 s^{-1}.....82

Figure 4.2 Comparison of Smooth and Rough Walls in the PDMS Microchannel. A Smooth Wall is characterized as a plain glass slide while a rough wall contains a monolayer of 1 μm Silica spheres deposited on to the glass slide.....85

Figure 4.3 Velocity profiles of the flowing suspension for two different shear rates for the smooth and rough boundaries as a function of distance from channel bottom (y) normalized by particle diameter (2a).....86

Figure 4.4 g(r) plots in the y vs. x ($(\nabla v$ vs $v)$ plane. Plots correspond to (a) $\dot{\gamma}$ = 2-3 s^{-1} (*Pe*~2), (b)) $\dot{\gamma}$ = 16-18 s^{-1} (*Pe*~20) for both the smooth and rough walls cases.....89

Figure 4.5 g(r) plots in the y vs. z ($(\nabla v$ vs ∇ x $v)$ plane. Plots correspond to (a) $\dot{\gamma}$ = 2-3 s^{-1} (*Pe*~2), (b)) $\dot{\gamma}$ = 16-18 s^{-1} (*Pe*~20) for both the smooth and rough walls cases.....90

Figure 4.6 Scaled relative viscosity plot. The data are plotted for both smooth and rough boundaries as a function of normalized distance away from the boundary 92

Figure 4.7 Scaled First Normal Stress difference. The data are plotted for both smooth and rough boundaries as a function of normalized distance away from the boundary 93

Figure 4.8 Scaled Second Normal Stress Difference. The data are plotted for both smooth and rough boundaries as a function of normalized distance away from the boundary 94

Figure 4.9 Scaled relative viscosity plot. The data are plotted for smooth boundaries for *Pe* =14, 51,103, 166, 230, 310 and 350. The data are plotted as a function of normalized distance away from the boundary 99

Figure 4.10 Scaled First Normal Stress Difference. The data are plotted for smooth boundaries for *Pe* =14, 51,103, 166, 230, 310 and 350. The data are plotted as a function of normalized distance away from the boundary 100

Figure 5.1 (a) Side view of the microchannel with porous network. The cylindrical pores are of 94 μm height with a 780 μm diameter. The distance between two pores is roughly 80 μm; (b) Top view of porous network highlighting the Regions of Interests (ROIs) investigated in this study 106

Figure 5.2 g(r) plots in the y vs. x plane for the upstream and downstream flow cases. The volume fraction of the suspension is low and therefore do not observe much structure. The extension of the flow component is negative before approaching the obstacle and is positive downstream 109

Figure 5.3 g(r) plots in the y vs. x plane for the upstream flow case. The volume fraction of the suspension is high and we observe a change in structure as the flow progresses toward the obstacle. The extension of the flow component is negative upstream and is positive in the downstream flow case 110

Figure 5.4 g(r) plots in the y vs. x plane for the upstream and downstream flow cases. The regions of interest in this figure are around the

obstacle. The volume fraction of the suspension is low and therefore do not observe much structure 113

Figure 5.5 g(r) plots in the y vs. x plane for the upstream and downstream flow cases. The regions of interest in this figure are around the obstacle. The volume fraction of the suspension is high and we observe more structure closer to the post than away 114

Figure 5.6 Region investigated between the two posts is shown in red. The approximate directions of the flow streamlines are shown. At this point, we can assume the extensional rate to be zero 115

Figure 5.7 g(r) plots representing the three different planes for the structure between the two posts 116

Figure 5.8 Scaled Relative Viscosity (ηr) and First Normal stress difference (N_1) plotted as a function of distance from wall (post) 119

Figure 6.1 Fluorescent Lambda DNA observed near the channel walls of the confocal microscope. The DNA observed closer to the walls always had a stretched state as seen in this figure. 126

Figure 6.2 Fluorescent Lambda DNA observed in the center of the channel of the confocal microscope. The DNA observed in the center of the channel always had a coiled state as seen in this figure. 127

Abstract

Microstructure is key to understanding rheological behaviors of flowing particulate suspensions. During the past decade, Stokesian Dynamics simulations have been the dominant method of determining suspension microstructure. Structure results obtained numerically reveal that an anisotropic structure is formed under high Péclet (Pe) number conditions. Researchers have used various experimental techniques such as small angle neutron scattering (SANS) and light scattering methods to validate microstructure. This work outlines an experimental technique based on confocal microscopy to study microstructure of a colloidal suspension in an index-matched fluid flowing in a microchannel. High resolution scans determining individual particle locations in suspensions 30-50 vol % yield quantitative results of the local microstructure in the form of the pair distribution function, g(r). From these experimentally determined g(r), the effect of shear rate, quantified by the Péclet number as a ratio of shear and Brownian stress, on the suspension viscosity and normal stress follow that seen in macroscopic rheological measurements and simulations.

It is generally believed that shear thickening behavior of colloidal suspensions is driven by the formation of hydroclusters. From measurements of particle locations, hydroclusters are identified. The number of hydroclusters grows exponentially with increasing *Pe*, and the onset of shear thickening is driven by the increase in formation of clusters having 5-8 particles. At higher *Pe*, we notice the emergence of 12 or more particle clusters. The internal structure of these hydroclusters has been investigated, and

there is some evidence that particles internal to hydroclusters preferentially align along the 45° and 135° axis.

Beyond observations of bulk suspension behavior, the influence of boundaries on suspension microstructure is also investigated. Experiments were performed for suspensions flowing over smooth walls, made of glass coverslips, and over rough walls having a high density coating of particles. These results show that there is more order in structure near smooth boundaries while near rough boundaries the structure is similar to that found in the bulk. The relative viscosity and normal stress differences also indicate that boundaries have an effect up as far as 6 particle diameters away from the boundary. Finally, we investigate the microstructure evolvement in a model porous medium and notice that such boundary effects come into play in such real process flows.

The confocal microscopy technique also provides us with the advantage of measuring structure in real process flows. We have investigated how the microstructure evolves upstream and downstream in a porous medium. We notice more structure in a high volume fraction suspension and notice anisotropic behavior at regions where shear from the wall of the posts dominate. In other cases, a mixed flow behavior is observed due to collisions between pore surfaces and other particles resulting in a deviation from flow streamlines.

Chapter 1

Introduction

1.1: Summary

This doctoral thesis serves to present research and findings of suspension microstructure and rheology based on experimentally obtained results utilizing confocal laser scanning microscopy. Simulation studies, specifically Stokesian Dynamics Simulation Methods have been dominant in predicting microstructure and rheology of flowing suspensions for the past decade. Not until recently, have researchers been able to establish a viable technique to understand flowing suspensions experimentally. This thesis will present the techniques and methods used (Chapter 2) and analyze the mechanism behind shear thickening based on hydrocluster formation (Chapter 3). We also emphasize the importance of wall effects in confined systems of flows (Chapter 4). The main benefit of using confocal Laser Scanning Microscopy is the fact that you can use this technique to measure structure of real process flows such as flows in porous media (Chapter 5) experimentally. Thus, we are able to track how the structure evolves locally and understand the mechanism behind such process relevant flows. It is also possible to observe how wall effects come into play in such real process flows (Chapter

5). Finally, future enhancements, directions, and areas of interest are summarized (Chapter 6).

1.2: Motivations

Suspension flows are common in natural processes such as sediment transport in rivers and blood flow, bioengineering analyses of cellular and DNA material, and industries including coating, coal, food and pharmaceuticals.

A detailed understanding of particle-particle hydrodynamic interactions is necessary as it impacts suspension process design for transport processes such as flow, mixing, and separation. Behavior of suspensions deviates from that of Newtonian fluids, for instance, shear thinning and thickening behavior of suspensions at moderate to high volume fraction of solids. Paints, cement and soft body armor are such suspensions whose rheology changes when such colloidal fluids experience shear stress. In addition, when considering suspension flow in non-uniform shear, particles can migrate from regions of high shear to regions of low shear to balance the normal stresses due to hydrodynamic interactions and formation of suspension microstructure. A complete three dimensional (3D) particle level data is necessary in order to understand the rheology and microstructure of a suspension. Rheological behavior as well as microstructural anisotropies responsible for sheared suspensions have been studied numerically by Brady and Morris (1997) and others and until recently these results has not been a detailed experimental confirmation of these results.

1.3: Suspensions Rheology and Microstructure

Rheology, as a newly emerged science in the twentieth century, studies the deformation and stress in materials displaying both fluidity and solidity. Addition of solid particles to a fluid makes a colloidal suspension and is characterized by several rheological parameters based on its deformation and stress. The effective viscosity, η, is defined by the ratio of shear stress, τ , to shear rate, $\dot{\gamma}$, and is strongly coupled to the particle properties, the volume fraction of solids, ϕ, and the flow.

$$\eta = \frac{\tau}{\dot{\gamma}}$$

The particle-particle interactions in suspensions can be of purely hydrodynamic solid body behavior, acting as hard spheres, or dominated by electrostatic interactions causing attraction or repulsion. For an ideal suspension with randomly distributed monosized hard spheres at very low ϕ, suspension viscosity follows Einstein's law of viscosity (Einstein, 1906, 1911). Einstein's law of viscosity is defined as;

$$\frac{\eta}{\eta_0} = 1 + \frac{5}{2}\phi$$

where η_0 is the fluid viscosity. Suspension viscosity deviates from Einstein's theory due to multi-body hydrodynamic interactions as a result of increase of particle concentration. The following empirical correlations were shown by Krieger (1972) relating viscosity to particle volume fraction at the zero shear rate

$$\frac{\eta}{\eta_0} = \left(1 - \frac{\phi}{0.57}\right)^{1.50}$$

And at the high shear limit

$$\frac{\eta}{\eta_0} = \left(1 - \frac{\phi}{0.68}\right)^{1.82}$$

Where $0 \leq \phi \leq 0.50$. All flows considered in this thesis is essentially inertia-free where, the Reynolds number,

$$Re = \frac{\rho a^2 \dot{\gamma}}{\eta} \ll 1$$

where ρ is the density of the fluid and a is the particle radius, and the Péclet number (the ratio of advection to diffusion time scales),

$$Pe = \frac{a^2 \dot{\gamma}}{D_0}$$

where D_0 is the short-time diffusivity (Bossis and Brady 1985);

$$D_0 = \frac{kT}{6\pi\eta_0 a}$$

Shear thinning/thickening behavior of suspensions is a result of suspension microstructure and is directly related to the Péclet number, *Pe*, in the system. At low *Pe* the equilibrium structure gets distorted by the flow and the suspension starts to shear thin. At high *Pe*, the shear stress is much larger than that of Brownian motion and shear thickening behavior is found at moderate to high ϕ. The following figure (Figure 1.1) shows rheological data of a colloidal latex dispersion from Laun (1984). The figure was adapted from Wagner and Brady (2009).

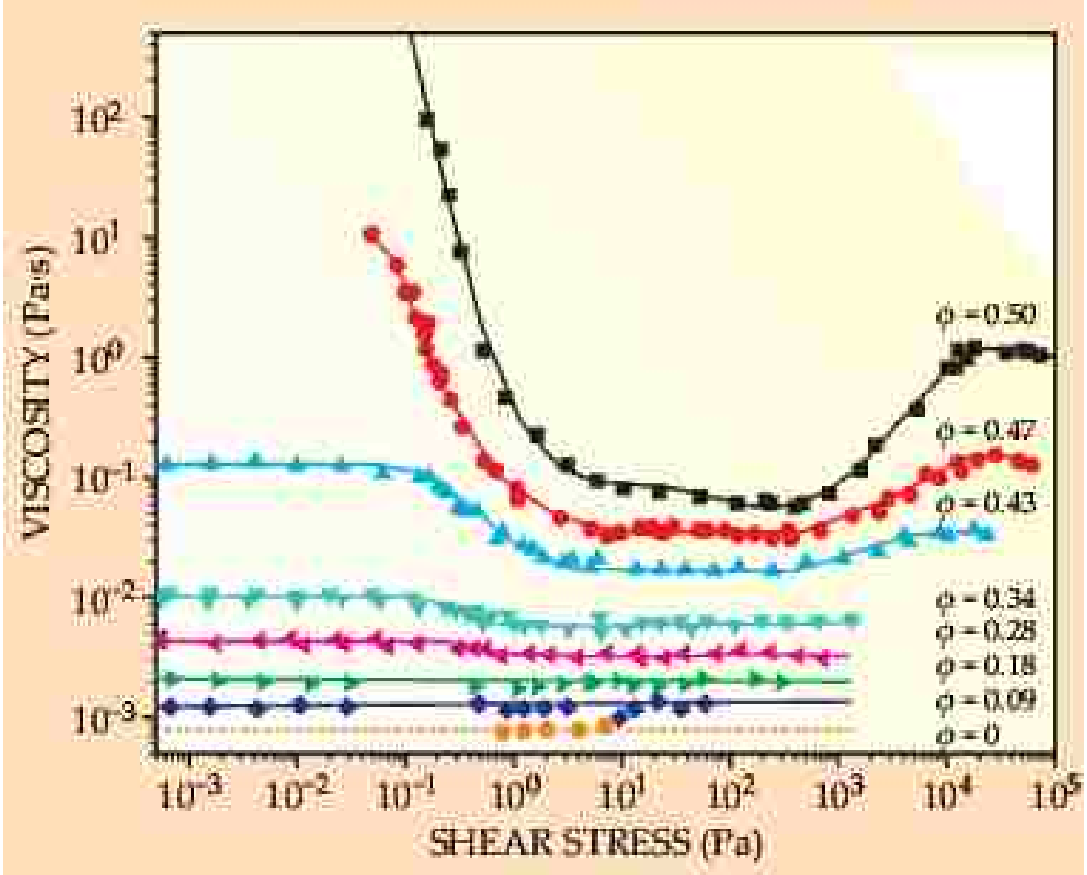

Figure 1.1: *The viscosity of a colloidal latex dispersion, Laun (1984). Suspension structure changes with applied shear stress from equilibrium, shear thinning and shear thickening. This effect is demonstrated in this figure at different volume fraction of particles*.

The addition of colloidal particles to a liquid such as water results in the increase of the liquid's viscosity, and also displays non-Newtonian behavior. In figure 1, the increase in volume fraction of latex particles in each dispersion increases both the shear thinning and thickening. According to the figure, a critical yield stress must be achieved in order to induce flow in a dispersion with a high particle concentration. Beyond this critical stress, the fluid's viscosity decreases (shear thinning). At yet higher stress, shear thickening is evident.

This behavior can be explained in terms of suspension structure as well. At low shear rates, the microstructure corresponds to an equilibrium microstructure. When the shear rate is introduced, it is hypothesized that particles form layers that start sliding over each other. This reduces stress resulting in shear thinning behavior. At higher shear rate, these layers dissipate and the microstructure forms significant anisotropy. It is hypothesized that a small fraction particle dominates the stress because of their local proximity and orientation. These so-called hydroclusters result in the dramatic shear thickening seen. Hydroclusters (Bossis and Brady 1985, Bender & Wagner 1995;1996, Melrose et al. 1996, Brady & Bossis 1998, Phung & Brady 1996) are particles in near contact where hydrodynamic lubrication between particles distributes stress over many particle diameters. Hydroclusters are dynamic by nature, and the growth of these clusters to length scales comparable to the system size can result in jamming and periodic flow.

Shear Induced particle migration is also a well-studied phenomenon that has received significant attention for the past two decades. Studies of shear-induced

migration have appropriately focused on various viscometric flows, e.g. Couette flow: Leighton & Acrivos (1987b); Phillips et al. (1992), flow between parallel plates: Chow et al. (1994), pressure-driven channel flows: Phillips et al. (1992); Lyon & Leal (1998), and oscillatory shear flows: Gadala-Maria & Acrivos (1980); Bricker & Butler (2006). It is widely seen as a breakdown in the homogeneity of the system, departing from proper kinematic flows for rheology. The microstructure depends on *Pe* and ϕ_{bulk} and generates normal stresses. In nonlinear shear flows, to balance normal stresses, ϕ_{bulk} must repartition with regions of different shear. Thus, particles migrate from high shear regions to low shear regions. This results in a higher particle concentration near the center of the channel and a lower concentration near the walls of a channel as shown in Figure 1.2.

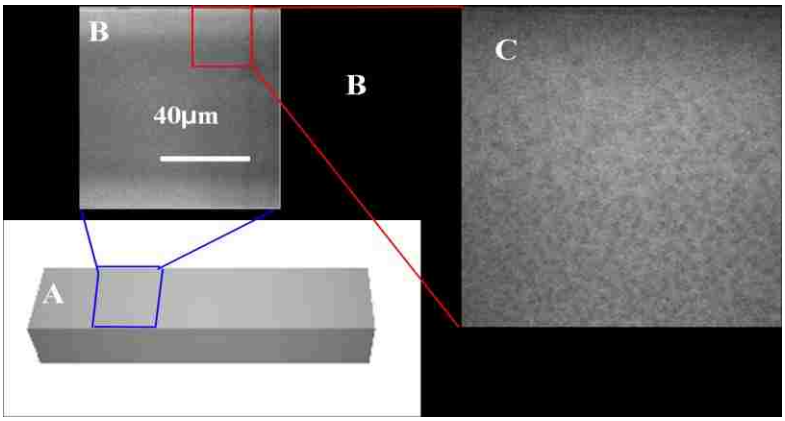

(a)

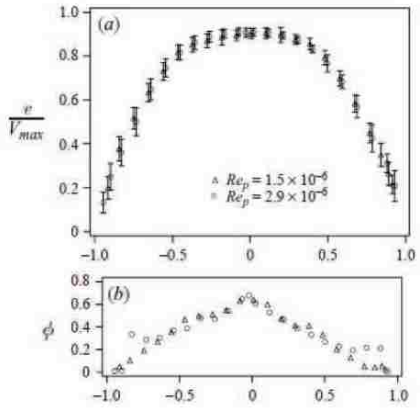

(b)

Figure 1.2: *(a) Shear Induced particle migration as seen on a confocal microscope image. The particle concentration is higher at the center of the channel than near the walls due to shear induced particle migration; (b) Velocity profile for shear induced migration. The velocity is the greatest at the center of the channel : Lyon and Leal (1998)*

In order to further understand shear induced particle migration, efforts have been made to relate suspension structure to stresses using Stokesian dynamics simulations (Brady & Bosis, 1988). Stokesian Dynamics simulations are used to study suspension microstructure to understand the rheology of suspensions as well as to give answers to phenomena such as shear induced particle migration and stresses in the system (Foss and Brady (2000), Sierou and Brady (2002), Morris and Katyal (2002), Kulkarni and Morris (2009), Stickel, Phillips and Powell (2006, 2007).

Simulations using Stokesian Dynamics methods seemed to be the best means of obtaining detailed information about suspension structure and stress information. However, few experimental results are available on suspension microstructure and these experimental results do not have sufficient resolution to determine structure. Light scattering (Husband & Gadala-Maria 1987, Parsi & Gadala Maria 1987), laser sheet imaging methods (Rampall et al. 1997) and Small Angle Neutron scattering (Bender et al. 1996, Kalman 2010, Hoffman 1998) were some of the methods been employed to obtain suspension structure of such systems. The main drawbacks of these experimental techniques were that the set up could be very complex, limited to ideal flows and most importantly could not match the detail obtained through simulation methods. Recently, Gao et al 2010 used an experimental technique based on 3D Laser Scanning Confocal Microscopy to obtain particle locations experimentally and then determine the suspension microstructure. Therefore, this thesis will be based on observing suspensions microstructure based on experimentally obtained particle locations data utilizing Confocal Microscopy. Prior to proceeding with the Confocal Microscopoy technique,

the next section of this introduction will be discussing the physics behind suspensions rheology.

The index measure of the microstructure of a suspension of a monodisperse spheres is the pair distribution function, defined as

$$g(\mathbf{r}) = \frac{P_{1|1}(\mathbf{r})}{n}$$

where P1|1(r) is the conditional probability of finding a particle at position r with respect to a reference particle, and n is the particle number density. P1|1(r) is formally obtained by integrating the N- particle configuration probability $P_N(x^N)$ over the center of mass coordinate for the pair and the coordinates of the remaining particles $x_3 \ldots x_N$. The information captured directly by g(r) provides a description of the symmetry, localization, and spatial persistence of the correlation of particle position about a body of known position. Structural asymmetry in the flow direction was shown to lead to non-Newtonian normal stresses with g(r) showing to have a boundary layer in the regions of compression where particles are in the approach due to the shear flow. Since the rheological properties are affected in a qualitative fashion by the structural deformation caused by flow of a suspension, it is important to understand the structure-stress relationship when a suspension is subjected to flow.

For Stokesian Dynamics simulations, the method uses a force balance for the solution of particles in zero-Reynolds number fluid flow situations. The method begins from the Langevin Equation which considers a hydrodynamic force component arising from the motion of particles, Brownian force component from the Brownian diffusion

as well as an interparticle force component that includes colloidal forces such as those arising from gravitational and electric fields.

Let us consider the equations considered in Stokesian Dyanamics (Brady 1993, Morris & Katyal 2002, Brady and Morris 1997) in order to demonstrate the underlying physics behind stresses of suspension flow. The bulk stress in a suspension can be regarded as;

$$\Sigma = -\langle p \rangle I + 2\eta \langle E \rangle + \langle \Sigma_{\mathrm{P}} \rangle$$

Where $\langle p \rangle$ is a constant setting the level of pressure and $2\eta\langle E \rangle$ is the deviatoric stress contribution from the fluid, with η being the viscosity of the suspending fluid. The particle contribution to the stress can be written as;

$$\langle \Sigma_p \rangle = -nkTI + n(\langle S^H \rangle + \langle S^B \rangle + \langle S^P \rangle)$$

Where $\langle S^H \rangle$, $\langle S^B \rangle$ and $\langle S^P \rangle$ are the Hydrodynamic, Brownian and interparticle force stresslets respectively. Detailed information about these stresslets can be found in Brady (1993) and Foss and Brady (2000). Here, *-nkTI* is just the isotropic stress associated with the thermal kinetic energy of the Brownian particles, I is the isotropic tensor and *n* is the number density of the particles. There are three contributions to the bulk stress. (a) a mechanical or contact stress transmitted by the fluid due to shear flow, S^H; (b) a stress due to the interparticle forces, S^P; (c) contribution from Brownian, S^B.

In addition, the viscosity of a suspension will have contributions from the Hydrodynamic and Brownian components as well. In steady shear flow, the viscosity of a suspension is related to the (x,y) components of the bulk stress and rate of strain in the following manner (Foss and Brady 2000),

$$\eta_r = \frac{\Sigma_{xy}}{2\eta E_{xy}}$$

And the individual hydrodynamic (S^H) and Brownian (S^B) contributions to the relative viscosity are denoted by η_r^H and η_r^B respectively.

$$\eta_r = 1 + \eta_r^H + \eta_r^B$$

Where the 1 is the solvent contribution.

We are able to obtain viscometric information of a flowing suspension via the suspension microstructure. Therefore, in Section 1.4, let me demonstrate how Confocal Imaging is used to obtain microstructure information from particle tracking data.

1.4: 3D Confocal Imaging

Confocal microscopy provides a useful method to obtain particle locations experimentally and deduce the suspension structure. This technique has been refined to obtain near simulation-level detail of suspension microstructure. Direct comparison of experimental results on suspensions where electrostatic interactions are mostly screened and hydrodynamics interactions dominate to Stokesian Dynamics simulations are used to confirm this technique .

Previous studies show that an anisotropic structure is formed with increasing *Pe* number of a suspension (Foss & Brady 2000). In addition, the structure of suspension under deformation has a greater number of nearest-neighbor interactions along the compression direction of the flow than the extensional axis. See Figure 1.3.

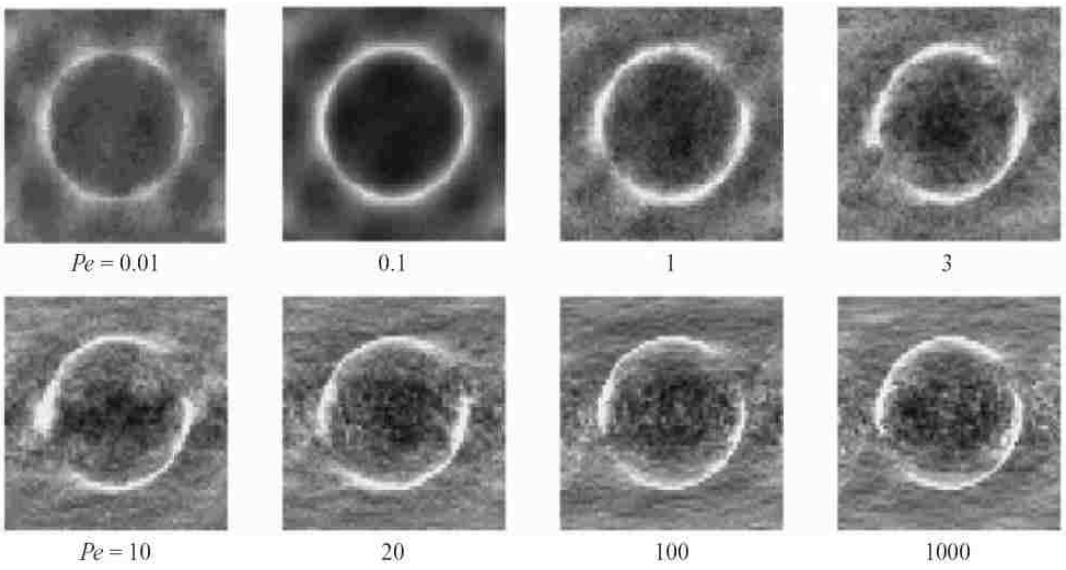

Figure 1.3: *Suspension structure for increasing Pe (Foss and Brady, 2000). An anisotropic ring starts forming along the velocity gradient-velocity plane as Pe increases.*

A comparison of our experimental results with simulation results are shown in Figure 1.4. Figure 1.4 (a) shows a comparison of our original experimental results with simulation. We were able to capture the signature anisotropy evident in the y vs. x plane, but the detail from experiments could not match with simulation results much closely. Over the years, we were able to modify our experimental technique (See Chapter 2) to improve the detail of our results as shown in Figure 1.4 (b). The experimental results demonstrate a high degree of agreement with simulation results by Foss & Brady, and Kulkarni & Morris under similar conditions. Not only is the signature anisotropy clearly seen in the experiment, but such details as vague tails near the opening of the innermost ring are also matched between the two different approaches. The experiment suggests stronger correlation along the flow direction with two red dots around 0° and 180° directions. Both obtained a stronger correlation along z- than x-direction in the first ring on x-z plane and a uniform first ring on z-y plane, though the experiment reveals more layering along the y-direction. Multiple reasons may give rise to these disagreements, including mismatch of *Pe* and ϕ in the two separate studies, near wall effect in experiment and simplifications made in the simulation regarding particle interactions.

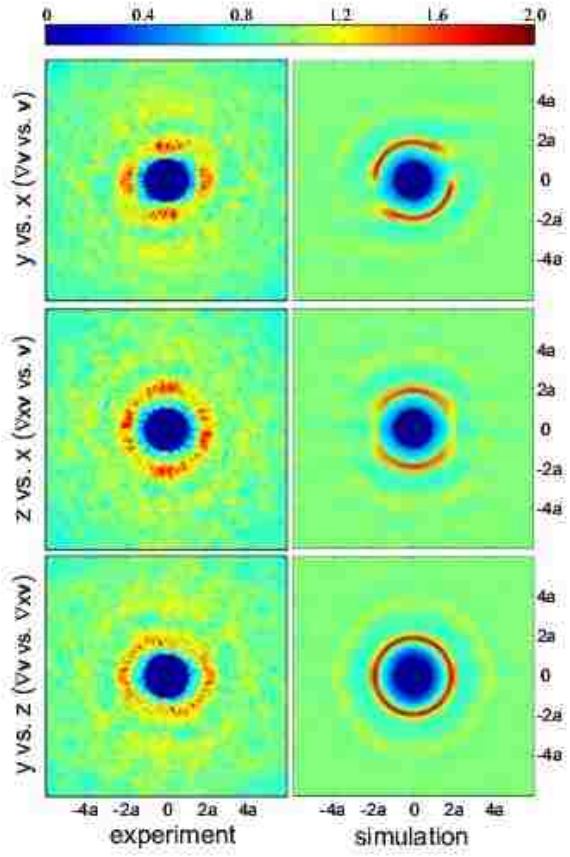
0
0.4
0.8
1.2
1.6
2.0
y VS. X (∇v vs. v)
Z VS. X (∇xv vs. v)
y VS. Z (∇v vs. ∇xv)
4a
2a
0
-2a
-4a
-4a -2a 0 2a 4a
experiment
simulation

(a)

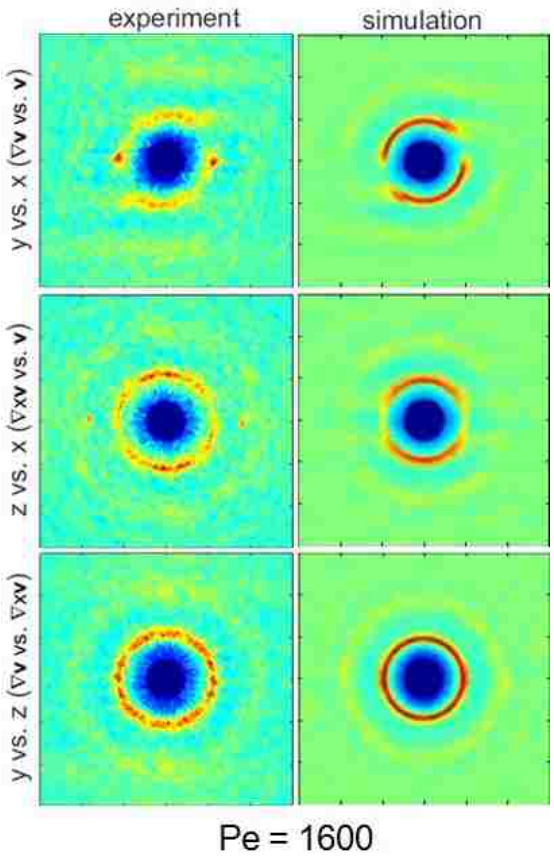

(b)

Figure 1.4: *Comparison between experimental and simulation g(r) plots, (a) original experimental results show signature anisotropy but lack detail in microstructure; (b) modified experimental results compared with simulation studies. Experimental results closely agree with simulation results from Kulkarni & Morris.*

Previous studies from the Gilchrist group have focused on looking at microstructure in simple hydrodynamic flows as well as looking at how electrostatic interactions can affect microstructure. The following section highlights work done by Dr. Bu Xu, a past student from the Gilchrist group, with regard to hydrodynamic interactions in simple shear flows.

1.4.1: Microstructure Study in Simple Hydrodynamic Flows

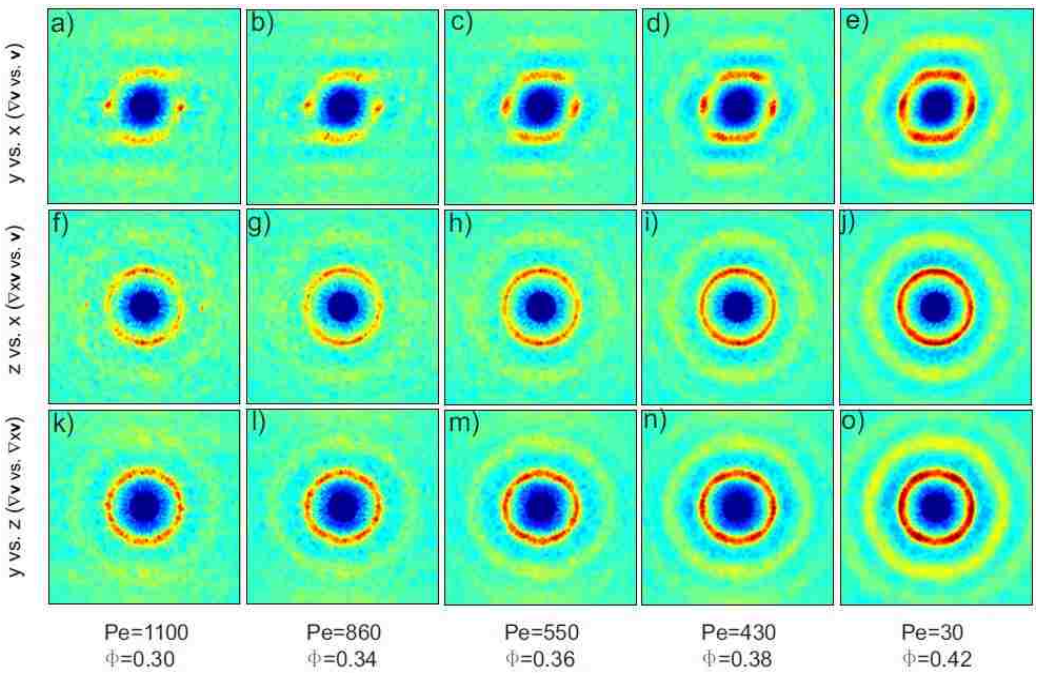

Figure 1.5: *Effect of hydrodynamic force on microstructure. An isotropic ring starts to form with reducing hydrodynamic force. The appearance of a second and third outer ring corresponds to the reducing hydrodynamic forces as well (Xu & Gilchrist 2014)*

The effect on varying *Pe* was studied as shown in Figure 1.5. It is important to note that, in our system the *Pe* and volume fraction are coupled due to shear induced particle migration. As seen in the figure above, you clearly notice that a more isotropic and symmetric structure is formed with reduced hydrodynamic force. This is clearly evident in the y vs. x plane. The anisotropy is being dissipated with reduced *Pe* or in other words, reduced hydrodynamic force. Secondly, the appearance of a second outer ring is visible as the *Pe* number is being lowered. This actually suggests longer range correlation in the system when the shear rate is being reduced.

Extensive experiments are used to determine the shear viscosity of suspensions. Normal stress measurements are challenging. Zarraga et al. (2000) obtained results consistent with computations (Phung et al., 1996) in which the first and second normal stress differences, N1 and N2 are both negative and |N2| > |N1|. Constitutive relations involving normal stress have been applied to model shear-induced migration (Morris & Boulay, 1999; Frank et al., 2003; Miller & Morris, 2006) and viscous resuspension (Ramachandran & Leighton, 2007).

We calculate the first and second normal stress differences based on the method elaborated by Foss & Brady. The leading contribution to rheology here is that we only consider near-contact pair wise interactions (i.e. lubrication forces) between particles. According to the method elaborated by Foss and Brady, the stress tensors can be approximated as;

$$S^H \approx S^H_{b.l.} \approx -n^2 \int_{b.l.} r F^{Shear} g(r) dr$$

$$S^B \approx S^B_{b.l.} \approx -n^2 kTa \int_{r=2a} \vec{r}\vec{r}\, g(r) dS$$

Where S^H and S^B are the Hydrodynamic and Brownian stress contribution to the total stress tensor, b.l. stands for the boundary layer with thickness of $O(Pe^{-1})$ at particle contact, a is the particle radius, n is the number density and $\vec{r}$ is the unit vector in the r direction.

$$F^{Shear} \approx -3\pi\eta'_\infty(\phi) a^2 \dot{\gamma} \vec{r} (\vec{r}.E.\vec{r})$$

where $\eta'_\infty(\phi)$ is the high frequency dynamic viscosity.

Then scaling of data was necessary since ϕ was not constant throughout the channel as a result of shear induced migration. The normal stress differences were scaled by the factor $\eta'_\infty \phi^2 g^0(2;\phi)$ in which $g^0(2;\phi)$is the equilibrium pair distribution function for hard spheres given by the Carnahan-Starling Equation of state for ϕ <0.50,

$$g^0(2;\phi) = \frac{1 - \frac{1}{2}\phi}{(1-\phi)^3}$$

We also obtained the relative viscosity measurements at these same locations. For the same reasons as above, the relative viscosity is scaled and given by;

$$\eta_{r,n} = (\frac{\eta_r}{\eta'_\infty} - 1)/\phi^2 g^0(2;\phi)$$

A comparison of our experimental results with simulation studies are shown in the figures shown below. Figure 1.6 shows a comparison of our relative viscosity data with simulation studies from Foss & Brady (2000). The experimental data clearly show

a shear thinning and shear thickening trend similar to the simulations, but however, it seems that we are off by a factor of 2. The main reason for this could be the limitation to resolution we can obtain from experiments. In addition, electrostatic effects in the real system can also affect in this deviation.

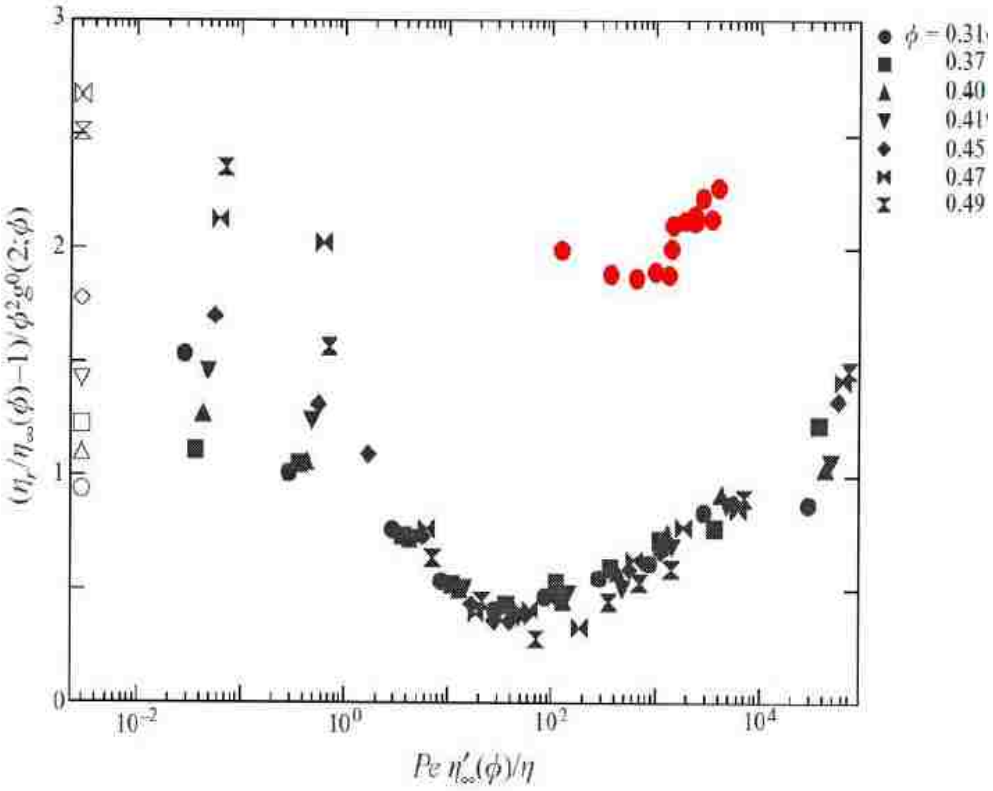

Figure 1.6: *Relative viscosity vs. Pe, rescaled. Red symbols represent experimental data while the black symbols represent simulation data from Foss & Brady (2000). Figure was adapted from Xu & Gilchrist (2014)*

The first and second normal stress differences were also obtained (Figures 1.7 & 1.8). The negative signs of N_1 and N_2 confirms to the compressive nature of sheared suspensions. It is obvious that even after rescaling, Foss and Brady's data still show a fair amount of scatter. Besides the qualitative agreement between experiments and simulations, it appears that experiments demonstrate a smooth ascending trend of normalized $|N_1|$ and descending of normalized $|N_2|$ as the scaled *Pe* increases from 10^3 to 10^4 where there is a crossover of these two quantities. This feature is not clear in Foss and Brady's results. Zarraga et al. reported a maximum of the positive $N_1 - N_2$ as shear rate is increased. However, their experiment did not reach higher shear rates to reveal the possibility of a crossover.

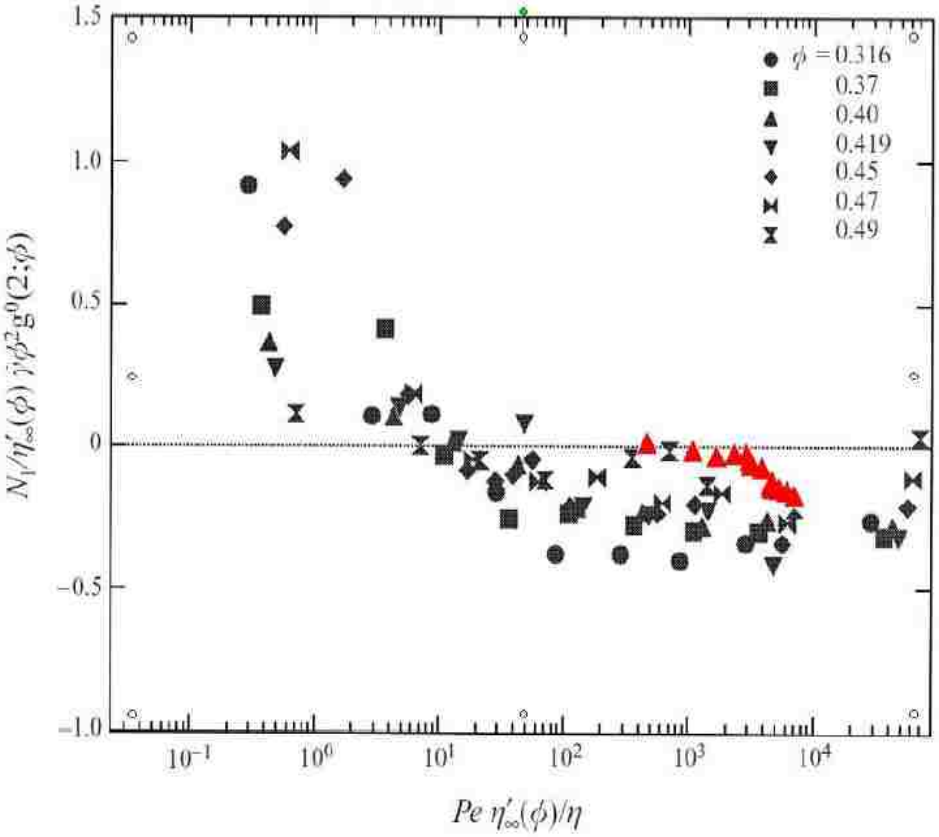

Figure 1.7: *First normal stress difference vs. Pe, rescaled. Red symbols represent experimental data while black symbols represent simulation data from Foss & Brady (2000). Figure was adapted from Xu & Gilchrist (2014)*

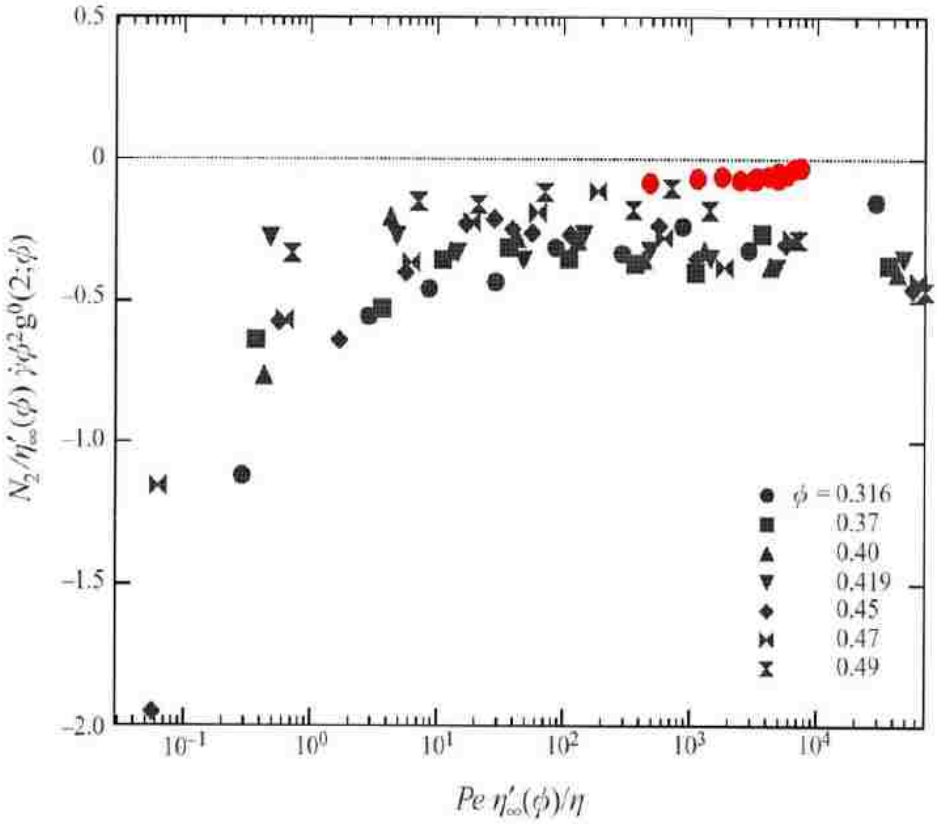

Figure 1.8: *Second normal stress difference vs. Pe, rescaled. Red symbols represent experimental data while black symbols represent simulation data from Foss & Brady (2000). Figure was adapted from Xu & Gilchrist (2014)*

1.4.2: Effect of Electrostatics on Microstructure

Electrostatic interactions can alter suspension structure. Xu & Gilchrist (2014) studied the effects of electrostatics on microstructure. The work is highlighted in this section.

Electrostatic interactions in the suspension can be tuned by the pH as well as the salt concentration in the system. Two parameters related to electrostatic interactions are;

a) Zeta potential, ζ

b) Debye length, $\kappa^{-1} = \left(\frac{\varepsilon \varepsilon_0 kT}{2e^2 z^2 n_b} \right)^{1/2}$

In addition, the zeta potential of the colloidal particles in the system is directly related to the pH. A graph showing how pH varies with zeta potential is shown in Figure 1.9.

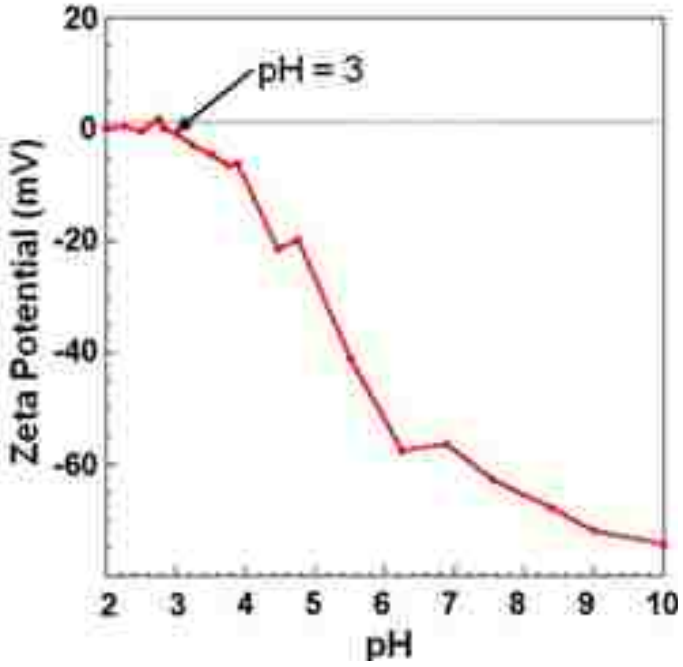

Figure 1.9: *Plot showing how zeta potential varies with pH for a system of colloidal particles*

We studied the effect of Debye length on microstructure as shown in Figure 1.10. As you can see, when the Debye length is increased from 8 nm to 30 nm, the structure is being dissipated and attenuated. This suggests enhanced fluctuation caused by electrostatics between neighboring particles in a suspension. When the Debye length is further increased from 30 nm to 80 nm, a more symmetric and ordered structure is formed, thus implying longer range correlation.

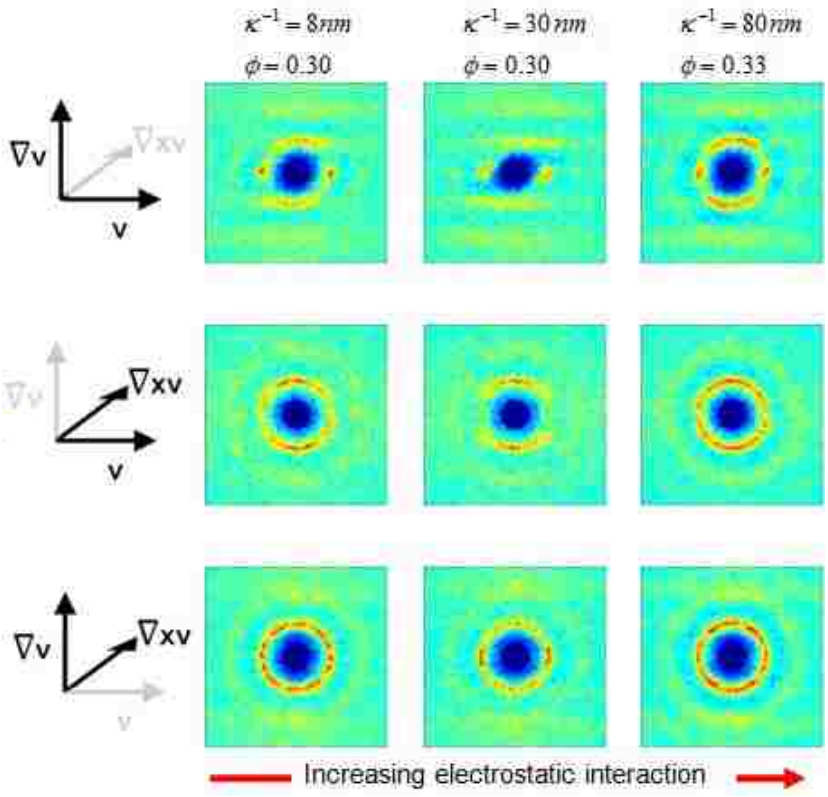

Figure 1.10: *Effect of debye length on microstructure. When the debye length is increased from 8 nm to 30 nm the structure is being dissipated and attenuated. When the debye length is further increased a more symmetric and ordered structure can be observed*

The effect of zeta potential was also investigated. The pH level in the suspension can be controlled with the Sodium Hydroxide (NaOH) concentration. Figure 1.11 shows the effect on microstructure with varying pH at a Debye length of 8 nm. Although not highly noticeable, a similar trend can be observed at a low Debye length in which the structure gets dissipated with increasing electrostatic interactions in the system. Therefore, enhanced fluctuation of particles can be noticed at low Debye lengths.

At a debye length of 80 nm, as expected, we notice longer range correlation with increased electrostatic interactions. When the pH is increased from 6 to 8, a more structured ring is being formed in all three g(r) plots. See Figure 1.12.

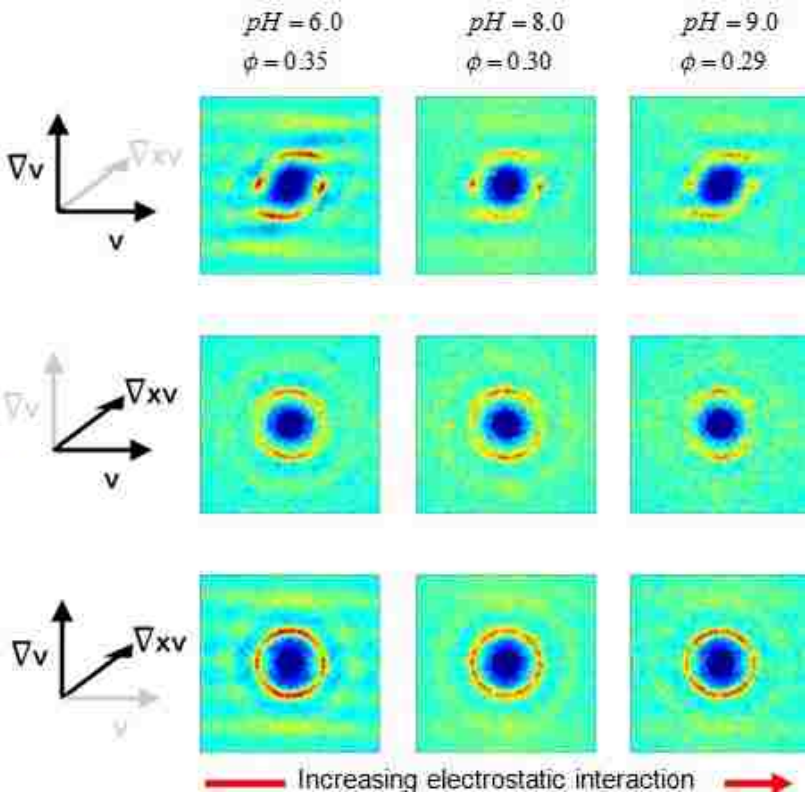

Figure 1.11: *Effect of zeta potential on microstructure at* k^{-1} *= 8 nm. At this debye length you see the structure getting dissipated based on the g(r) plots*

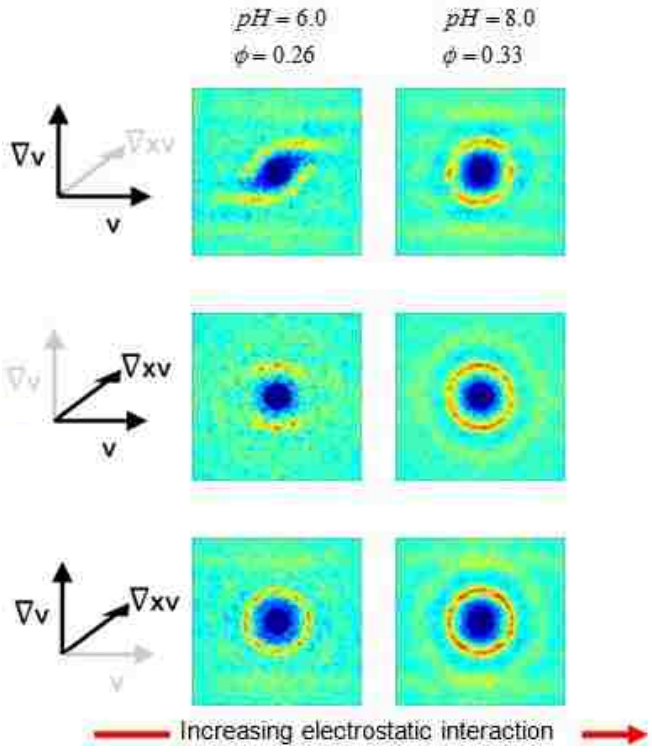

Figure 1.12: *Effect of zeta potential on microstructure at k^{-1} = 80 nm. A more structured ring is formed when the pH is increased from 6 to 8.*

The extension to my work originated when I started to observe particle chaining near the walls in Newtonian and viscoelastic fluids. As highlighted previously, Dr. Bu Xu's work were centralized in studying the effect of hydrodynamics and electrostatics on suspension microstructure. He was able to obtain all these data by scanning across the flow in one single channel thus giving information for a range of *Pe* numbers. But what happens when you keep the velocity profile constant throughout this same channel? If the channel dimensions were changed, the shear rate across the channel kept constant, we were able to observe changes in structure near the boundaries. Particle chaining in the flow direction and order in structure was observed near the boundary. Boundary effects and wall slip have been a well known phenomenon, but boundary effects on suspension microstructure have not been studied. Is there a relationship between wall slip, microstructure and rheology? Can boundary effects be ignored in confined systems of flows? I hope to answer questions like this in Chapter 4 of this thesis.

In addition, based on the introduction of this chapter, it is clear that an anisotropic structure is formed at high *Pe*. With increasing *Pe*, we observe an increase is suspension viscosity as well due to the formation of hydroclusters in the system. An analysis on hydrocluster formation that causes shear thickening is also studied in this thesis using CLSM by using channels that give constant shear rate profiles. Details on this phenomenon will be explained in Chapter 3 of the thesis.

One of the main advantages we have using the CLSM system is the fact that suspension structure can be studied in any complex geometry. We have already proved

that our technique provides us with viable results comparable with simulation. Therefore, chapter 5 of this thesis will be introducing how we can measure structure in real process flows such as flows in porous media. A deeper understanding as to how the structure evolves in such a medium will be studied. Also, it gives an opportunity to see how boundary effects come into play in real processes as well. An analysis on boundary effects in a porous medium will also be studied in Chapter 5 of this thesis.

Chapter 2

Experimental Methods and Techniques

2.1: Fabrication of Microchannels

Microchannels play an important role in microfluidics. Currently, there are many techniques that are available for the fabrication of microchannels. Some of the techniques are room temperature imprinting (Xu et al. 2000), laser ablation (Robert et al. 1997), Injection Molding (McCormick et al. 1998) and soft lithography (Xia & Whiteside 1998). Among these methods, soft lithography is perhaps the most powerful method due to its low cost, reproducibility and biological compatibility.

For this project, microchannels were fabricated via soft lithography using silicon wafers which had patterned microchannel structures that were imprinted at the Cornell Nanoscale facility. Sylgard 184 Elastomer Kit (Dow corning, Co., MI) was used as PDMS (Polydimethylsiloxane). Silicon elastomer base was mixed with curing agent in a 10:1 ratio and poured on to the silicon wafer in order to etch the required channel. Then it was heated at 80°C for 45 minutes. In addition, connectors (Harvard Apparatus) were placed prior to molding the PDMS in order to provide for inlet and outlet for the

channel. Finally, a clean glass cover slip (cleaned with Piranha solution) was attached using an oxygen plasma cleaner, and heated on a hot plate at 65°C for 5 minutes for stronger bonding. The bond formed between the PDMS and the coverslip was strong enough to withstand relatively high pressures required to produce flow in the channel. Through imaging, the degree of swelling of the channel due to the induced pressure is monitored and considered when determining the location to take images of the flow in order to minimize the occurrence of reverse or 3D flow.

For Chapter 5 of this thesis, we used channel structures that used a model porous network. The silicon wafer that contained this patterned structure was obtained from Professor Xuanghong Cheng's Laboratory at Lehigh University. The channel structure was imprinted at their laboratory facility.

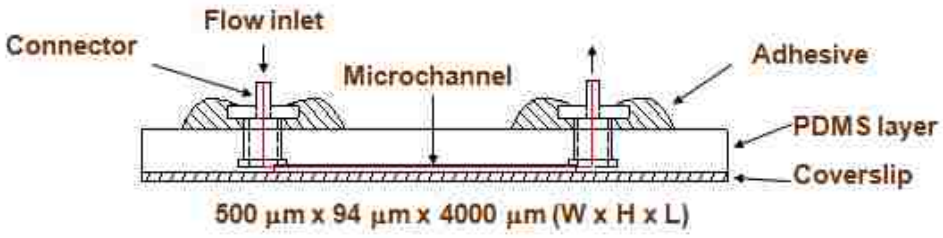

(a)

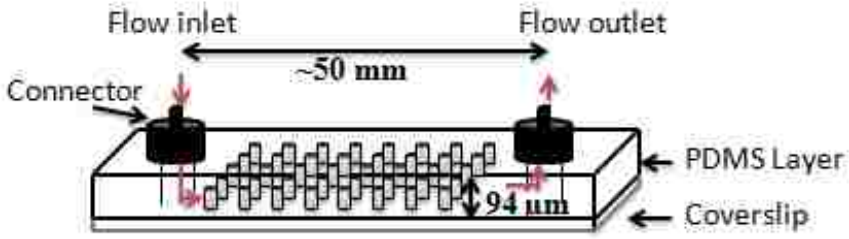

(b)

Figure 2.1: *(a) Side view of the typical microchannel. The PDMS microchannel is attached with a glass coverslip at the bottom and has a flow inlet and outlet. This is a straight channel with dimensions of 500 µm X 94 µm X 4000 µm (W x H x L) utilized to achieve constant shear rate profiles when flowing. This channel was used for the studies of chapter 3 and 4 of this thesis.*

(b) Channel that contains a porous network structure. The silicon wafer that contained this patterned structure was obtained from Professor Xuanghong Cheng's Laboratory at Lehigh University. This channel was used for the study described in Chapter 5 of this thesis.

2.2: Cleaning of Glass Slides with Piranha Solution

Glass slides used to bond to the PDMS were cleaned using Piranha solution. Initially, 40 ml of 98% Sulfuric acid was added to a graduated cylinder. Then, 10 ml of Hydrogen peroxide was added to the sulfuric acid containing cylinder. Thin glass slides were taken and placed in a glass container. The sulfuric acid/hydrogen peroxide solution was added to the glass container and was left inside the fume hood overnight. On the following day, six weighing boats with DI water were used to rinse the glass slides using a pair of tweezers. Finally, the piranha solution was disposed in acid waste. The water/acid in plastic was also disposed in the waste container in the hood. Note that personal protective equipment such as the lab coat, safety goggles, forearm guards and gloves were worn at all time during this process and was carried out in the fume hood.

2.3: Particle Synthesis

Monodisperse colloidal particles with uniform size and shape have wide applications in many fields. Currently, the most effective way to synthesize monodisperse silica particles is known to be the Stober method. The Stober method was utilized for particle synthesis in this project.

980 nm fluorescent silica particles were synthesized using Tetraethylorthosilicate (TEOS), 200 proof ethanol, Deionized (DI) water, and Ammonium Hydroxide. On day one, 30.8 mg of 3-aminopropyltriethyoxysilane(APS) was mixed with 5 ml of 200-proof ethanol in a small flask. Then, 19.6 mg of Rhodamine Isothiocyanate (RITC) was added to prepare the dye solution. This dye

solution was the source to the fluorescence for the particle cores to be prepared. The prepared solution was stirred overnight.

On day two, 17.28 ml of 200-proof ethanol, 24.88 ml DI Water, and 7.81 ml of ammonium hydroxide were mixed initially in a flask. TEOS (4.52 ml) and ethanol (45.48 ml), also premixed, were added to this solution to start the particle synthesis reaction along with the dye solution from day 1. The particles synthesized from this process were about 500 nm.

Larger particles were made using the core-shell approach. One addition of TEOS (4.52 ml) and ethanol (45.48 ml) were added after 6 hours in order to build shells around the synthesized seeds. The particles synthesized after this addition had an average diameter of about 980 nm. Note that a moderate stirring rate was kept at all times during the synthesis process.

Finally, the synthesized particles were washed and centrifuged a minimum of 6 times with ethanol and 3 times with DI water. Scanning Electron Microscope (SEM) images of the 980 nm fluorescent particles are shown in Figure 2.2.

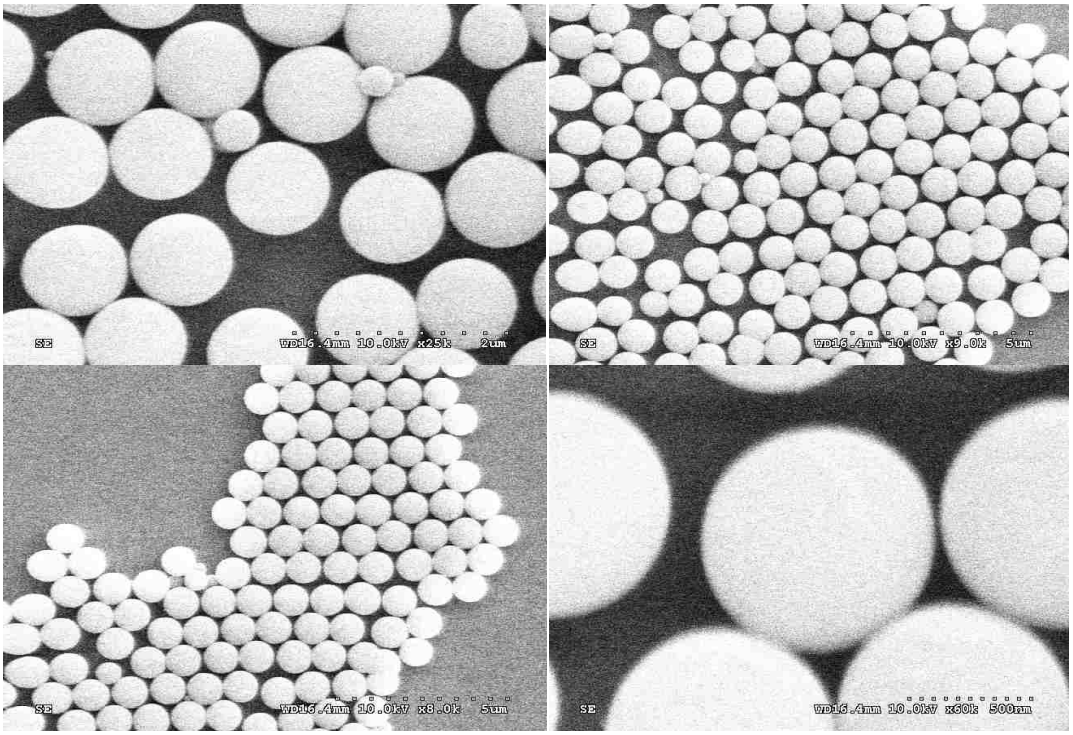

Figure 2.2: *Scanning Electron Microscopy (SEM) Images of 1 micron Fluorescent Silica particles. The particles are monodisperse and impurities have been washed away (images taken before washing)*

2.4: Suspension Preparation

Particles were dried using a dessicator. In a separate bottle, a 3:1 glycerine:water solution was prepared and NaOH and NaCl were added accordingly in order to obtain a pH of 8 and a salt concentration of 0.001M that corresponds to a debye length of about 6 nm. This solution was added to the dried particles so that the overall silica volume fraction was about 0.4. We have also used suspending fluids containing 0.035 wt% Polyacrylamide (PAM) solids in glycerine water, 0.04 wt% Lamda DNA in Dimethylsulfoxide (DMSO) and pure DMSO as suspending media in various projects in this thesis.

The prepared suspension with an overall silica volume fraction of about 0.4 is injected into the connector at channel inlet. The channel is then put onto the platform of the confocal microscope. Compressed nitrogen is then connected to the inlet to drive suspension flow, the pressure of which is controlled by the electropneumatic converter (Experiments described in Chapter 4 and 5). In some experiments we have also used a syringe pump to drive the flow. Using the syringe pump provided us with convenience in controlling the flow to obtain various shear rate profiles (with subtle differences) for the hydrocluster study (Chapter 3). However, it was more challenging to cease the flow and obtain steady velocity profiles from the syringe pump as opposed to the pressure controlled by the electropneumatic converter. See Figure 2.3.

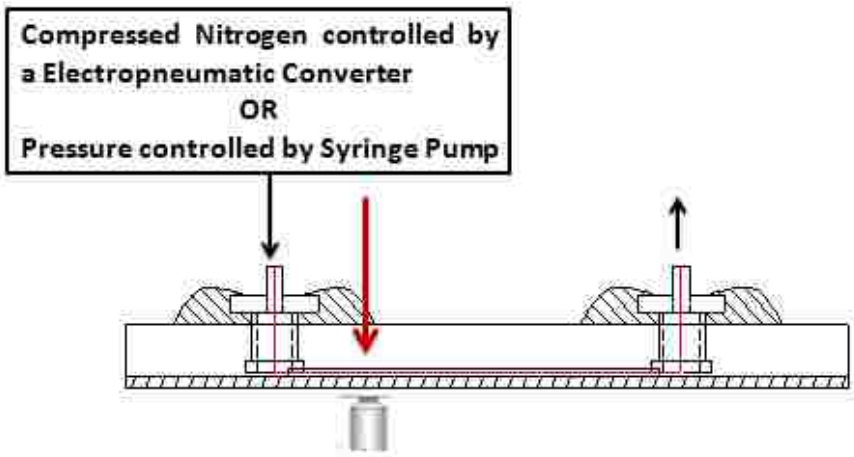

Figure 2.3: *Set up of the confocal microscope platform. Compressed nitrogen was used via the electropneumatic converter to drive the suspension using pressure-driven flow (for experiments described in Chapters 4 and 5). A syringe pump set up was used to perform experiments described in Chapter 3 of this thesis.*

2.5: Imaging Protocol

Suspension was flowed for a few minutes (maximum velocity at the center of the channel ~ 700 μm/s: Pressure ~15 psi) a time scale much longer than the average residence time of particles in the channel. During this period, velocimetry was conducted in which the microscope scanned from the bottom toward top of the sample along the vertical or velocity-gradient direction, taking 10 images every 0.1 μm at 100 fps. See Figures 2.4 and 2.5.

Then the stop-flow scans can be started. Suspension flow was driven for a few minutes (using the same technique as before), and then the nitrogen to the channel was suddenly arrested. The flow was quickly arrested by reducing nitrogen pressure to the channel. Immediately after flow cessation, confocal scanning through the system was started, in same way as in the velocimetry measurement except that now we took 1 image per 0.1 μm. After the scan, flow was restarted and the stopped-flow operation was repeated for at least eight times in each experiment, as shown in figure 2.4.

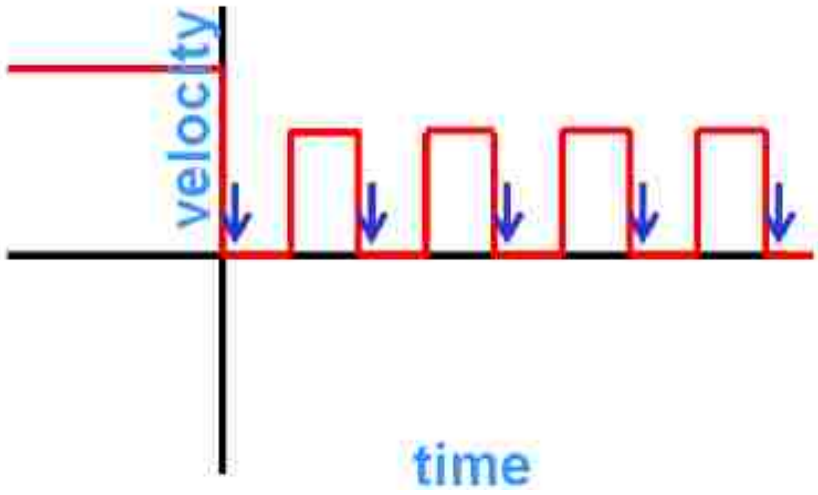

Figure 2.4: *Stop flow scan procedure displayed with time. The suspension was flowed for a few minutes till it reached a certain velocity and then the flow was arrested and the scan was performed. The blue arrows show the points at which the scans were taken*

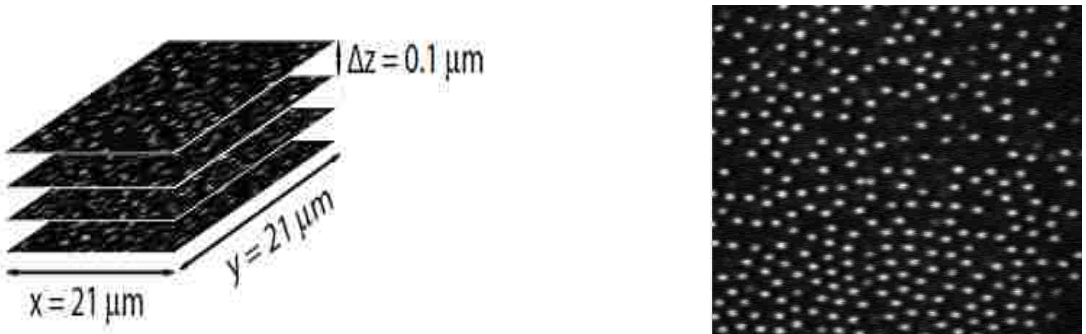

(a) (b)

Figure 2.5: *(a) Example of a Z-stack image capture series. The dimensions of the images taken are shown. Images were taken every 0.1 µm at 100 fps for the velocimetry and stop flow scan procedures. (b) This image shows a typical fluorescent image of particles as seen on the confocal microscope.*

2.6: Particle Image Velocimetry

The z-direction velocimetry scans are processed in IDL. The velocity at each point could be calculated by comparing displacements of the same particle between frames differed by a certain time interval and averaging over at least ten particles. This procedure is performed from the bottom to the center of the channel. A velocity profile can be obtained as shown in the Figure 2.6. Once the velocity profile is obtained, the shear rate can be calculated based on the slope of the line of data. Then, the *Pe* can be obtained using the equations described in the introduction of this thesis. It is important to note that the shear rate may vary along the velocity gradient direction of the channel. However, as seen in Figure 2.6, we could approximate the shear rate to be constant in the region of interest for our studies in this thesis. The errors in the velocimetry represent the standard deviation of the velocities when averaging the velocity over ten particles at each layer of particles away from the bottom of the wall.

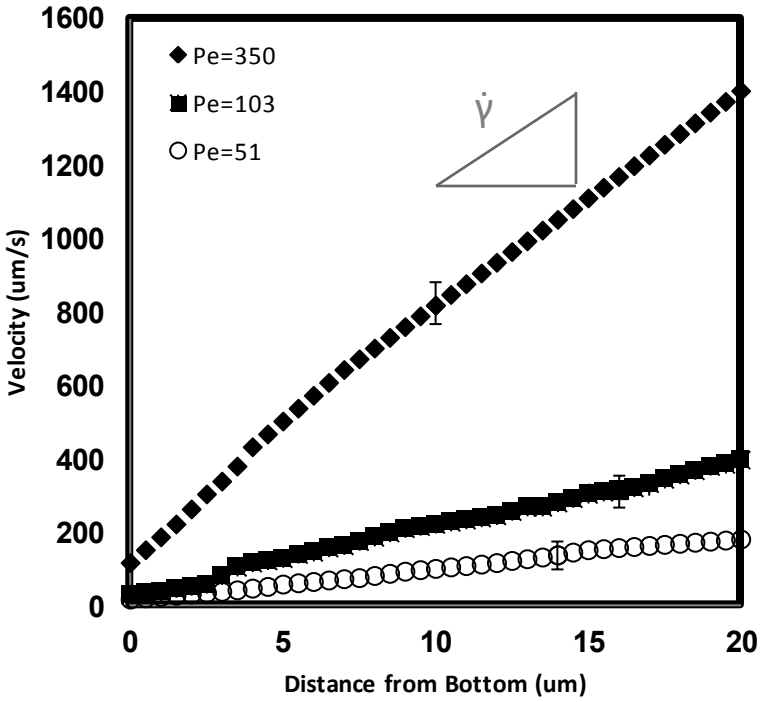

Figure 2.6: *Velocity profile obtained of the suspension by comparing displacement of particles in IDL. Shear rate can be obtained by calculating the gradient of velocity over the distance from the bottom layer.*

2.7: Particle Tracking

Particle-tracking routines developed by Dr. Eric Weeks at Emory University were used to reconstruct the three-dimensional particle distribution in the experiments. The IDL software is designed to look for bright particles on a black background. It looks something similar to figure 17 (b) above. When tracking in 3D, the particles of interest are between about 10 and 20 pixels in all three dimensions. The software then uses a process called *band pass filter* in order to track the predominant features (particles) accounting for various distortions in the images. Once the particles were tracked, it uses a feature called *profiles* to obtain the particle coordinates (x,y and z coordinates). The error in center determination is roughly 20-40 nm in x and y, and 40-80 nm in z (the velocity gradient direction). Finally, they are saved as text files so that they can be plotted using a numerical software such as MatLab. A sample three dimensional reconstruction of particles is shown in Figure 2.7.

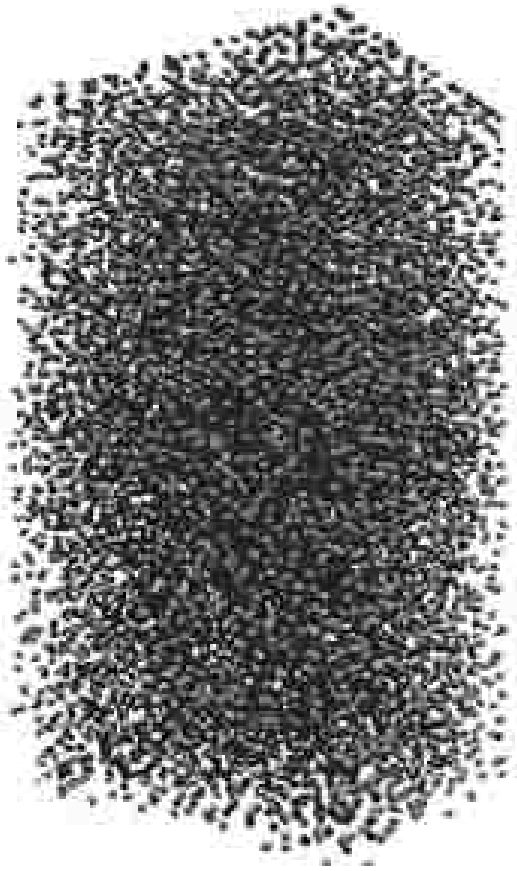

Figure 2.7: *A 3D reconstruction of particles obtained using the particle tracking coordinates from IDL. The image above shows a true 3D rendering of particle structure similar to if it was flown in the actual microchannel*

2.8: Data Analysis

Now g(r) plots can be obtained. Once a specific plane is selected, neighboring particles are identified 3 particle diameters around a reference particle, for all particles. These particle coordinates will be used for the g(r) calculations. The spatial coordinates are normalized by particle diameter. Also, the total number of particles on the plane is identified. This procedure is repeated for all the planes that cover the z-stack image captures we obtained, averaging for all the eight experimental scans. Finally, for each specific *Pe*, we obtain the local g(r), which is plotted on three orthogonal planes formed by three axes along directions of flow (x), velocity gradient (y) and vorticity (z) (note: these are conformed to the JoR standards, and not relative to the laboratory frame). We plot the three projections using Matlab. The bin volume used to indentify particles for g(r) is $\Delta r=0.2a$ and $\Delta\theta=3.6°$. All plots of g(r) span dark blue to red colors representing the range $0 \leq g(r) \leq 2$.

For chapter 3 of this thesis, we also investigate hydroclusters. Based on the particle coordinate data we obtain, we are able to track down clusters of particles using IDL. When the center-center distance between two particles is less than one particle diameter, we define these two particles to be a part of a cluster. Similarly we perform this analysis in IDL further, to identify number of clusters and cluster geometries that will be further discussed later in this thesis.

2.9 Rheometry

The AR2000 Rheometer by TA Instruments was used to analyze the rheology of some suspensions. This is a stress controlled rheometer. Typically, a 20 mm cone with a 2° angle was used. The viscosities of interested suspensions were obtained by shearing the sample from 0.1 to 100 s^{-1}. Oscillatory measurements were also performed to obtain viscosities and the data for storage and loss moduli. The standard operating procedure was used as highlighted in the instruction manual for this instrument and all suspensions were pre-sheared for 1 minute before obtaining rheological data for that suspension.

For viscoelastic fluids, the relaxation time was calculated by obtaining the crossover frequency between G' and G''. Then, the relaxation time, λ;

$$\lambda = \frac{1}{\omega}$$

Where ω is the crossover frequency.

Chapter 3

Hydrocluster Analysis of Suspensions

3.1: Introduction and Previous Work

Shear thickening which is characterized as the increase in shear viscosity with increasing shear rate or shear stress has become one of the most significant changes occurring in a stable colloidal dispersion (Barnes 1989). This phenomenon can be beneficial in applications involving electro rheological fluids (Shenoy et al. 2003), materials that can stiffen and dampen simultaneously (Fischer et al. 2007), flexible composites (Decker et al. 2007) as well as enhanced body armor (Lee et al. 2003). As mentioned in the introduction of this thesis, shear thickening in stable colloidal dispersions is understood to be driven by the dominance of short-range lubrication hydrodynamic interactions that lead to particle clustering (Brady and Bossis 1985). Two causes of shear thickening have been proposed by previous studies. The order-disorder transition (Hoffman et al. 1972;1991, Laun et al. 1992) and the 'hydrocluster' mechanism (Bender & Wagner 1995;1996, Melrose et al. 1996, Brady & Bossis 1998, Phung & Brady 1996). The argument for the order-disorder transition was that at low

shear rates particles organize into layers or strings that would result in a lower viscosity than would be obtained for a flowing disordered suspension. At high shear rates lubrication forces between neighboring particles induce particles to rotate out of alignment and destabilize the flow (Maranzano & Wagner 2002). This results in an increase of viscosity due to an increase in the interparticle interactions in the flowing, disordered state. Based on simulation predictions by Bossis & Brady (1985), and later on by computational evidence by Boersma and coworkers, and Melrose and coworkers, the more widely accepted mechanism for shear thickening is the hydrocluster mechanism.

These particle clusters, known as "Hydroclusters" were initially predicted by Stokesian Dynamics simulations, were then observed experimentally by rheo-optical and neutron scattering methods (Bender & Wagner 1995, Dhaene et al. 1993, Maranzano & Wagner 2001;2002, Newstein et al. 1993). Essentially the brief mechanism behind the hydrocluster formation is the shear induced self organization of colloidal microstructure that forms clusters of particles under the influence of short ranged lubrication forces. Understanding the formation and structure of these hydroclusters is key to understanding suspensions rheology.

In this chapter of this thesis, we try to approach to understand shear thickening and the formation of hydroclusters through measuring microstructure via CLSM. When a suspension is sheared, shear thinning is observed until a characteristic shear rate $\dot{\gamma}_c$ after which the viscosity increases. In terms of a microstructural perspective, shear thinning can be thought as the phenomenon in which the rate of shear exceeds to that of

which the microstructure is able to relax under the conditions. With further increase in the shear rate, these particles undergo microstructural changes resulting from the inability to overlap as they are forced along the compression axis of the shear field. The boundary layer produced from the balance of shear forces bringing the particles together and Brownian or interparticle forces that ensure particles do not overlap, gives rise to the localization of particles into what are now referred to as hydroclusters (Bossis and Brady 1989).

Maranzano & Wagner (2001;2002), Krishnamurthy et al. (2005), Egres & Wagner (2005), Wagner & Brady (2009), Bender & Wagner (1996), Gopalakrishanan & Zukoski (2004) have shown that the onset of shear thickening can be dependent on many factors such as particle size, volume fraction, effect of attraction between particles as well as polymer interactions in the suspending medium. In general, suspensions of larger particles have been found to thicken at lower shear rates, and polydispersity increases the critical shear rate (Bender and Wagner 1996). Therefore, note that for the purposes of this study, we have used the standardized suspension described in Chapter 2 of this thesis.

3.2: Results & Discussion

3.2.1: Suspension Microstructure

In order to understand this phenomenon further, we carried out experiments flowing 1 μm Silica particles in a glycerine/water solution under varying *Pe*. The average volume fraction of particles in the suspension is 30%. The suspension was flowed in much wider and higher channel dimensions (as opposed to Dr. Bu Xu's work from the Gilchrist lab) in order to obtain an approximately linear velocity profile. See figure 3.1 below. This would suggest that the shear rate profile would be approximately constant in the area of interest of the region of the channel. The region of interest in this case is from 0 to 20 μm away from the channel wall or channel bottom. A linear fit was used to approximate the shear rate in each of the respective flows and correspondingly we obtain *Pe* of 14, 51, 103, 166, 230, 310 and 350 for the different flow experiments. The channel dimensions for this case was 4000 μm **X** 500 μm **X** 94 μm (L **X** W **X** H).

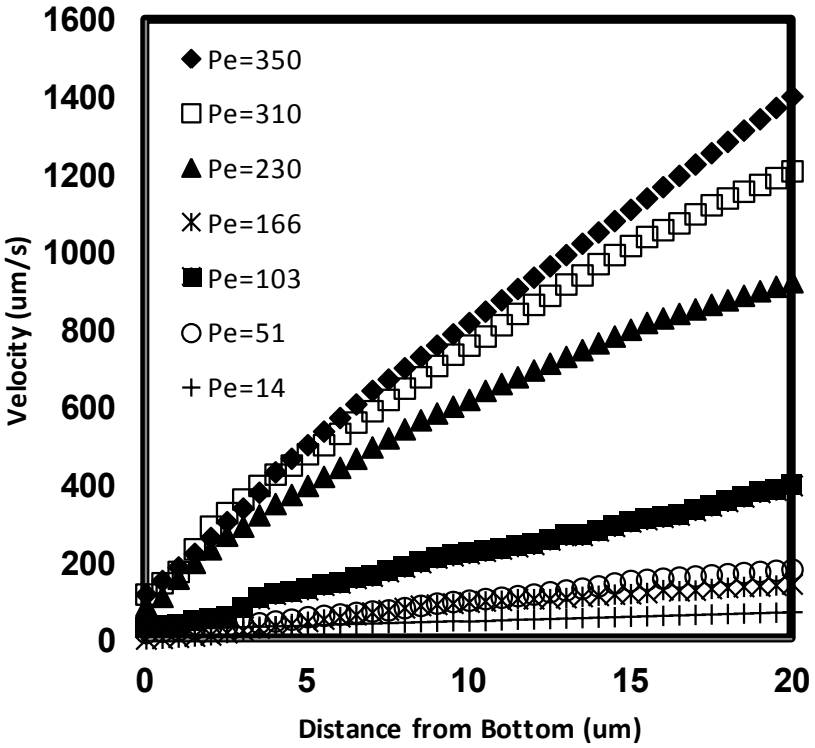

Figure 3.1: *Velocity profiles of particles flowing in the suspension from 0 to 20 μm away from the channel bottom (wall). The velocity profiles shown correspond to different shear rates and thus have been plotted for different Pe. Symbols span data for Pe of 14, 51, 103, 166, 230, 310 and 350 as shown.*

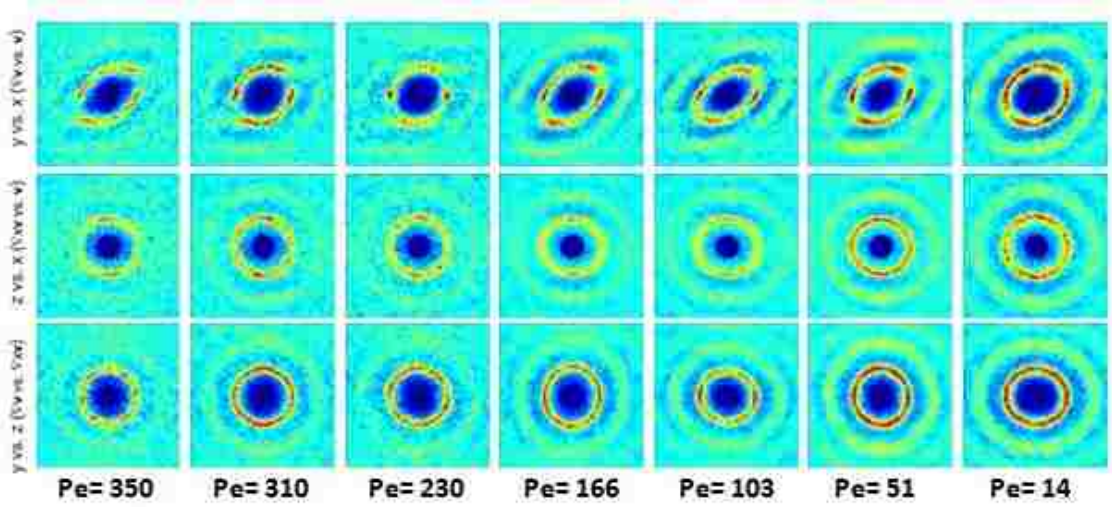

Figure 3.2: *g(r) plots for the y vs. x, z vs. x and y vs. z planes for Pe= 350, 310, 230, 166, 103, 51 and 14. The pair distribution functions shown are averaged between 6 µm to 12 µm from the channel bottom.*

The pair distribution functions for all the planes averaging particles from 6 μm to 12 μm were obtained as shown in figure 3.2. Note that we have eliminated particle details from 0-5 μm for this averaging due to the wall slips that we have observed in our experiments. We observe a degree of order in the microstructure closer to the walls (i.e till about 5 μm away from the channel wall) and therefore averaging in those regions are neglected in order to obtain more accurate results for this hydrocluster study. A more detailed study with regard to wall slip and its effects on suspension microstructure will be discussed in the next chapter.

When we observe the microstructure, a clear anisotropic ring is evident for the y vs. x plane for all *Pe*. Previous studies show that the nearest neighbor ring is supposed to get narrower as the Pe increases (Morris & Brady 1997, Foss and Brady 2000). Our experiments however are not able to capture this phenomenon in detail between experiments. The anisotropy is less and the nearest neighbor ring is certainly more broadened for the Pe=14 case. A narrowing of the nearest neighbor ring as well as more anisotropy can be seen when comparing two farthest *Pe* cases (such as *Pe* =350 and *Pe* =51) but not necessarily when the *Pe* cases are closer together. The z vs. x and y vs. z planes show isotropic rings at all *Pe*. The individual g(r) plots at distances of 6, 8, 10 and 12 μm away from the wall at each *Pe* were very similar to each other, thus assuring of a constant Pe throughout the region been considered. Also, it is important to note that you see the intensity of the first nearest neighbor ring getting intensified along the compressive axes as predicted by previous Stokesian simulation methods. This suggests that the particles are forced closer together along the compressive axes by

hydrodynamic shear forces upstream. A weak repulsive force between particles also act downstream but is negligible to the hydrodynamic force. In the downstream side, both the repulsive force and the hydrodynamic shear forces act together in separating particles from contact.

3.2.2: Investigation of Particle Clustering and Effects on viscosity

A hydrocluster is defined as any two particles of which the center-center distance is less than or equal to about one particle diameter (Figure 3.3). Clustering can be readily quantified from our particle tracking data. By looking at the nearest neighbor distance of two particles, we identify particles constituting to a cluster. If the center-center is distance is less than or equal to about one particle diameter we consider those two particles to be part of a cluster, and repeatedly we perform this for all particles in IDL based on our particle coordinates. Our experimental data identify clusters ranging from 2 particles to as high as 15 particles.

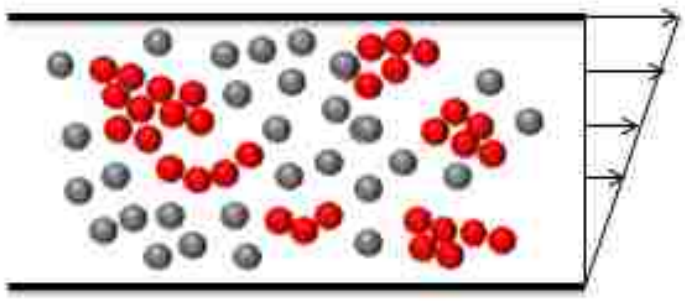

Figure 3.3: *A flowing particle suspension with a few Hydroclusters identified (in red)*

For the purposes of this study, we obtain cluster data constituting to 5 or more particles. We define N to be the number of clusters constituting to particles of 5 or more. Based on our results, we see that the clusters grow with increasing Pe as shown in Figure 3.4. The formation of Clusters of particles greater than equal to 5 clusters with increasing Pe is also an assurance to the shear thickening regime as discussed before. The growth of clusters with Pe fits an exponential profile with $N = 8.7577e^{0.0056Pe}$. The error bars shown give the standard deviation of the number of clusters for each Pe for the different 5 scans we perform during our experiments. The formation of clusters leads to shear thickening and when we obtain the relative viscosity calculations for this study, we clearly see an increase in shear viscosity after a critical shear rate, $\dot{\gamma}_c = 9$ (or $Pe = 51$). This will be the onset of shear thickening behavior for the system.

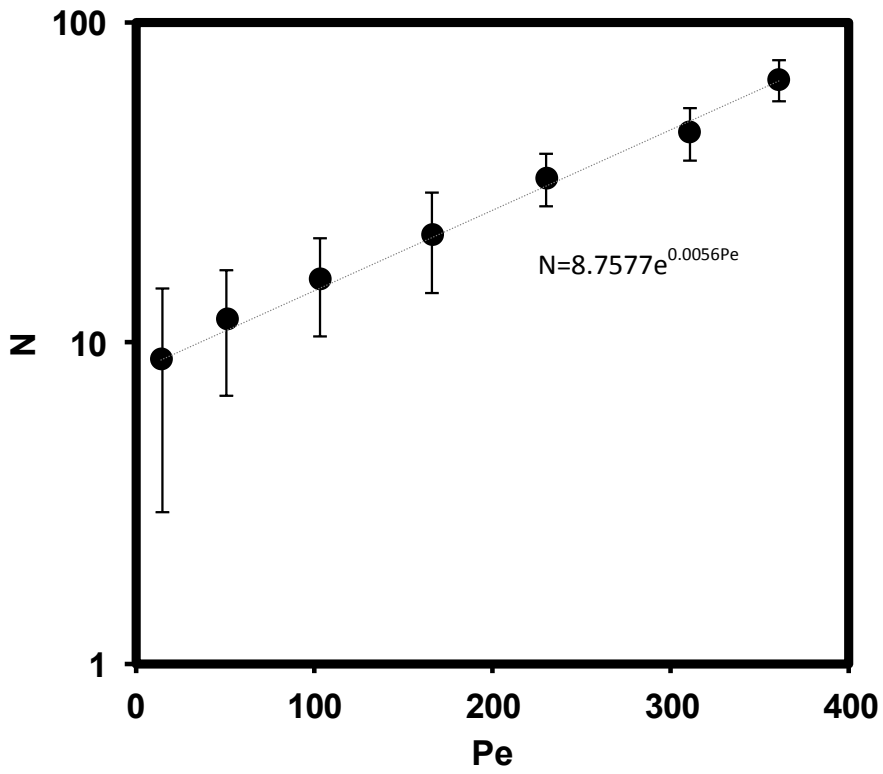

Figure 3.4: *Number of clusters constituting to 5 or more particles in a cluster (N) plotted against Pe. The results suggest an exponential increase of clusters that fits an exponential profile of N= 8.7577 exp (0.0056Pe)*

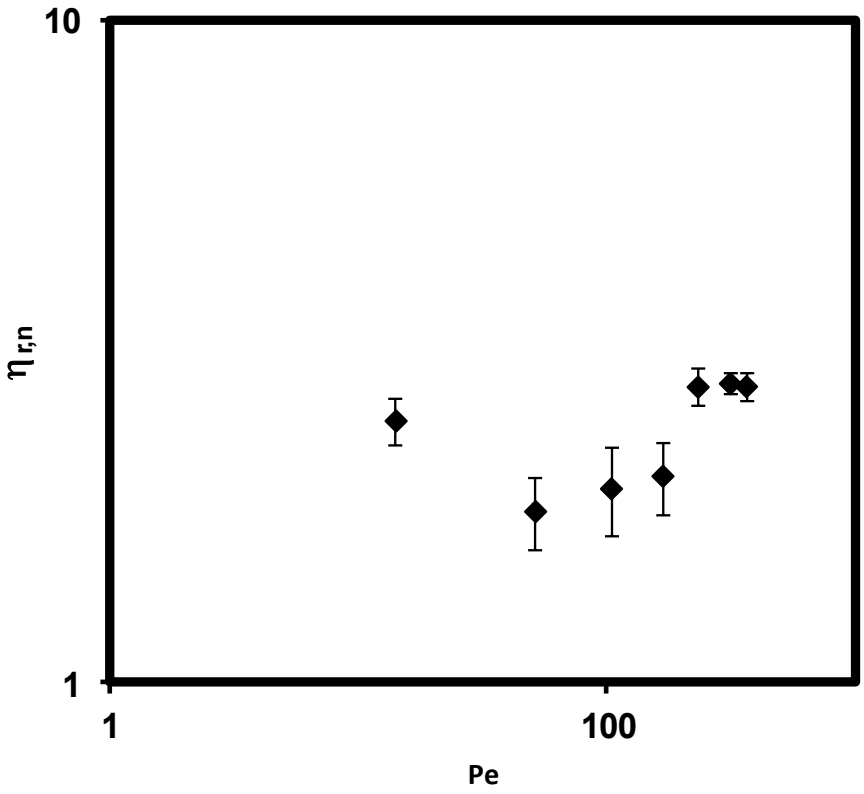

Figure 3.5: *Relative viscosity (η_r) plotted against Pe. The graph shows a shear thinning and thickening trend in which you see the shear thickening to start at a Pe~50.*

Based on Figure 3.5, we see that the relative viscosity starts to increase after the critical shear rate of $\dot{\gamma}_c = 9$ ($Pe = 51$). What is unclear here is the fact that we notice a drop in relative viscosity from $Pe = 14$ to $Pe = 51$ even though the number of clusters has increased. The relative viscosity is affected by all the particles in the system and not just the clusters. This suggests that even though the number of $N \geq 5$ clusters increased from $Pe = 14$ to $Pe = 51$, the smaller particle clusters and other individual particles in the system causes a lower stress distribution to viscosity when flowing that results in a reduction of viscosity. After $Pe \sim 50$, the stress distributions from the clusters dominate and results in an increase in viscosity in our system. Therefore, we can deduce that once the critical shear rate has been achieved, the exponential growth of the clusters is the cause for the shear thickening behavior of a colloidal suspension.

We have also computed the Brownian contribution to the viscosity as shown in Figure 3.6. The Brownian contribution to the relative viscosity does not seem to be very dominant and reduces with increasing *Pe*. As expected, we see that with the rise of hydrodynamic force (increasing *Pe*) the hydrodynamic component of the viscosity starts to dominate. The increase in shear forces is what causes the increase in the hydrodynamic contribution. Foss and Brady 2000 mentions that at high *Pe* ($Pe \geq 10$), the shearing forces overcome Brownian motion and push particles into close contact where the short range hydrodynamic lubrication forces are important. Our Brownian viscosity results also qualitatively match with Foss and Brady 2000, where the Brownian contribution to the viscosity is shown to decrease in an exponential manner. We would also like to make note that our results demonstrate that shear thickening is

not a consequence of the order-disorder transition. This is because we do not observe any order in our g(r) plots presented in Figure 3.2. Also, a reconfirmation to the fact that shear thickening does not occur as a consequence of the order-disorder transition was found by investigating the Bond Order Parameter, Ψ_6, on the x-z plane for the different *Pe* in our experiments. The equation defining Ψ_6 is shown below.

$$\psi_6 = \frac{1}{N}\sum_{j=1}^{N} exp\left[6i\theta(r_{ij})\right]$$

Where *N* is the number of nearest neighbors with respect to particle *i*, θ is the angle between particle *i* and *j* with respect to a horizontal line and r_{ij} is the distance between particles *i* and *j*. A $\Psi_6 = 1$ is defined to having an order of a perfect crystal. As you can see in Table 3.1, our results show not high order in our system and the bond order remains constant regardless of the *Pe* in our experiments. This is a good indication that our system does not undergo any order-disorder transition during the shear thinning and thickening behavior.

Pe	Ψ6
14	0.163
51	0.173
103	0.168
166	0.165
230	0.162
310	0.164
350	0.16

Table 3.1: The bond order parameter, Ψ_6 obtained for the different *Pe* experiments. The value remains constant regardless of the *Pe* in our experiments

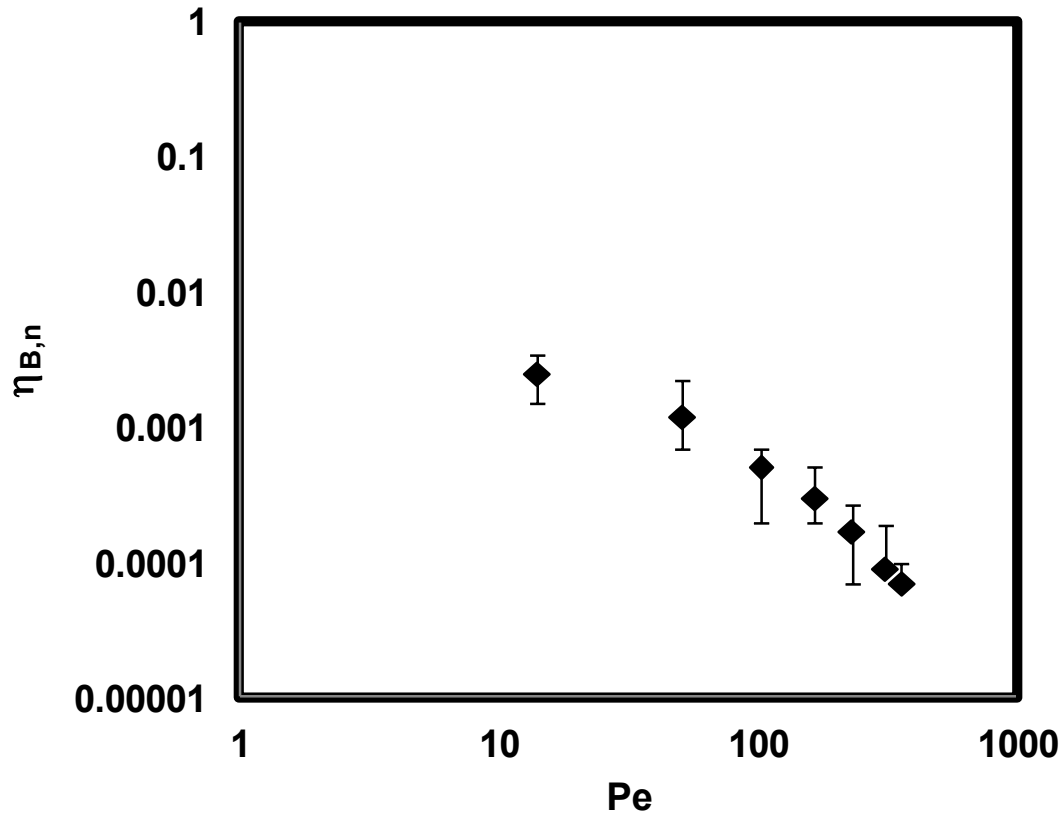

Figure 3.6: *Brownian contribution to the relative viscosity (η_B) plotted against Pe.*

3.2.3: Probability Distribution of Clusters size

Next, we look closer at the probability distribution of the cluster size distributions for each of the *Pe* being considered in our study. See figure 3.7. From our results, we see that the 5 particle clusters dominate the most at all *Pe*. The formation of 5 to 12 particle clusters can be seen till the *Pe* ~ 200 region, but when the *Pe* is greater than 300 we see the emergence of 13 to 15 particle clusters as well. At *Pe*=14 and 51, the probability distribution of the 5-12 particle clusters remain approximately the same based on the bar chart. But till *Pe* reaches 300, the 5-8 particle clusters show more distribution compared to the 9-12 particle clusters in this region. And then eventually at *Pe* >300, the 5-8 particle clusters peak compared to the rest of the particle clusters. Our experiments indicate that when $1 < Pe < 50$, particle clusters of 5-12 emerge with equal distribution. Once this is reached (this is where we noticed the onset shear thickening critical shear rate or *Pe*), shear thickening starts to appear as there are more emergences of the 5-8 particle clusters. With increasing hydrodynamic forces, more and more 5-8 particle clusters start forming and you notice particle clusters of 12 or more appearing as well.

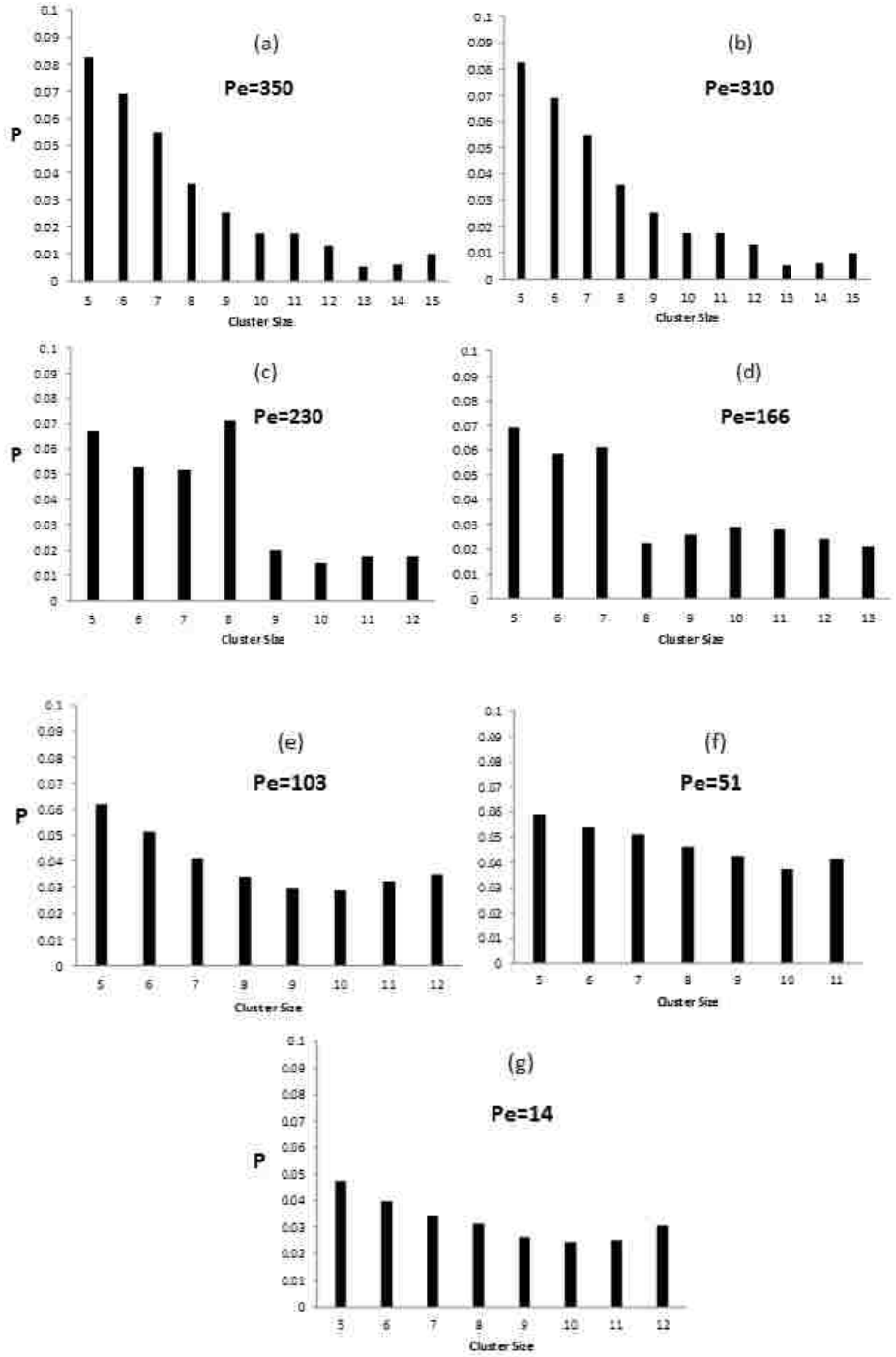

Figure 3.7: *Probability of Cluster size distributions for Pe (a) 350, (b) 310, (c) 230, (d) 166, (e)103, (f) 51, (g) 14*

Essentially, our results indicate that the dominance of 5-8 particles is what causes the onset of shear thickening. At Pe = 14 and 51 the cluster size distribution is constant and thus do not attribute to the onset of shear thickening behavior. As the Pe increases we clearly see the peaks of the 5-8 particle clusters as compared to the other cluster sizes. And when Pe is greater than 300, the 5-8 particle clusters still dominate with the emergence of a few 12 plus particle clusters. However, the argument given by Cheng et al. 2011 is somewhat different from our analysis. According to Cheng and coworkers, the cluster size distribution reduces linearly with increasing particle number until the onset of shear thickening, and they observe an exponential decay of cluster size distribution after the onset of shear thickening. Our results match with Cohen's results at $Pe \geq 300$ where we see an exponential decrease in cluster size distribution. But as mentioned previously, when Pe is less than 50, we see almost an equal distribution of cluster size. At Pe = 166 and 230, we do not observe an exponential decay of cluster size distribution. Therefore, based on our results, we can conclude that the dominance of the 5-8 particle clusters compared to other particle clusters is the cause of shear thickening behavior. In addition, the appearance the N greater than 12 particle clusters at higher Pe is also consistent with Cheng and coworkers' results.

3.2.4: Angular Dependence of particles constituting a cluster

Next, we investigate the cluster orientation in our experiments and study the angular dependence of these clusters in the system. We define Ø to be the angle between particles in the v and ∇v plane and θ to be the angle between the v and $\nabla \times v$ plane. See figure 3.8 below.

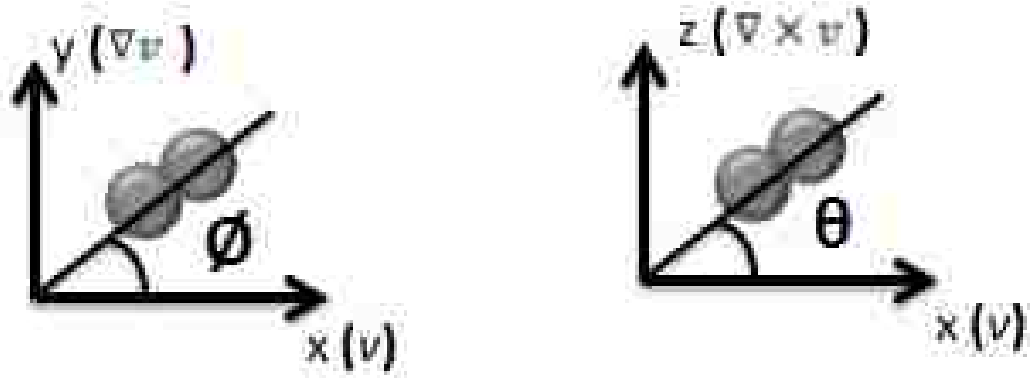

Figure 3.8: *Angular dependence of clusters defined with coordinates as shown. The angle between the x and y planes will be defined as Ø while the angle between the x and z planes will be defined as θ.*

Based on the particle coordinates of the particles constituting to a cluster, we can obtain the average orientation in Ø and θ of all particles in clusters of $N \geq 5$. Note that the positive x axis will be regarded as 0° for both the cases. The average angular dependence was obtained for all the experiments with the various *Pe*. In order to obtain an accurate depiction of the angular dependence, we plot the probability distribution of the neighboring particle orientations in clusters for the $N \geq 5$ averaging all data for all *Pe* experiments. See Figures 3.9 and 3.10.

Figure 3.9 shows the cluster orientation in the Ø direction. All the *Pe* graphs show a similar orientation with higher probability of finding a particle in the the range of ~40° to ~140° about the x axis. If we look closer, the highest probability of finding another particle in a cluster is around the 45° and 135° axis. This is clearly evident at *Pe* = 350, 310, 166 and 103. *Pe* = 230, 51 and 14 also show a similar trend but the 45° and 135° peaks are not as clear as in the other *Pe* cases. Therefore, we can conclude that neighboring particles in clusters preferentially align in the 45° and 135° axis in the x-y plane regardless of the *Pe.* The number of clusters as well as cluster sizes will change with increasing *Pe* causing shear thinning or thickening, but the cluster geometries will preferentially align in the above mentioned axis. In addition, note that our results match with those predicted by Cheng et al. 2011's confocal experiments as well as those predicted by simulations (Bossis & Brady 1985).

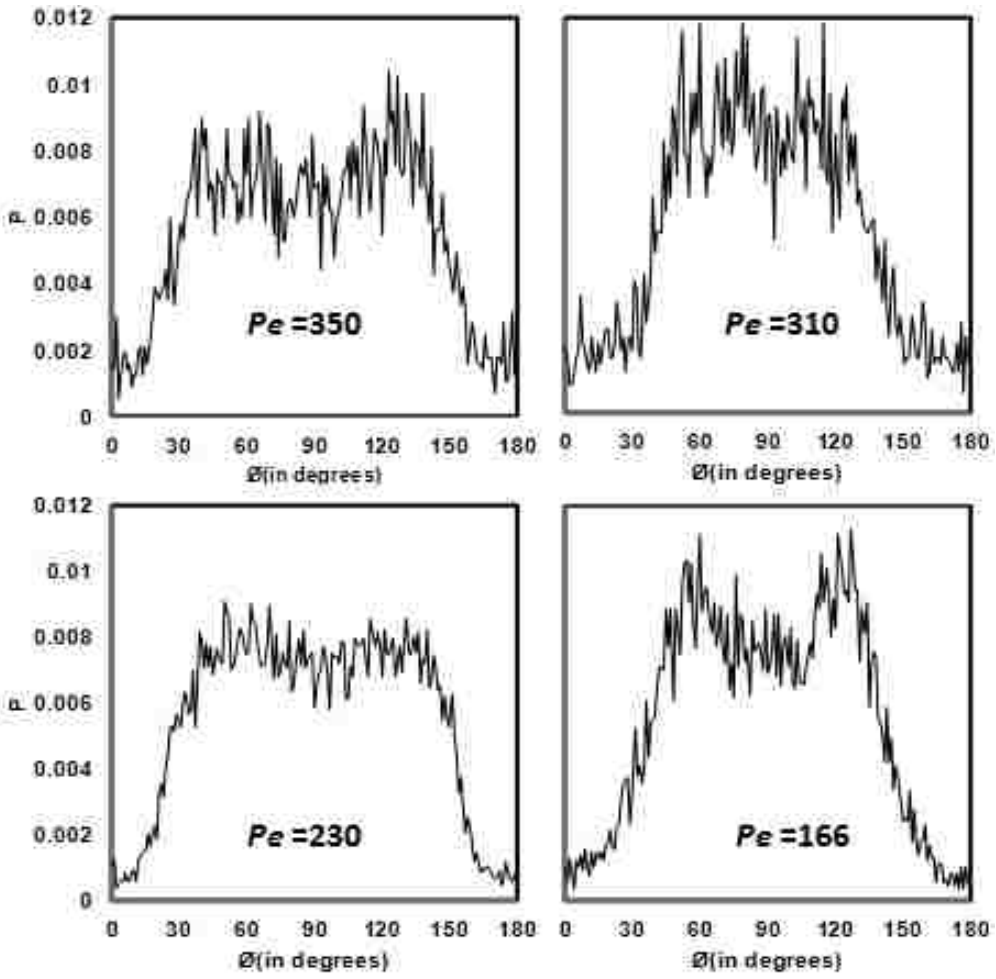
0.012
0.01
0.008
0.006
0.004
0.002
0
P
Pe =350
Pe =310
Pe =230
Pe =166
0 30 60 90 120 150 180
Ø(in degrees)

(i)

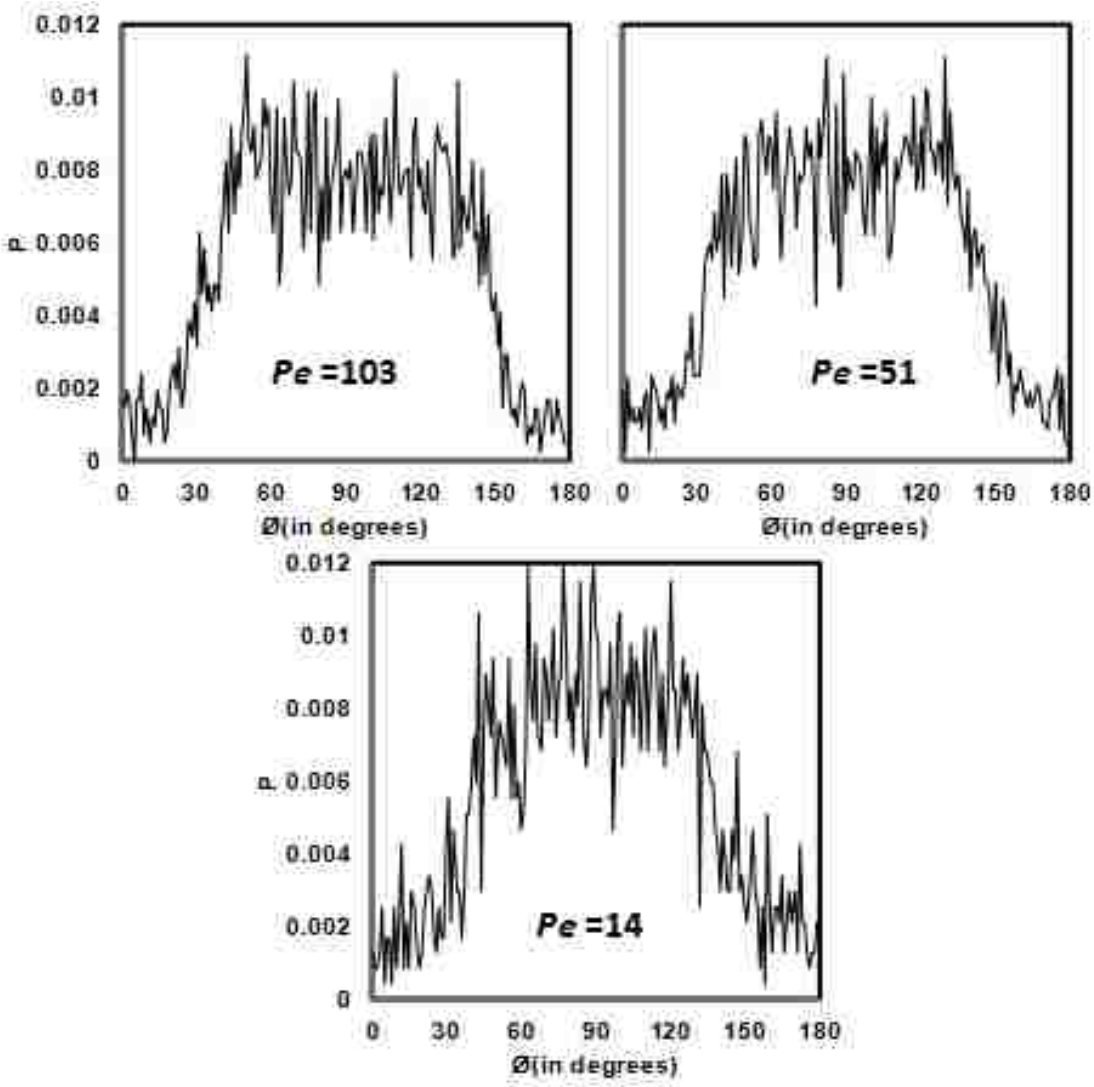

(ii)

Figure 3.9: *Probability of finding a particle having an angle Ø for all particles constituting the* $N \geq 5$ *clusters. (i) and (ii) represent the results for Pe = 350, 310, 230, 166, 103, 51 and 14*

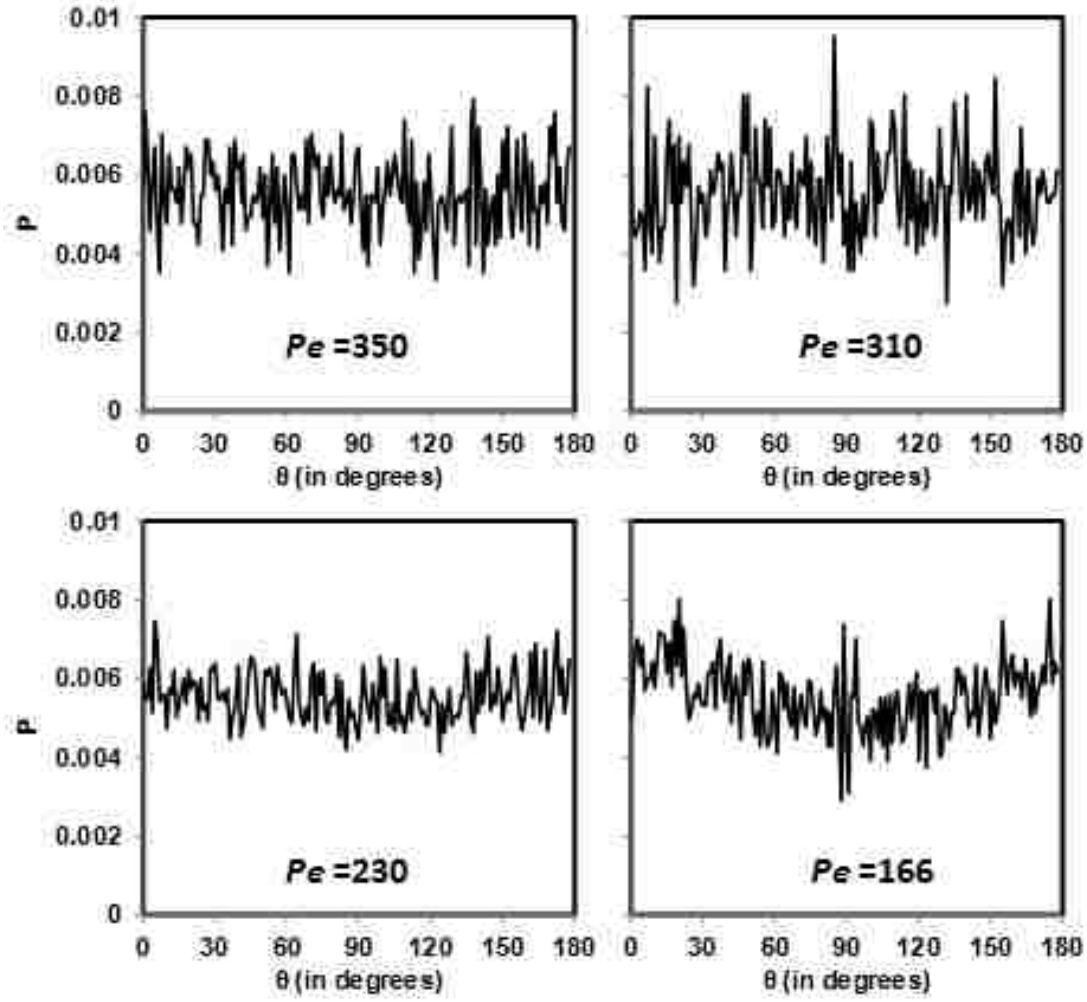
0.01
0.008
0.006
0.004
0.002
0
P
Pe =350
Pe =310
Pe =230
Pe =166
0 30 60 90 120 150 180
θ (in degrees)

(i)

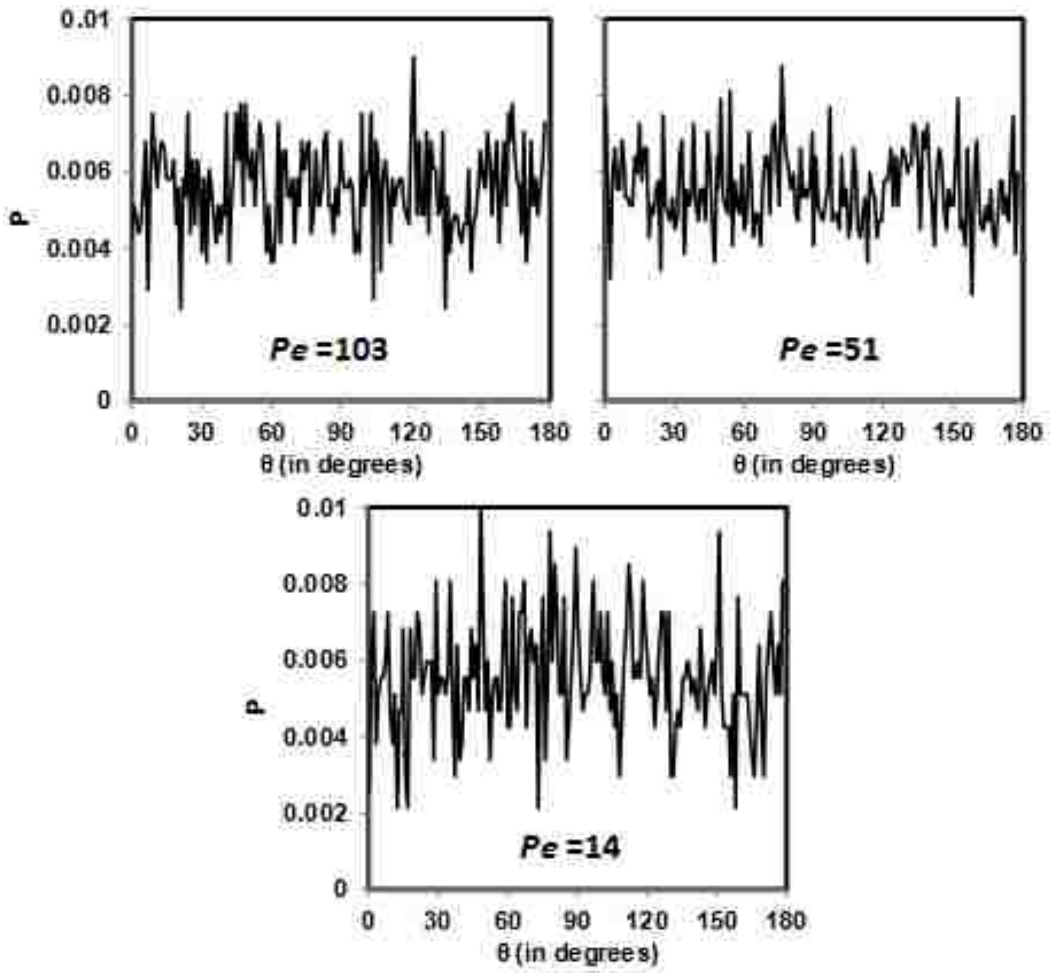

(ii)

Figure 3.10: *Probability of finding a particle having an angle θ for all particles constituting the* $N \geq 5$ *clusters. (i) and (ii) represent the results for Pe = 350, 310, 230, 166, 103, 51 and 14*

However, the probability of finding a neighboring particle in the θ direction remains almost constant from 0° to 180° (See Figure 3.10). The results seen in $Pe = 166$ show slightly more probability in the 0° and 180° (flow direction), but the majority of the results predict that the probability is equivalent from 0° to 180°. Cheng et al. 2011 performed a similar study and they mention that they observe more probability in the flow direction when looking at the x-z plane.

3.3: Conclusions

This chapter discusses the hydrocluster mechanism, which is the well accepted cause for shear thickening behavior. First, we have showed that the order parameter, Ψ_6, remains constant regardless of the *Pe* in our experiments. This is a good indication that our system does not undergo an order-disorder transition as the cause of shear thickening. Suspension microstructure plots show that anisotropy is developed as you increase the *Pe*.

With increasing *Pe*, our experiments indicate a change in relative viscosity showing shear thinning till *Pe* ~50, and then shear thickening from there on. Therefore, we estimate the onset of shear thickening to occur at *Pe* ~ 50 ($\dot{\gamma}_c$ =9). The number of $N \geq 5$ clusters grow exponentially with *Pe* fitting a trendline of $N = 8.7577\, e^{(0.0056Pe)}$ The growth of clusters is not the sole reason for shear thickening. According to our data, we see that the dominance of 5-8 particle clusters is what drives shear thickening in the region of *Pe* being considered. At $Pe \geq 300$ we see an exponential decay of cluster size and also the emergence of 12 or more particle clusters.

Furthermore, this chapter also investigated the angular dependence of neighboring particles in clusters. We clearly see that the neighboring particles preferentially align in the 45° and 135° axis in the velocity-velocity gradient plane. Also, our results indicate that the probability of finding a neighboring particle in the velocity-vorticity plane is constant throughout 0° to 180°. This indicates that there is no preferential alignment of particles in clusters in the velocity-vorticity plane.

Chapter 4

Effect of Smooth and Rough Boundaries on Suspension Microstructure

4.1: Introduction and Background

Wall slip occurs in many industrial and daily applications where flows of complex and multiphase fluids are involved (Yoshimura et al. 1988, Barnes et al. 1995, Larson 1995, Soltani et al. 1988). The causes of wall slip, detection as well as correction for the rheological behaviours of concentrated suspensions have widely been studied by various researchers (Kalyon 2005, Ballesta et al. 2012, Isa et al. 2007, Walls et al. 2003, Cohen et al. 2006). The slip velocity is widely determined from capillary flow using the Mooney Method, which involves changing the surface-to-volume ratio of the capillary die (Mooney 1931). Several other groups have used various rheological techniques to infer the slip velocity (Zhao & Macosko 2002, Jiang et al. 2003, Lee et al. 2009, Park et al. 2010, Zhang et al. 2006). They have estimated the slip velocities using the reduction of measured viscosity in the presence of slip when compared to the value estimated in the absence of slip. To fully describe the flow of fluids that display wall slippage, the

rheological constitutive equations should be supplemented with a relation that describes the slip. The simplest slip law is a linear relation between slip velocity and wall shear stress (Mewis and Wagner 2012);

$$v_s = \beta_{s,N}\sigma(R)$$

Where $\beta_{s,N}$is called the Navier's slip coefficient. It is not a pure material characteristic, as it also depends on the nature and roughness of the wall (Walls et al. 2003, Seth et al. 2008). Often the slip velocity will not behave as linearly as given in the above equation, and therefore, this equation has been modified to fit by a power law,

$$v_s = \beta_{s,P}\sigma(R)^n$$

Where $\beta_{s,P}$ is now the slip coefficient.

The so called slip length, l_s, can be defined as the length scale of the region of much higher velocity gradient. There is a significant amount of depletion in this region which results in a lower viscosity compared to the bulk suspension. The drop in viscosity causes a change in local microstructure of a flowing suspension that can lead to interesting rheological behaviour near the boundaries. Therefore, it is important to gain a microscopic understanding to the nature of such boundary effects on flowing suspensions.

When a suspension flows, the particles cannot physically occupy the space adjacent to the wall as effectively as they can away from the wall. This results in the formation of a relatively thin layer of fluid adjacent to the wall. This relatively thin layer is known as the "Apparent slip layer" or "Vand Layer" (Vand 1948). Wall interactions and roughness can change the apparent flow in such suspensions. This

changes the local rheology in the system and hence is a direct result of suspension microstructure. Meeker et al. 2004 and Seth et al. 2008 studied the apparent flow of concentrated emulsions and other soft particle pastes in the presence of smooth walls and modified surfaces. Recently, Ballesta et al. 2012 and Isa et al. 2007 have also looked at wall slip of colloidal suspensions in smooth and rough boundary conditions.

When sheared within rough boundaries, concentrated dispersions flow uniformly and exhibit a bulk yield stress σ_y (Seth et al. 2008). When sheared within smooth surfaces, the flow is inhomogenous at low stresses - combination of wall slip and bulk flow (Seth et al. 2008). Simple models describing the rheology are discussed. Ballesta et al. 2008 relate the local stress σ to the slip velocity v_s of the colloids along the wall by $\sigma = \sigma_s + \beta v_s$, with βv_s as the hydrodynamic term and σ_s to be the threshold stress. Ballesta et al. 2012 performed series of experiments using a stress-controlled rheometer (cone and plate) with coated (rough) and uncoated (smooth) walls to obtain the rheology in the system. Based on their results, they predict that their suspensions, for which $\phi < \phi_g$ where ϕ_g~ 0.58, exhibit Newtonian behaviour at low shear rates and exhibit Herschel-Bulkley (HB) behaviour at higher shear rates. The HB behaviour is described by $\sigma_m = \sigma_y + \alpha\dot{\gamma_a^n}$, where $\sigma_m$is the measured shear stress, σ_y is the yield stress, and $\dot{\gamma_a}$is the apparent shear rate. But for $\phi > \phi_g$, the suspension exhibit a Bingham like behaviour described by $\sigma_m = \sigma_s + \eta_{eff}\dot{\gamma_a}$, where $\sigma_s$is the threshold stress below which the flow completely stops and $\eta_{eff}$is the effective viscosity characterizing the stress increase in this branch. However, we cannot predict such behaviour from our

experiments using CLSM. Therefore, this chapter will focus on looking at suspension microstructure near the boundaries using experimentally obtained particle locations, and then we will deduce viscometric calculations and present an analogy to previous studies.

The motivation behind the work concerning this chapter was when we observed particles forming structure near the walls no matter what the suspending fluid was. Our experiments indicated that particles immersed in Newtonian fluids (Glycerine/water, Dimethylsulfoxide (DMSO)), and viscoelastic fluids (Polyacrylamide solids dissolved in Glycerine-water, Lambda DNA in DMSO) showed order in structure near the boundaries in our microchannels. See Figure 4.1.

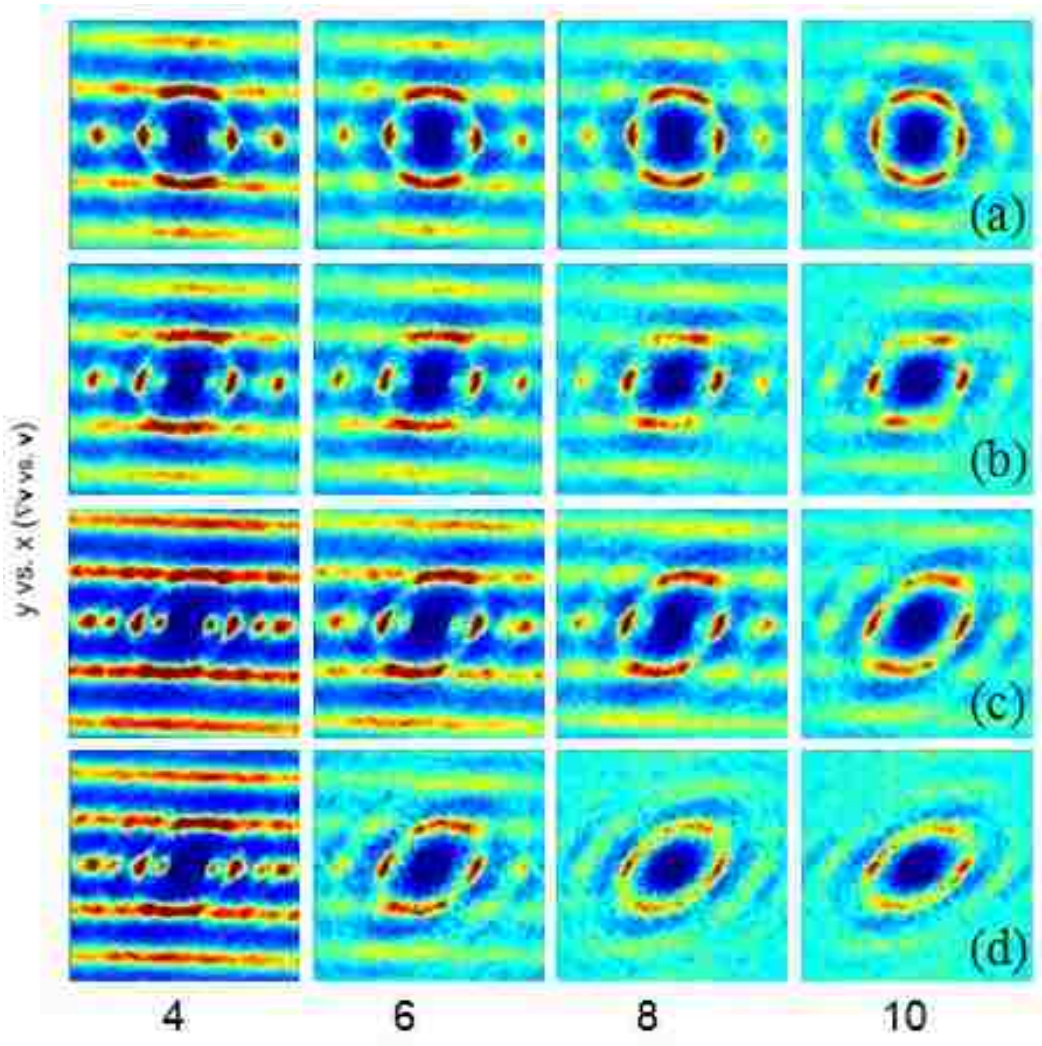

Figure 4.1: *Structure and particle chaining in the flow direction observed near the walls. The g(r) plots correspond to 4,6,8 and 10 μm away from the wall. The plots correspond to (a) Glycerine-Water Suspension at* $\dot{\gamma}=9\ s^{-1}$*, (b) DMSO suspension at* $\dot{\gamma}=12\ s^{-1}$*, (c) PAM Dissolved in Glycerine-Water at* $\dot{\gamma}=20\ s^{-1}$ *and (d) λ-DNA in DMSO at* $\dot{\gamma}=25\ s^{-1}$*.*

Boundary effects may seem obvious but complications in rheological behaviour may arise when considering confined systems of flows. Our experiments indicate that boundary effects propagate as much as 6 μm away from the boundary itself. Smooth and rough boundaries result in different flow behaviour for a flowing suspension, changing the local microstructure and rheology in each of the individual cases. Thus, the main goal of this chapter is to highlight why boundary effects should be considered important in various flows of complex fluids especially when considering confined systems of flows.

4.2: Results & Discussion

4.2.1: Experimental Technique

In this chapter, we compare effects from smooth and rough boundaries on suspension microstructure using CLSM. A suspension containing screened 1 μm SiO_2 in Dimethyl Sulfoxide (DMSO) is used for the study. The suspension is flowed in a PDMS microchannel with dimensions of 4000 μm **X** 500 μm **X** 94 μm (L **X** W **X** H). We characterize a smooth boundary in our channels as a plain glass wall while a rough boundary is considered to be a monolayer of Silica spheres deposited on a glass slide using Vibration-Assisted convective deposition (Muagnapoh et al. 2013). See Figure 4.2.

The main experimental challenge in this study was to obtain comparable data when considering the smooth and rough boundary conditions. Previous studies have used techniques such as spin coating to introduce particles to be deposited on the walls (Besseling et 2009, Ballesta et al. 2012). In addition, surfaces were modified by scotch tape polymer surfaces, Polymethylmethacrylate (PMMA) coatings, gold surfaces and silicon surfaces (Seth et al. 2008, Isa et al. 2007). In our experiments, we coat Silica spheres on to a glass slide and this introduced roughness reduces wall slip. Figure 4.3 below shows the velocity profiles obtained for two different shear rates of flow for both the Smooth and Rough boundaries.

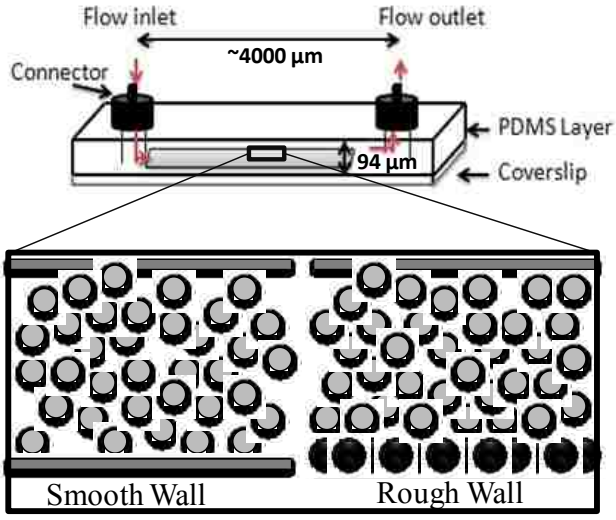

Figure 4.2: *Comparison of Smooth and Rough Walls in the PDMS Microchannel. A Smooth Wall is characterized as a plain glass slide while a rough wall contains a monolayer of 1 µm Silica spheres deposited on to the glass slide.*

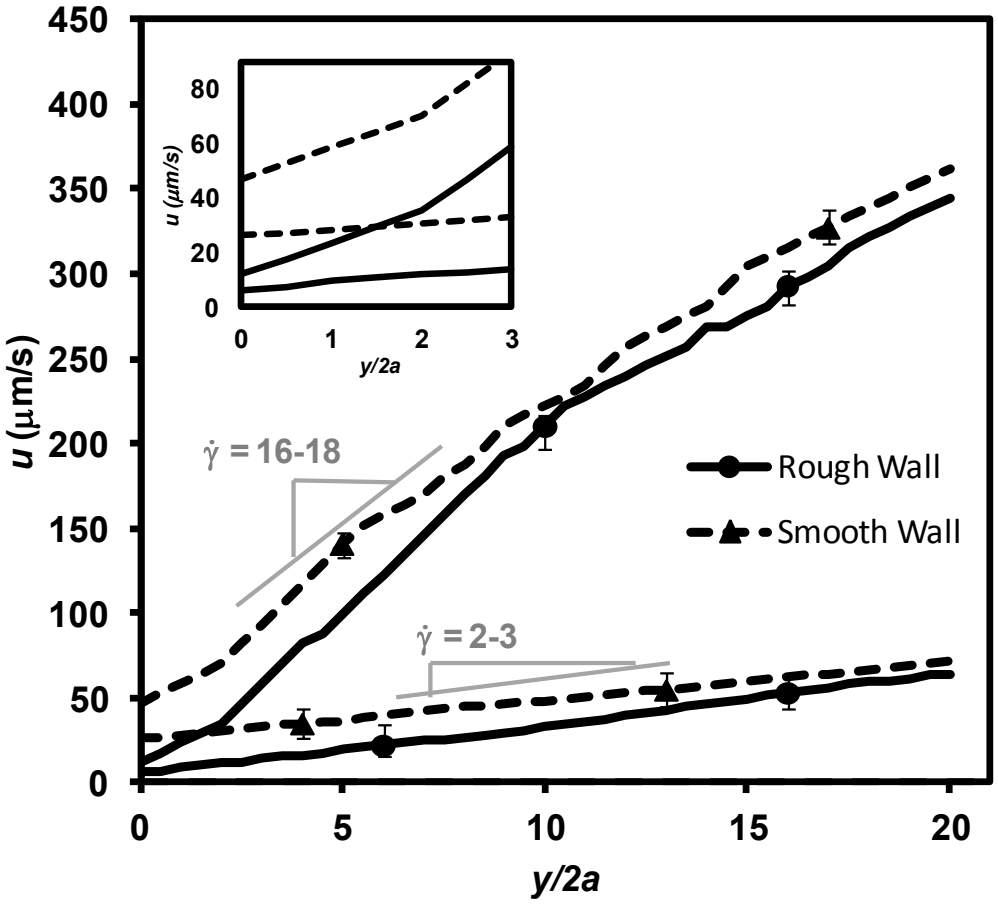

Figure 4.3: *Velocity profiles of the flowing suspension for two different shear rates for the smooth and rough boundaries as a function of distance from channel bottom (y) normalized by particle diameter (2a).*

We assume a constant shear rate for the velocity profiles shown in Figure 4.3. The velocity can be given as $u = v_s + \dot{\gamma} y/2a$. As seen in Figure 4.3, we clearly see that wall slip has been reduced by the rough boundaries. Note that the distance is zero at the first layer of moving particles next to the channel bottom normalized by particle diameter. When $\dot{\gamma}$=2-3 s^{-1}($Pe \sim 2$), we see that particles near the channel bottom faces slip with velocities of about 27 μm/s for the smooth walls case and 6 μm/s for the rough walls case. When the shear rate is ramped up to $\dot{\gamma}$=16-18 s^{-1} ($Pe \sim 20$), the slip velocity increases to 47 μm/s in smooth walls while the rough walls case results in a slip velocity of about 12 μm/s. Even though the flow profiles look very similar for both the cases, the resulting microstructure closer to the boundaries show more structural order for the smooth walls case. In order to investigate this, we perform experiments to analyse the local microstructure near the walls for smooth and rough boundaries.

4.2.2: Suspension Microstructure

To quantify suspension structure we use the pair distribution function, g(r), obtained by integrating the N-particle configuration probability, $P_N(x_1, x_2 \cdots, x_N)$ by N-1 times. Then we obtained 2D plots of the three orthogonal planes of the g(r) from 4-10 μm at every 2 μm from the channel wall to demonstrate the boundary effects on suspension structure in both the smooth and rough boundary cases. Note that we are not investigating the structure between 0-4 μm away from the wall because g(r) is calculated for every 3 particle diameters away from each reference particle and

therefore would not provide accurate results near the wall. Figure 4.4 shows g(r) plots for y vs. x ($\nabla v\ vs\ v$).

Figure 4.4 shows particles chaining in the direction of flow dominantly till about 4 μm from the wall for the smooth walls case. This structure starts dissipating from about 6 microns away from the wall as it approaches an anisotropic behaviour due to shear. Importantly, when the rough walls are introduced the microstructure seems to have a purely anisotropic nature regardless of the distance away from the wall. Note that with wall slip been reduced for this condition, we notice no particle chaining at all closer to the rough boundaries. The structures also look similar in both the boundaries at 8 microns away from the wall. The same level of anisotropy in the y vs. x z ($\nabla v\ vs\ v$) plane is an indication that the bulk rheology is the same at this point onwards. A similar trend is observed looking at the y vs. z ($\nabla v\ vs\ \nabla \times v$) plots (See Figure 4.5). The order seems to resemble almost a crystalline structure at 4 microns away from the wall for the smooth walls case. But when you look at the rough walls condition, a perfectly isotropic structure is seen. Order is observed for both the shear rates at 6 microns away from the wall for the smooth boundary.

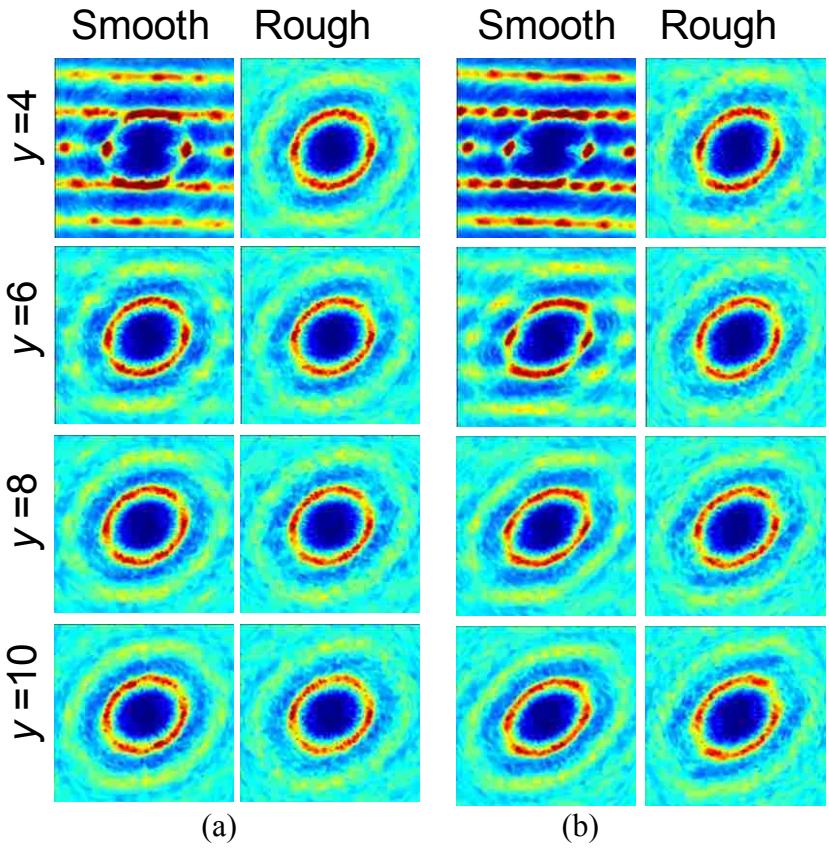

Figure 4.4: *g(r) plots in the y vs.x ((∇v vs v) plane. Plots correspond to (a) $\dot{\gamma}$=2-3 s^{-1} (Pe ~ 2), (b) $\dot{\gamma}$ = 16-18 s^{-1} (Pe ~ 20) for both the smooth and rough walls cases.*

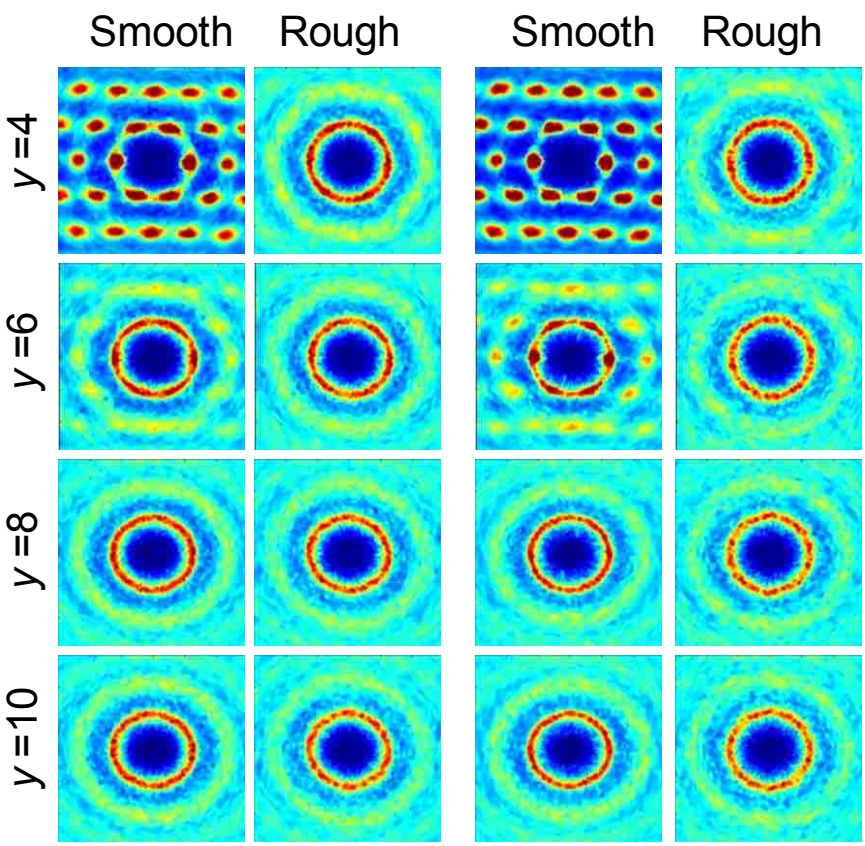

(a) (b)

Figure 4.5: *g(r) plots in the y vs.z ($(\nabla v$ vs $\nabla \times v)$ plane. Plots correspond to (a) $\dot{\gamma}$ =2-3 s^{-1} (Pe ~ 2), (b) $\dot{\gamma}$ = 16-18 s^{-1} (Pe ~ 20) for both the smooth and rough walls cases.*

Some ordering is evident at 6 μm away from the boundary especially at the higher shear rate. This suggests that boundary effects can be dominant till about 6 microns away from the boundary altering microstructure. At 8 and 10 μm away from the wall, the structures look very similar (correspond to the bulk structure) indicating that that there is no boundary effect at this point. The convergence of the anisotropic structure in y vs x. starting at 8 μm is a clear indication to the similar rheological behaviour of the suspension at this point upward. A slightly more anisotropic behaviour is observed for the high shear rate case as expected.

It is clear that the boundary has an effect on suspension microstructure. Let us now investigate the viscometric functions so that we can deduce to more understanding as to what may be going on near the smooth and rough boundaries.

4.2.3: Viscometric calculations

In order to understand these effects further, we computed the relative viscosity, first and second normal stress differences using the method elaborated by Foss and Brady (2000) as highlighted in the introduction section of this thesis report.

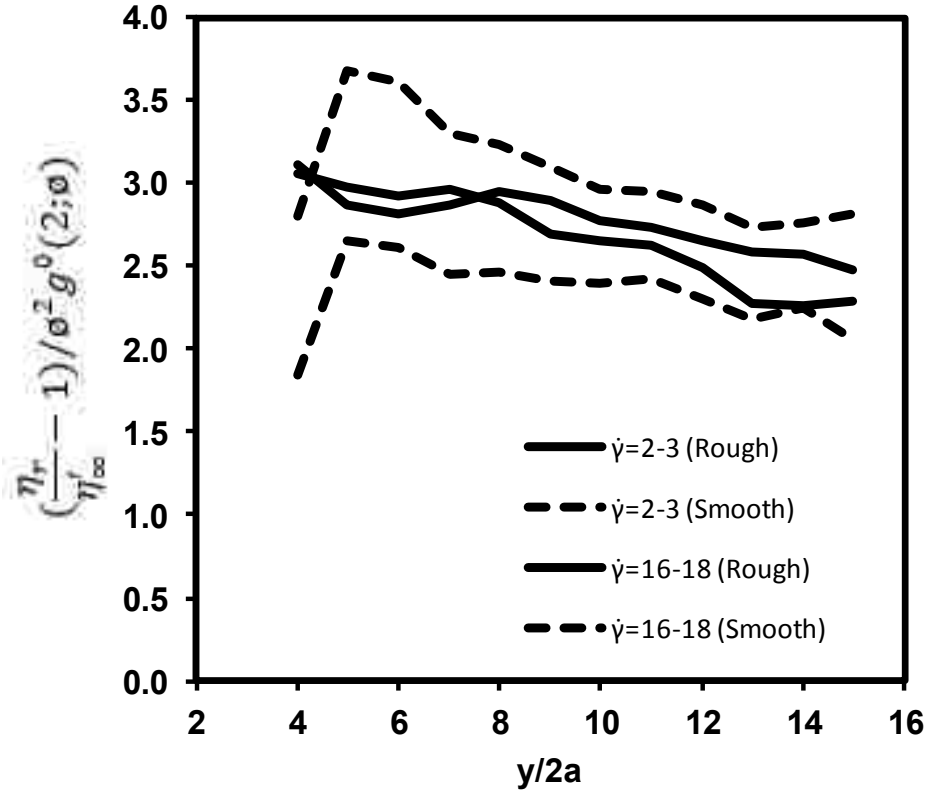

Figure 4.6: *Scaled relative viscosity plot. The data are plotted for both smooth and rough boundaries as a function of normalized distance away from the boundary.*

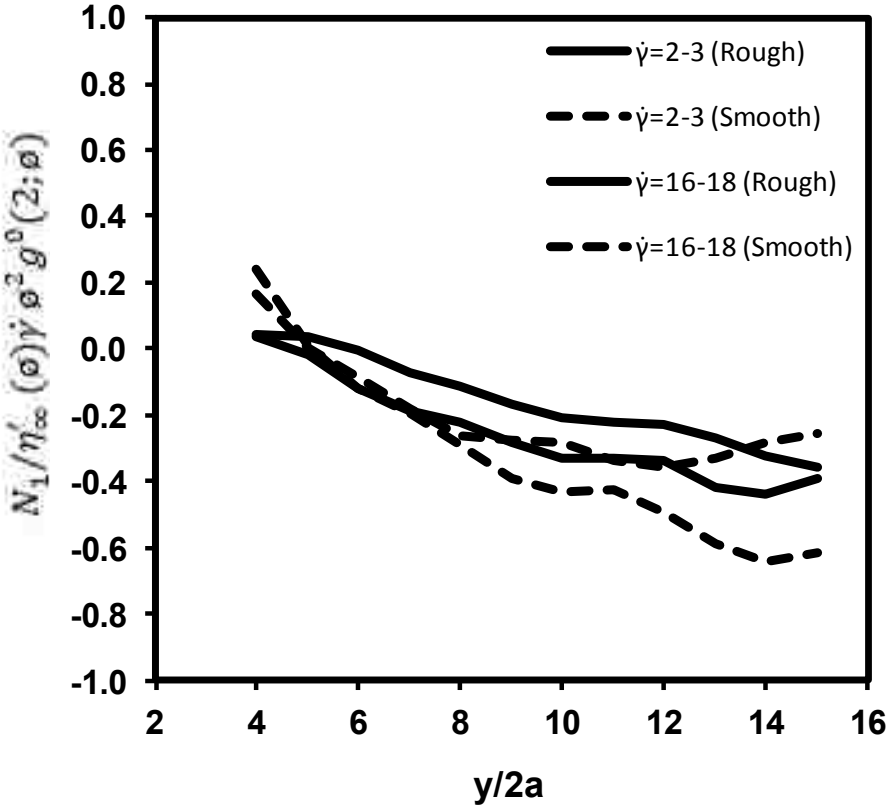

Figure 4.7: *Scaled First Normal Stress difference. The data are plotted for both smooth and rough boundaries as a function of normalized distance away from the boundary*.

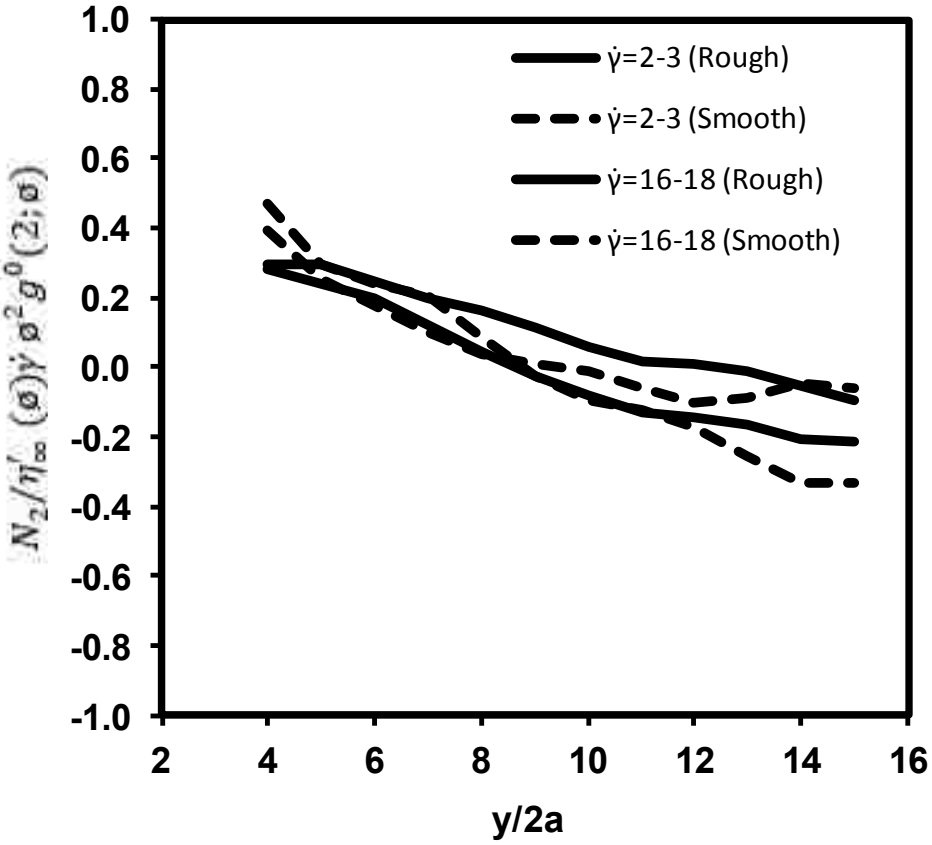

Figure 4.8: *Scaled Second Normal Stress Difference. The data are plotted for both smooth and rough boundaries as a function of normalized distance away from the boundary*.

Figure 4.6 shows the relative viscosity plot obtained from g(r)s as you go further away from the channel bottom. You clearly notice the lowered viscosity near the wall for the smooth walls case. This is due to the significant amount of depletion caused near the wall that results in a lowered viscosity. We are able to accurately capture this phenomenon from our experiments. However this trend does not seem to apply for the rough boundaries case. With the reduced slip velocity, there appears to be no depletion near the wall when rough walls are introduced to the system. The viscosity starts off high and reduces as you go further away from the channel bottom. Note that the shear rate profile or *Pe* number is approximately constant throughout the region of interest here. Therefore, this can be accounted to be an effect purely from the boundaries.

First and second normal stress differences for these systems are shown in figures 4.7 and 4.8. Although all four scenarios show similar trends in terms of both the first and second normal stress differences, we would like emphasize the fact that the first Normal stress difference is positive till about 6 μm away from the wall. Shear driven suspensions of this nature are known to have a negative N1 due to the compressive nature in shearing suspensions (Foss and Brady 2000). Yet, we see that due to the boundary effects, the first normal stress difference is positive closer to the wall. We suggest that due to the wall boundaries, the particles push against each other that result in a positive N1. In smooth boundaries, this positive N1 results in particle chaining in the flow direction and order as shown in our g(r) plots. But the rough condition disrupts this order in terms of the physical arrangement of particles flowing near the wall. A similar trend is observed for the second normal stress difference, but not much can be

concluded from the second normal stress difference data for these systems.

Previous studies by Foss & Brady 2000, show that the relative viscosity, first and second normal stress differences varies by shear rate or *Pe*. So it is important to note that for our system, we analyse these viscometric functions as a function of distance from the channel bottom or the wall assuming that the *Pe* is constant throughout the region being considered in this study. Realistically, we need to keep in mind that there are variations to the local shear rate and thus changes the local *Pe* in the system. This is evident in the variations of the viscometric functions calculated as a function of wall distance. The fact that N1 and N2 behaves similarly for all the four cases actually serve as a good check that the change in structure evident closer to the walls is more of an alteration to the physical arrangement of particles. The change in arrangement here would affect the apparent slip layer closer to the walls, thus change the local viscosity near the boundaries. The depletion effects, relative viscosity at the boundary, the local microstructure as well as the slip velocity are all inter related based on this study.

4.2.4: Lubrication Slip Layer

Furthermore, it is important to investigate the role of the apparent slip layer or lubrication layer near the boundary. Meeker and co-workers (2004) and Seth et al. 2008 discuss the theory of elastohydrodynamic slip with short range forces in their studies with microgel pastes. They also state that the slip of the particle is due to the lubrication caused by the surrounding solvent between the particle and the boundary. This lubricated film thickness is a function of slip velocity and also can be estimated from experimental data. We make a similar argument to Seth et al. 2008; the particle stress is by the drag experienced due to shear flow in the lubricated solvent layer. Then, $\sigma_p \sim (\eta_S V_S / \delta)$ near the boundary. The lubrication film thickness, δ can be estimated by $\sim (\eta_S V_S / \sigma_p)$. From our experiments, we already know the slip velocities for the particles near the walls. η_S is the solvent viscosity for DMSO and is approximately 2×10^{-3} Pa.s. We do not know shear stress, σ, in our system however. But we can estimate the particle stress contribution from our stress calculations based on Foss & Brady 2000. The sum of the hydrodynamic and Brownian contribution to the stress will give an estimate to the total particle stress that we are able to calculate from our viscometric data. σ_p given in Table 4.1 corresponds to the particle stress obtained near the boundary for each of our experimental studies.

	V_s (μm/s)	η_s (Pa.s)	σ_p (Pa)	δ (nm)
$\dot{\gamma}$ =2-3 s^{-1}(Smooth)	27	0.002	1.25	43.2
$\dot{\gamma}$ =2-3 s^{-1}(Rough)	6	0.002	1.19	10.1
$\dot{\gamma}$ =16-18 s^{-1}(Smooth)	47	0.002	0.79	119.0
$\dot{\gamma}$ =16-18 s^{-1}(Rough)	12	0.002	0.75	32.0

Table 4.1: *Estimating the lubrication thickness, δ, from experimental data. V_s correspond to the slip velocity, η_S the solvent viscosity and σ_p the particle stress estimated by the addition of the Hydrodynamic and Brownian stress contributions.*

The δ values we have predicted are in the same range as those predicted by Meeker and co-workers and Seth et al. 2008. Based on our analysis here, we can see that the reduction in lubrication layer thickness is due to the introduced roughness in the channel walls. This causes a reduction in slip velocity.

It is clear that the lubrication thickness, δ is proportional to the slip velocity V_S based on our experiments. I would also like to point out that based on our experiments, the structural order for the smooth boundaries is only observed up to 6 μm away from the wall. In chapter 3 of this thesis, we looked at the formation of hydroclusters for 7 different shear rates, giving a *Pe* range from 14 to 350. These experiments were carried out under smooth boundaries, and we neglected the near wall effects for our hydocluster study. So now, let us investigate the respective viscometric calculations utilizing the data from Chapter 3 of this thesis so that we grasp a better understanding of boundary effects.

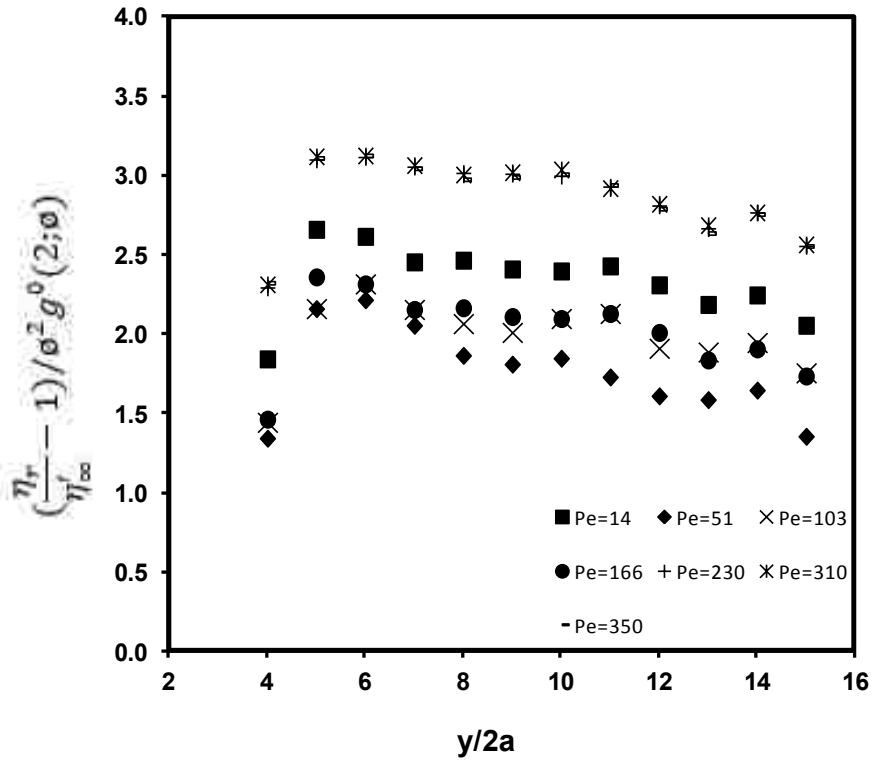

Figure 4.9: *Scaled relative viscosity plot. The data are plotted for smooth boundaries for Pe =14, 51,103, 166, 230, 310 and 350. The data are plotted as a function of normalized distance away from the boundary.*

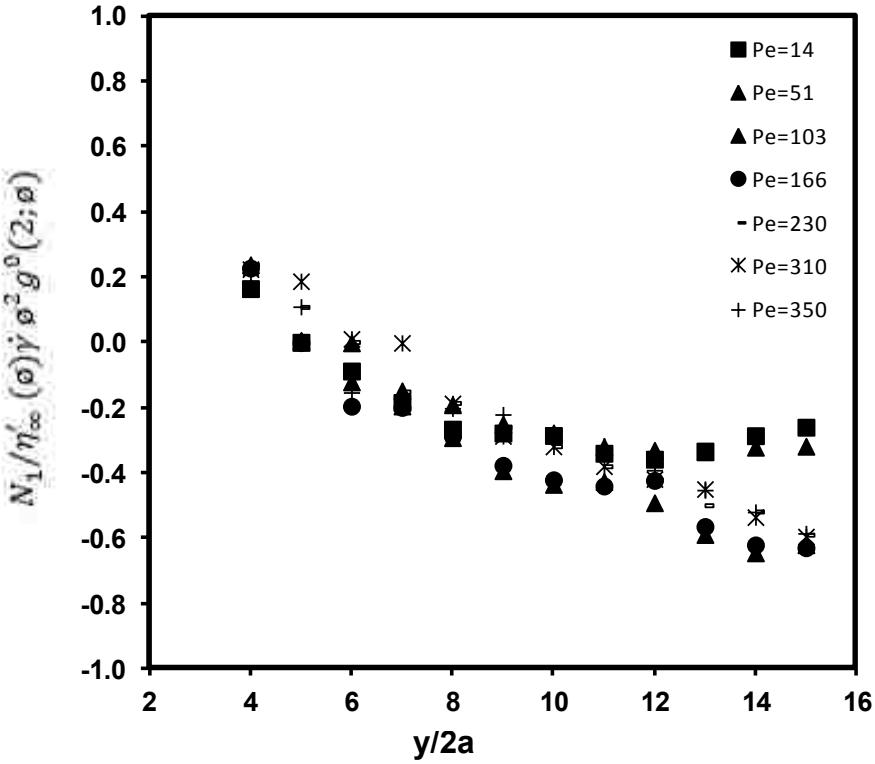

Figure 4.10: *Scaled First Normal Stress Difference. The data are plotted for smooth boundaries for Pe =14, 51,103, 166, 230, 310 and 350. The data are plotted as a function of normalized distance away from the boundary.*

Figures 4.9 and 4.10 show the Relative viscosity plot and First Normal stress difference for the different *Pe* we obtained in Chapter 3 of this thesis. It is clearly seen that in Figure 4.9, the depletion effect is evident till about 6 microns away from the channel boundary. The lowered viscosity near the boundary is a reconfirmation that the boundary results in this depletion effect. Since our *Pe* range is from 14 to 350, we cannot really predict the dependence on shear rate or *Pe* to this boundary effect. Similarly, the first normal stress difference plotted in Figure 4.10 seem to agree with our results analysed previously in this chapter. We see that N1 is positive closer to the boundary and becomes negative after 6 microns away.

Our analysis in this chapter has made it clear that boundary effects are important when flows in confined systems are concerned. Previous studies have demonstrated wall slip and its effects on rheology based on traditional rheometer settings. We have demonstrated that CLSM can provide a useful technique in observing how the structure changes in a smooth and a rough boundary. Relative viscosity, first and second normal stress differences are also deduced from g(r). The depletion effect has been observed directly from our calculations, especially for the smooth boundary case. The slip velocities are greater for the smooth boundaries due to the higher lubrication layer thickness between the boundary and the immediate adjacent particle. This causes a reduction in viscosity near the boundary. When the rough boundaries are introduced, it reduces the lubrication layer thickness near the wall. Therefore, wall slip reduces. Hence, the depletion effect is not as great as observed for the smooth boundary case. The rough boundaries also alter the physical arrangement of particles near the

boundaries and therefore, we do not see any structural order near the boundaries.

4.3: Conclusions

Results following suspension microstructure indicate that boundary effects can be prominent near the walls even up to about 6 microns away from the wall. Smooth walls influences in particle chaining in the direction of flow. When roughness is introduced on to the boundaries, wall slip is reduced and thus, disrupts local structure of the flowing suspension. Therefore, particle chaining is eliminated and a purely anisotropic structure is observed even near the rough boundary.

Wall slip causes a significant amount of depletion near the walls. This effect results in a lowering of suspension viscosity near the wall compared to the bulk. In rough boundaries, the depletion effects are not very prominent. The near wall viscosity remains almost constant with the bulk viscosity resulting in a microstructure similar to the bulk behaviour. Furthermore, the first normal stress differences show that N1 is positive near the wall. This behaviour is deviant from the compressive nature that is usually present in flowing suspensions. We also believe that the addition of roughness onto walls reduce the lubrication layer thickness of the solvent layer formed between the boundary and the particle closest to the boundary. Since slip velocity is proportional to this lubrication layer thickness, we have showed that the reduction in this thickness is achieved by the addition of rough walls and hence reduces slip velocity.

Boundary effects should be considered important in flows of complex fluids as demonstrated in this article. Especially in confined systems of flows, these effects can be dominant and may influence in the rheological behaviour of the flowing suspension.

Chapter 5

Microstructure of suspension flow in a well structured micro-porous medium

5.1: Introduction and Background

Suspension flow in porous networks occurs in many processes including filtration (Sherard et al. 1984, Datta et al. 1988), water and oil extraction processes (Muecke 1972, Gruesbeck et al. 1982) as well as in biological systems (Sanderson et al. 2001). The complications of flow can result in desirable or unwanted consequences in such processes. Therefore, it is important to study the underlying mechanical properties in order to achieve process optimization.

Fluid flow in porous media often involves the migration of fine particles. These particle migration through porous networks reflect interplay between various particle-particle interactions, particle-pore wall interactions at different stages through the network. Previous studies have looked at clogging in porous networks (Valdes et al. 2002; 2007; 2008, Goldztein et al. 2004, Kampel et al. 2008; 2009), model flows in such networks (Choi et al. 2008, Vasin et al 2010, Pan et al. 2013) and a few studies

have looked at the rheology of such flows for specific purposes (Olanrewaju et al. 2014, Comba et al. 2011).

Flow in porous media can affect the microstructure and rheology of a suspension. Microstructure in this context refers to how particles arrange their locations based on the geometry in which they are in, thermal fluctuations and inter-particle forces. A migratory particle inside a porous medium experiences physical interactions with the pore surfaces, fluid and other particles. Such interactions can change depending on the location in which the particle is in the porous medium. Therefore, the main objective of this chapter is to utilize CLSM to obtain the microstructure of the suspension in a porous network based on experimentally obtained 3D particle positions. In addition, since I discussed about boundary effects in Chapter 4 of this thesis, this chapter also serves to investigate how these boundary effects come into play in real process flows such as in a porous medium. Suspensions flowing in various geometries can also give rise to interesting phenomena. The main motivation to analyze the microstructure in porous media in this chapter was the observation of strings in a highly concentrated suspension (ϕ = 0.4~0.5). Particles form strings in the direction of shear generated by the pores. This phenomenon is only evident at very high concentrations of particles. We do not observe string formation at concentrations of about ϕ = 0.2~0.3. In this chapter, we investigate the particle string formation around pores in a highly concentrated system and suspension microstructure at different locations in the medium.

5.2: Results & Discussion

5.2.1: Experimental Technique

In order to accomplish this, we have fabricated a microfluidic device (as discussed in chapter 2 of this thesis) with well-structured pores. See Figure 5.1 (a) & (b) below. The microchannel was fabricated using a silicon wafer mask containing a porous structure. The wafer was obtained from Prof. Xuanghong Cheng's Lab in Materials Science at Lehigh University. The post diameter was 780 μm with a distance between the posts being approximately 80 μm. The post height was 94 μm.

The suspension was flowed through the device and flow streamlines similar to Figure 5.1 (b) were noticed. Microstructure evolvements upstream and downstream were investigated as shown in Figure 5.1 (b).

Prior to proceeding with the microstructure results, it is important to note that the flow direction changes as the flow progresses through the medium. The arrows in figure 5.1 (b) represent the directions of the velocity. The velocity gradient in this case will be in the same plane as the velocity because the shear is driven in the same plane as the velocity thus creating a change in velocity in that same plane. Therefore, the vorticity direction will be in the perpendicular direction to the velocity-velocity gradient plane. Measurement scans were taken covering the central region of the channel height in order to avoid boundary effects as well as recirculation flows. Let us investigate how the structure evolves in the velocity-velocity gradient direction in this model well structured porous medium.

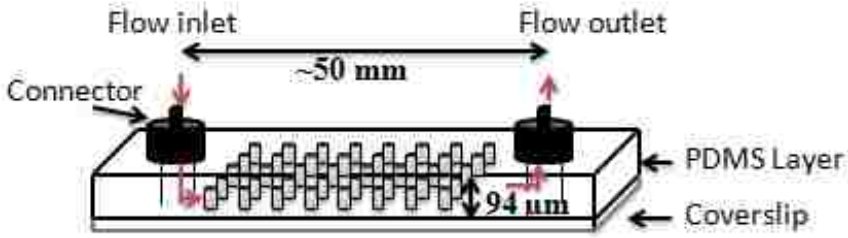

(a)

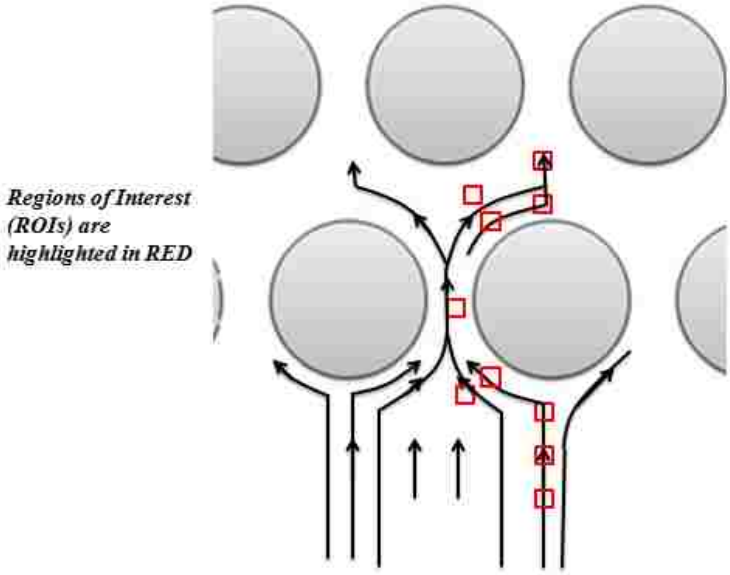

(b)

Figure 5.1: *(a) Side view of the microchannel with porous network. The cylindrical pores are of 94 µm height with a 780 µm diameter. The distance between two pores is roughly 80 µm; (b) Top view of porous network highlighting the Regions of Interests (ROIs) investigated in this study*

5.2.2: Suspension Microstructure in upstream and downstream flows

Prior to proceeding with the structure results, let us briefly investigate the physics underlying migrating particles in porous networks based on some previous studies. The severe reduction in flow conductivity in a porous network due to the excessive retention of migratory particles is referred to as clogging (Valdes et al. 2007). Clogging typically develops near entry ports when suspensions are pumped in or near exit ports when fluid extraction prompts particle migration in the porous network and has been investigated in various studies (Valdes et al. 2002; 2007; 2008, Goldztein et al. 2004, Kampel et al. 2008; 2009). Due to inertial effects migratory particles will deviate from streamlines and collide with pore walls and neighboring particles. These collisions will increase with increasing velocity of the fluid in the porous medium. The delay between particle and fluid displacement is referred to as retardation. It is also known that the local concentration of particles gradually increases as it flows through the network (Valdes et al 2007). As a result the average velocity of the particles is sometime different from the average velocity of the suspending fluid.

A migratory particle in a fluid in a porous medium experiences a drag force, and kampel et al. 2009 approximates this force as $F_D = 6\pi\mu r_p(v^* - x')\boldsymbol{e}$ where μ is the fluid viscosity, r_p is the radius of the particle, v^* is the fluid speed. x(t) was defined as the distance between the particle and the upstream end of the channel at time t. The inertial force experienced by a migratory particle in the flow direction is simply the mass multiplied by acceleration. $F_I = m_p(dv_p/dt) = m_p\big(dv_p/dx\big) \times (dx/dt)$.

Therefore, differences in mass density and spatial variations of fluid velocity in a porous network can cause particle deviations from streamlines and collisions.

We conducted experiments to study how the microstructure progresses in a porous medium. Figure 5.2 and 5.3 below show how the microstructure evolves both upstream and downstream for both the low and high volume fraction conditions of the suspension. Figure 5.2 shows that the g(r) rings are isotropic regardless where the region of interest is. However, when you introduce a high volume fraction suspension into the system, structure is evident furthest away from the obstacle giving a volume fraction of ϕ=0.48. This structure dissipates as you approach the obstacle in front because the flow distributes itself evenly and results in an isotropic ring. Also, note the change in volume fraction in our results. We see that the volume fraction increases as the flow progresses through the porous medium both in the low and high volume fraction cases. This is consistent with Valdes et al. 2007 predictions. In addition, note that we have considered the flow behavior upstream to have a negative extensional rate because the flow component can be considered compressible in the direction of flow due to the obstacle in front. Once the obstacle has been over passed (downstream), the flow component undergoes extension in the direction of flow, thus having a positive extension.

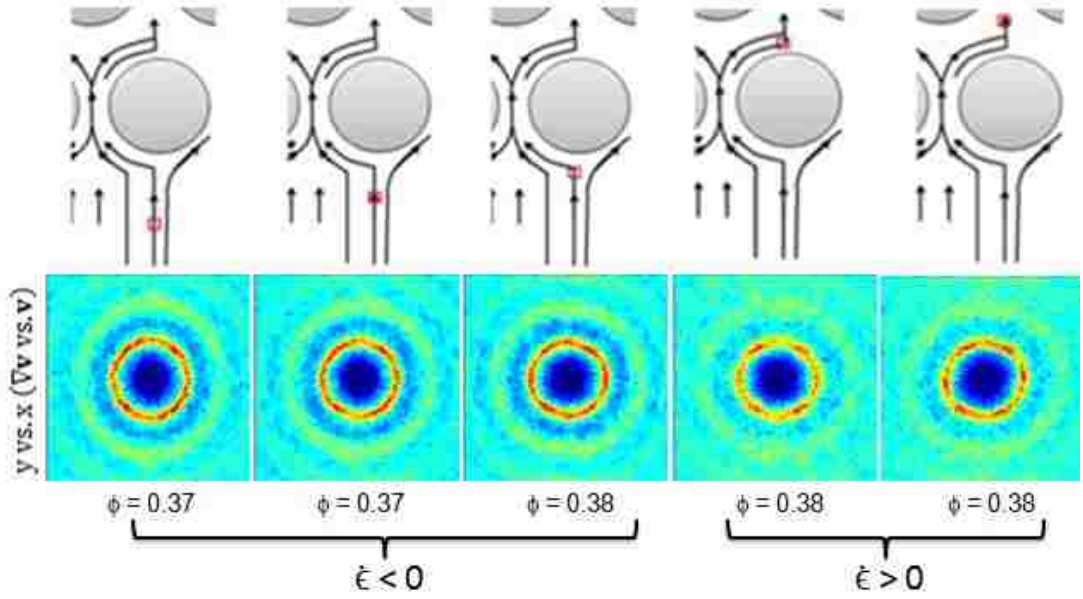

Figure 5.2: *g(r) plots in the y vs. x plane for the upstream and downstream flow cases. The volume fraction of the suspension is low and therefore do not observe much structure. The extension of the flow component is negative before approaching the obstacle and is positive downstream.*

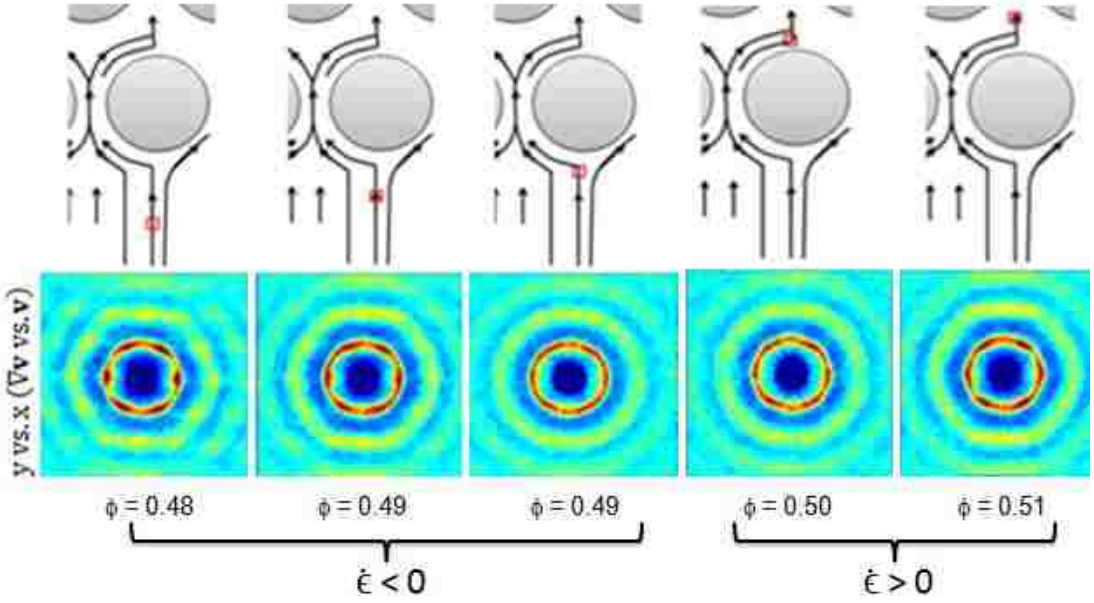

Figure 5.3: *g(r) plots in the y vs. x plane for the upstream flow case. The volume fraction of the suspension is high and we observe a change in structure as the flow progresses toward the obstacle. The extension of the flow component is negative upstream and is positive in the downstream flow case.*

When the flow is around the obstacle, a mixed flow behavior is resulted due to complexity of the flow. As mentioned in the introduction of this chapter, a migratory particle entering a porous network undergoes interactions with the pore surfaces and other particles. Collisions between particles and pore surfaces result in these particles to deviate out of the predicted streamlines and we define this as a mixed flow behavior from here on of this chapter. In figure 5.2 and 5.3 we saw isotropic rings in the velocity-velocity gradient plane. Suspension flow is homogenous at these ROIs and we do not observe anisotropy. The shear components generated from the pore surfaces are minimal at these points. Since we are also considering data at the central region of the channel we can disregard the shear component from the top and bottom walls of the channel. Therefore, we notice isotropic behavior. However, for the flows around the posts a certain degree of anisotropy is seen because at these ROIs, the shear component from the post walls will dominate. Keeping in mind that there is a mixed flow behavior present at the ROIs around the post, let us investigate the structure results herein.

Our results indicate that an anisotropic ring is formed when the suspension flows around the obstacle. See Figures 5.4 and 5.5. The microstructures upstream and downstream essentially reflect an anisotropic behavior in which you see the intensity of the nearest neighbor ring getting intensified along the compressive axes and less intensified along the extensive axes. The anisotropy is greater for the low volume fraction case than for the higher volume fraction case. With low particle concentration, a migratory particle is able to flow more freely in the medium. Under shear, this particle will have a greater probability of finding another neighboring particle along the

compressive axes than the extensive axes and then will depart downstream. This anisotropy suggests that the shear flow from the walls of the post dominate, but for an instance the fourth g(r) from the left in figure 5.4 and the second g(r) plot from the left in figure 5.5 do not show as much anisotropy. This could be the result of a mixed flow behavior. The collisions of particles that occur between the pore surfaces and other particles result in a non pure shear flow behavior at certain regions. Particle motion deviating from the streamlines results this behavior and thus we do not observe much anisotropy at these ROIs. However, in both the low and high volume fraction cases, we can deduce that the anisotropy is greater closer to the post wall as opposed to away from the post wall. This is due to the shear generated from the wall of the post. Also the mixed flow behavior occurring away from the wall of the post results in a reduction of anisotropy. For the high volume fraction case, more structure away from the post than closer to the post is evident for both upstream and downstream. The explanation for this effect can be thought of as the same as the straight flow case, where away from the obstacle, each particle is affected by other particles and the obstacle, thus gives more order. This is captured in our experiments.

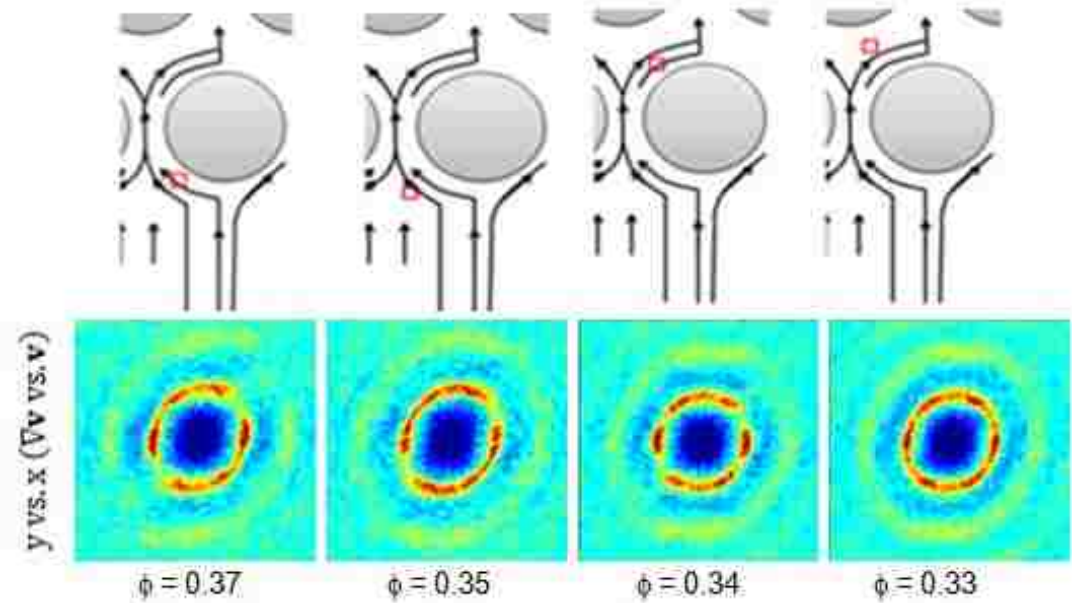

Figure 5.4: *g(r) plots in the y vs. x plane for the upstream and downstream flow cases. The regions of interest in this figure are around the obstacle. The volume fraction of the suspension is low and therefore do not observe much structure.*

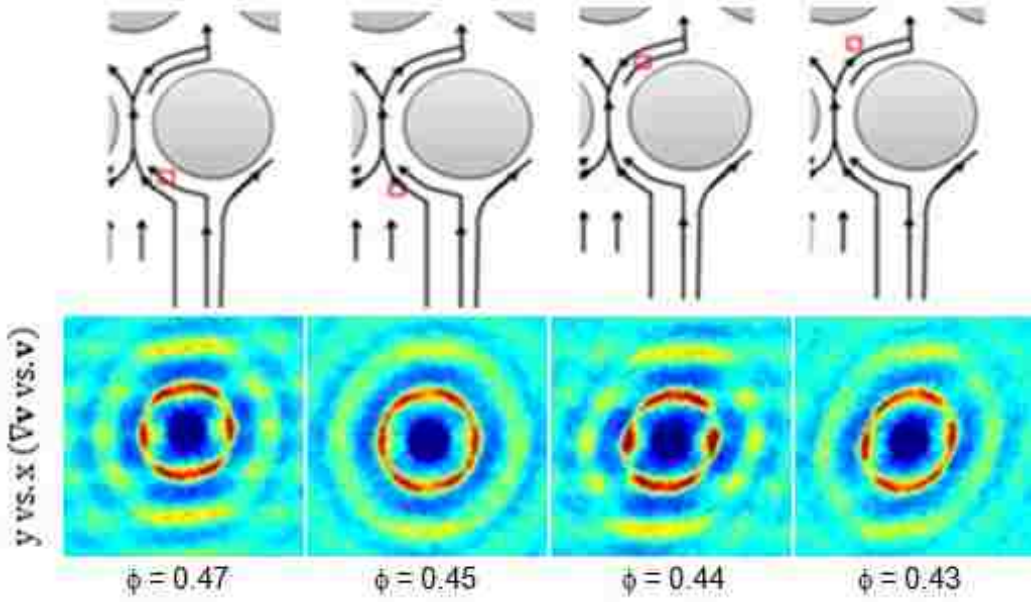

Figure 5.5: *g(r) plots in the y vs. x plane for the upstream and downstream flow cases. The regions of interest in this figure are around the obstacle. The volume fraction of the suspension is high and we observe more structure closer to the post than away.*

5.2.3: Suspension Microstructure between the posts

Next, I would like to focus on the structure observed between two posts for the high volume fraction case. Chapter 4 of this thesis discussed boundary effects in detail, and therefore, for the rest of this chapter, I would like to focus on how boundary effects come into play between two posts in a porous medium. The region of interest here is shown in Figure 5.6.

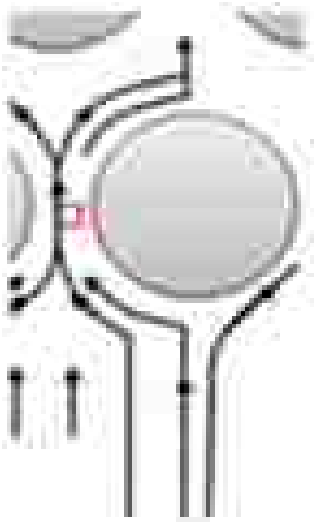

Figure 5.6: *Region investigated between the two posts is shown in red. The approximate directions of the flow streamlines are shown. At this point, we can assume the extensional rate to be zero.*

The region highlighted in Figure 5.6 above is where all flows converge and we can safely assume the extension component of flow to be zero at this point. We assume that the flow is completely driven by shear from the walls of the posts. Therefore, I will be investigating the structures at this point and also deduce the rheology and establish a relationship with the detail we obtained in Chapter 4 of this thesis. First we investigate the g(r) plots obtained for a volume fraction of $\phi = 0.46$. See figure 5.7.

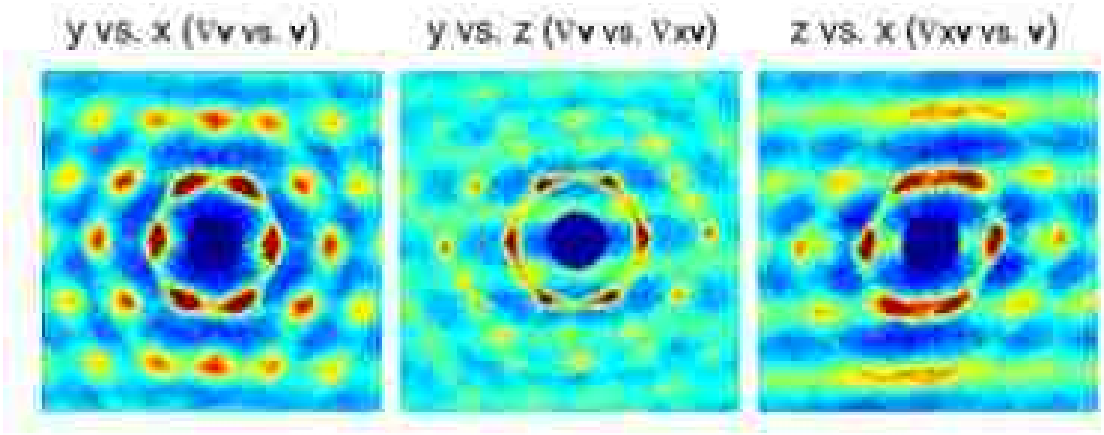

Figure 5.7: *g(r) plots representing the three different planes for the structure between the two posts.*

We clearly observe high order in structure in all three planes of the g(r). Flows converge to this point, and results in a highly ordered structure. We could also assume that the extension component of flow is zero at this point because there is no extension or compression flow component at this point in the porous medium. The hexagonal nature of the particles is observed in the y vs. x axis indicating a crystalline nature of particle arrangement. We also observe particle layering behavior in the z vs. x plane. Note that this behavior is similar to the results that we obtained in chapter 4 when a suspension flows near a smooth boundary. The post in this case can be considered as a smooth boundary in which wall effects can come into play. Therefore, we investigate the viscometric functions as before. See Figure 5.8.

Figure 5.8 shows the relative viscosity as well as the First Normal stress difference plotted as a function of distance from the wall of the post. We observe a similar trend as seen in our chapter 4 results. First we notice a lowered viscosity due to the depletion effects caused by the wall. This is evident till about 9 μm away from the wall of the post. The first normal stress difference is also positive only till about 6 μm away from the wall. Shear driven suspensions of this nature are known to have a negative N1 due to the compressive nature in shearing suspensions (Foss and Brady 2000). Yet, we see that due to the boundary effects, the first normal stress difference is positive closer to the wall. We suggest that due to the wall boundaries, the particles push against each other that result in a positive N1. Therefore, these new results also confirm our results in Chapter 4 under which boundary effects should be considered dominant.

Some may argue that could this ordering be purely a result of boundary effects? It is understood that flows converge into this point, which results in a higher local concentration of particles between the two posts. With higher local concentration, the particles order themselves as shown in the g(r) plots in a hexagonal nature. Based on the streamlines that we observe through the confocal microscope, we see that the particles had a linear motion in the direction of flow, free from any collisions from the boundaries of the posts. Particle chaining is also observed in the velocity-vorticity plane (the plane parallel to the wall of the post). And thus, if we assume pure shear flow at this point, the viscometric calculations closely match with the results we obtained in Chapter 4 discussing with regard to boundary effects. Therefore, it is clear that the boundary effects come into play dominantly to result in this order of suspension structure even when it comes to real process flows such as flows in porous networks.

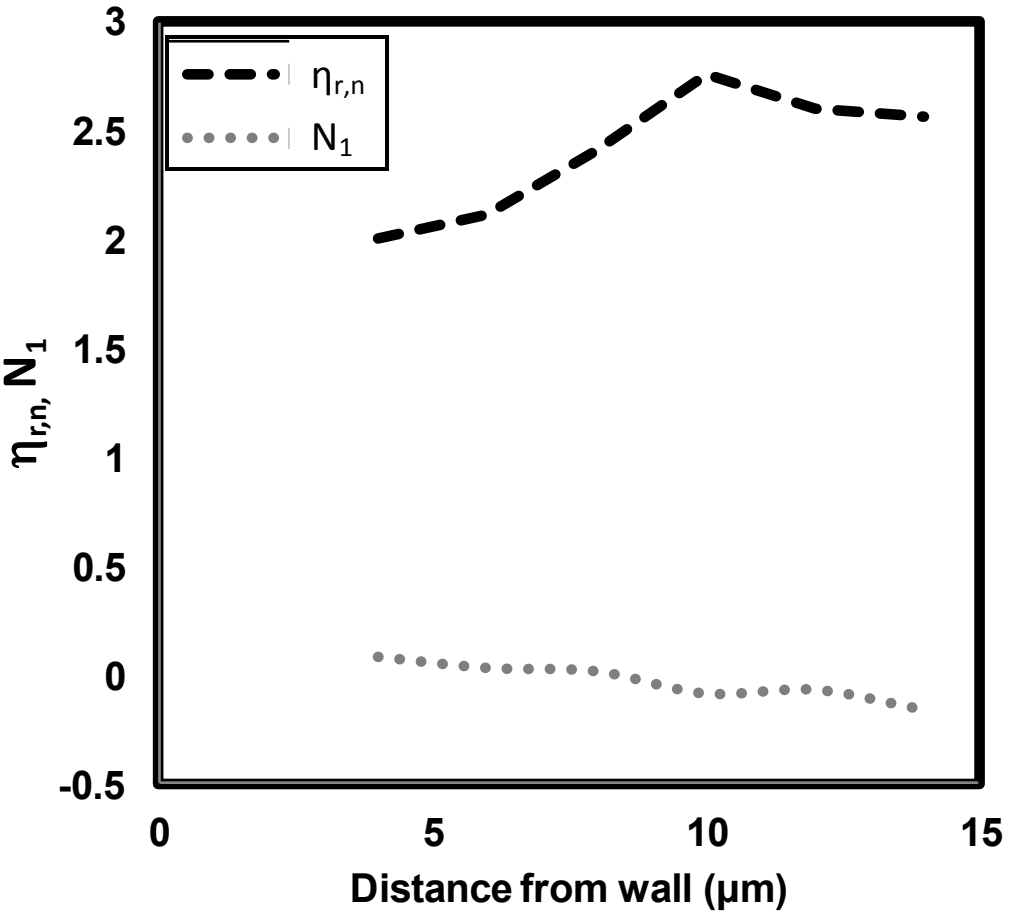

Figure 5.8: *Scaled Relative Viscosity (ηr) and First Normal stress difference (N_1) plotted as a function of distance from wall (post).*

5.3: Conclusions

A particle migrating in a porous medium is subjected to inter-particle forces, and forces induced by the pore surface and fluid. Therefore, migrating particles deviate from streamlines resulting in a mixed flow behavior. This directly affects suspension microstructure. We have investigated how the structure evolves upstream and downstream in a well structured porous medium. We observe an anisotropic structure in the velocity-velocity gradient axis around the posts indicating shear flow. But this is not the case for all structures across the medium suggesting a mixed flow behavior. When suspensions of high solid volume fraction are flowed in the medium, more structure is observed. The structure between two posts shows high order, almost suggesting a crystalline nature having a hexagonal ordered structure. This is due to the convergence of flows at this point and due to the dominant boundary effects. Investigation of viscometric functions suggests a similar behavior as our Chapter 4 results discussing about boundary effects.

CLSM provides a useful technique in investigating microstructure in real applications such as in a porous medium. The work outlined in this chapter also suggests that boundary effects can play a major role in real process flows.

Chapter 6

Summary and Future Directions

6.1: Summary

This dissertation experimentally explores suspension microstructure of flowing suspensions to investigate the shear thickening phenomenon and boundary effects. Direct visualization of the microstructure is rendered possible using Confocal Microscopy. Previous work initiated by Dr. Gao and Dr. Xu from the Gilchrist group implemented this experimental technique to provide accurate and detailed results of microstructure that can strongly agree with simulation results. By making necessary corrections to the experimental technique, they were able to obtain results that agree with theoretical predictions and computations. Stokesian dynamics simulations show anisotropy of a flowing suspension with increasing Pe in the velocity-velocity gradient plane. This trend was confirmed using CLSM and further studies with regard to hydrodynamic and electrostatic effects were investigated by our group previously.

The formation of hydroclusters with increasing *Pe* is the well accepted mechanism behind shear thickening. Essentially the brief mechanism behind the hydrocluster formation is the shear induced self organization of colloidal microstructure

that forms clusters of particles under the influence of short ranged lubrication forces. We have showed that the number of hydrocluster formation increases with *Pe* in an exponential manner. The dominance of 5-8 particle clusters causes the onset of shear thickening behavior in our experiments. In addition, the hydroclusters tend to orient more towards the 45 ° and 135° axis in the velocity-velocity gradient plane.

Shear thickening can be considered as a phenomenon that occurs in the bulk suspension. The question that arises here is what really happens closer to the boundaries when a suspension flows through a microchannel? Results following suspension microstructure indicate that boundary effects can be prominent near the walls even up to about 6 microns away from the wall. Smooth walls influences in particle chaining in the direction of flow. When roughness is introduced on to the boundaries, wall slip is reduced and thus, disrupts local structure of the flowing suspension. Therefore, particle chaining is eliminated and a purely anisotropic structure is observed even near the rough boundary. Smooth boundaries also cause a significant amount of depletion that result in a reduction of viscosity. We also believe that the addition of roughness onto walls reduce the lubrication layer thickness of the solvent layer formed between the boundary and the particle closest to the boundary. Since slip velocity is proportional to this lubrication layer thickness, we have showed that the reduction in this thickness is achieved by the addition of rough walls and hence reduces slip velocity.

As an extension to boundary effects, this thesis also investigated how boundary effects come into play in real process flows such as in porous media. This effect is evident between the boundaries of two posts where flows converge and results in order

due to the boundary effects. A particle migrating in a porous medium is subjected to inter-particle forces, and forces induced by the pore surface and fluid. Therefore, migrating particles deviate from streamlines resulting in a mixed flow behavior. This directly affects suspension microstructure. We have investigated how the structure evolves upstream and downstream in a well structured porous medium using CLSM.

6.2: Future Directions

With more studies geared toward particle level simulations, CLSM has provided to be a very useful experimental technique to obtain suspension microstructure and deduce the rheology based on near-field approximations. It is always preferential to have rheo-optics measurements simultaneously to provide more objective mechanical results. Therefore, an upgrade to the current system can be mounting a mechanically driven shear cell to the confocal microscope which carries out simple shear, oscillatory shear, flow cessation and force/torque measurement. With this setting, factors like concentration and shear rate can be individually controlled and rheological effects like shear-thinning/thickening are readily captured with their corresponding microstructures.

Other possible directions could be the investigation of binary suspensions and other suspending fluids such as viscoelastic fluids and boger fluids. The initial ground work for this work was performed by me during my research work, but was not completely understood. Therefore, let me briefly outline the observed phenomena here and can be considered a future direction for my work.

Due to the changes in hydrodynamic interactions, the formation of strings or necklaces of particles in sheared viscoelastic fluids has been reported long ago. Michele et al. (1977) were the first to report results of string formation in what were described to be ‘monolayers’ of semi-dilute suspensions of glass spheres in viscoelastic media, in the case of both oscillatory shear flow and pipe flow. Giesekus pointed out that this phenomenon was governed by the normal stress differences and furthermore showed that in the case of a bi-disperse suspension, the particles segregate and form separate

strings, sorting themselves according to their size (Giesekus 1981, 1978). Scirocco et al. 2004, Pasquino et al. 2010 reported flow induced strings in viscoleastic fluids. When viscoelasticity was introduced on to our suspensions, we noticed particle chaining as well, but it was unclear whether it was a boundary effect or due to viscoelasticity itself. Therefore, certainly more work can be done in this field using our CLSM system, by looking at the effect from shear rate, polymer concentration, polymer weight etc.

I would also like to mention that in order to understand the effect of polymer on particle chaining, I also performed a series of experiments using Lambda DNA since DNA is known to behave as a polymer. Interestingly, we observed the DNA to always have an elongated nature closer to the walls and a coiled state at the center of the channel even though the shear rate was approximately constant throughout the channel. See figures 6.1 and 6.2. Therefore, a possible future direction would be to investigate this effect further using our CLSM system.

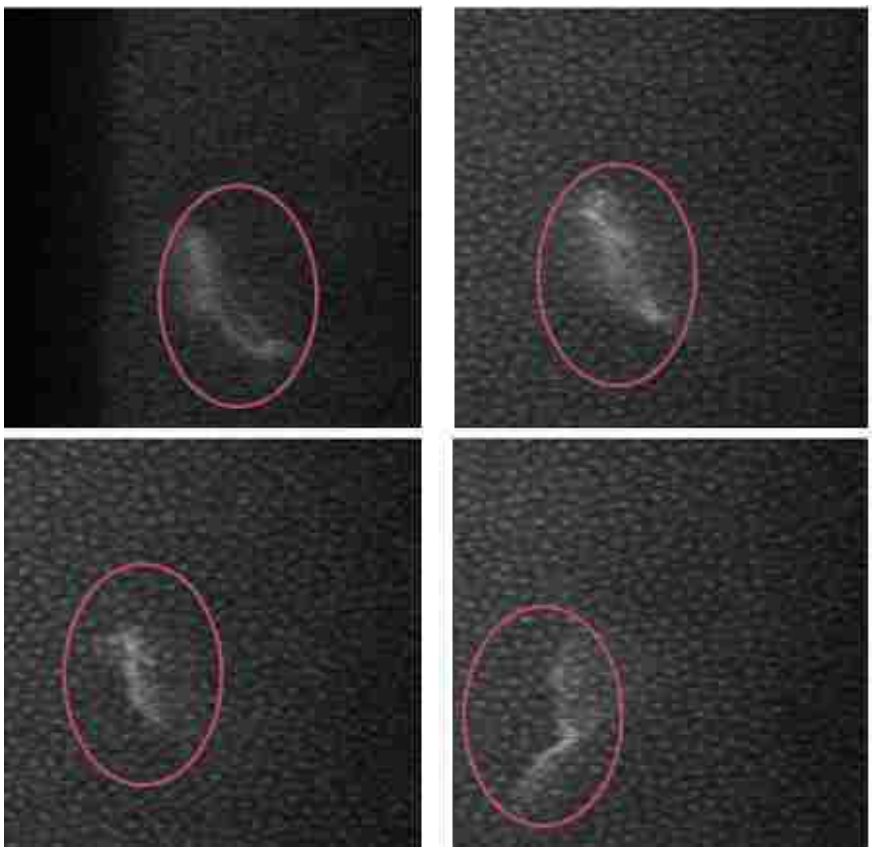

Figure 6.1: *Fluorescent Lambda DNA observed near the channel walls of the confocal microscope. The DNA observed closer to the walls always had a stretched state as seen in this figure.*

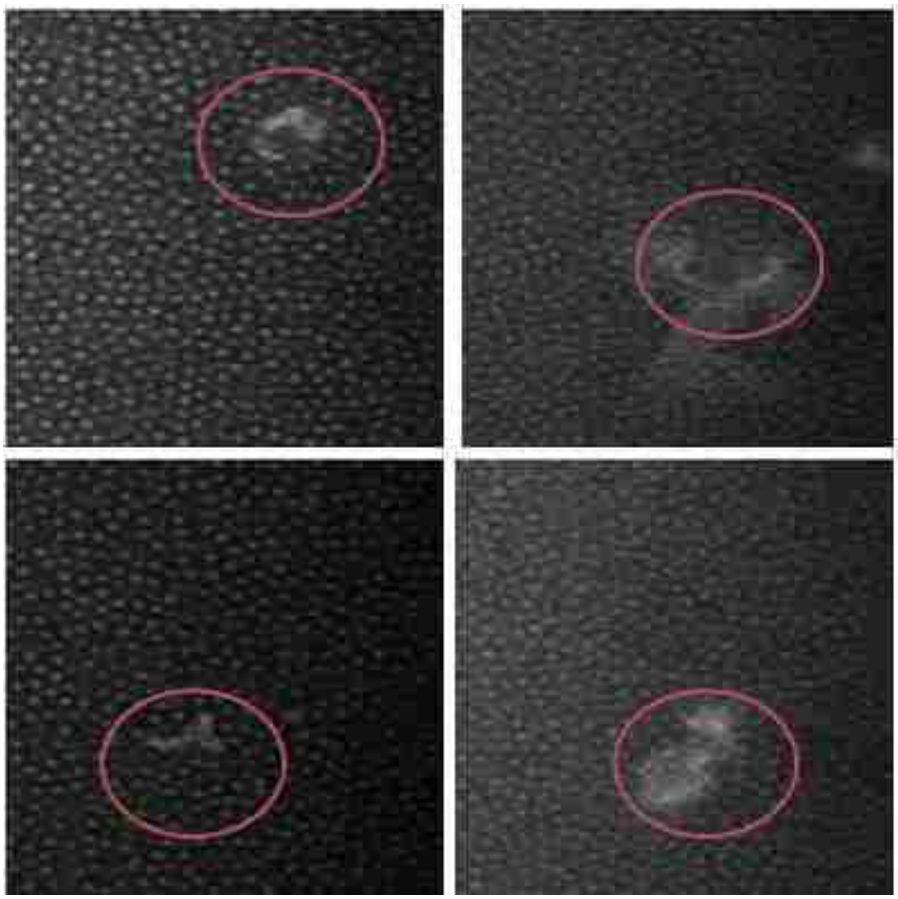

Figure 6.2: *Fluorescent Lambda DNA observed in the center of the channel of the confocal microscope. The DNA observed in the center of the channel always had a coiled state as seen in this figure.*

Bibliography

Barnes, H. A., ‘‘A review of the slip wall depletion of polymer solutions, emulsions and particle suspensions in viscometers: Its cause, character and cure,’’ *J. Non-Newtonian Fluid Mech*. 56, 221–251 (1995)

Barnes, H.A., “Shear thickening (Dilatancy) in suspensions of nonaggregating solid particles dispersed in Newtonian liquids”, *Journal of Rheology,* 33, 329-366 (1989)

Barnes, H. A., ‘‘The yield stress, a review or, everything flows?’’ *J. Non-Newtonian Fluid Mech.* 81, 133178 (1999)

.

Barnes, H. A. and Q. D. Nguyen, ‘‘Rotating vane rheometry—A review,’’ *J. Non-Newtonian Fluid Mech*. 98, 1–14 (2001)

Ballesta, P., Petekidis, G., Isa, L., Poon, W. C. K., and Besseling, R., “Wall slip and flow of concentrated hard sphere colloidal suspensions”, *J. Rheology,* 56, 1005 (2012)

Batchelor, G. K., “Brownian diffusion of particles with hydrodynamic interaction.” *J. Fluid Mechanics*. 74, 1–29 (1976)

Batchelor, G. K. & Green, J. T., “The determination of the bulk stress in a suspension of spherical particles to order c2.” *J. Fluid Mechanics*. 56, 401–427 (1972)

Batchelor, G. K. & Green, J. T., “The hydrodynamic interaction of two small freely-moving spheres in a linear flow field.” *J. Fluid Mechanics*. 56, 375–400 (1972)

Bender, J., Wagner, N.J., “Optical Measurement of the contribution of colloidal forces to the rheology of concentrated suspensions”, *Journal of Colloid and Interface Sci,* 172, 171-184 (1995)

Bender, J., Wagner, N.J., “Reversible Shear thickening in monodisperse and bidisperse colloidal dispersions”, *Journal of Rheology,* 40, 899-916 (1996)

Besseling, R., Weeks, E.R., Schofield, A.B., Poon, W.C.K., “Three-dimensional imaging of colloidal glasses under steady shear”, *Phys. Rev. Lett.* 99, 028301 (2007)

Besseling, R., Isa, L., Weeks, E.R., Poon, W.C.K., "Quantitative imaging of colloidal flows", *Adv. Coll. Int. Sci.* 146, 1–17 (2009)

Besseling, R., Isa, L., Ballesta, P., Petekidis, G., Cates, M.E., Poon, W.C.K., "Shear banding and flow-concentration coupling in colloidal glasses", *Phys. Rev. Lett.* 105, 268301 (2010)

Boersma, W.H., Baets, P.J.M., Laven, J., "Time dependent behavior and wall slip in concentrated shear thickening dispersions", *Journal of Rheology,* 35, 1093-1120 (1991)

Boersma, Laven, J., Stein, H.N., "Computer Simulations of Shear thickening of concentrated dispersions", *Journal of Rheology,* 39, 841-860 (1991)

Brady, J.F. & Morris, J. F., "Microstructure of strongly sheared suspensions and its impact on rheology and diffusion." *J. Fluid Mechanics*. 348, 103–139 (1997)

Brady, J. F. & Bossis, G., "The rheology of concentrated suspensions of spheres in simple shear flow by numerical simulation." *J. Fluid Mechanics*. 155, 105–129 (1985)

Brady, J. F. & Bossis, G., "Stokesian Dynamics." *Annu. Rev. Fluid Mech.* 20, 111–157 (1988)

Bricker, J. M. & Butler, J. E., "Oscillatory shear of suspensions of noncolloidal particles." *J. Rheology.* 50, 711–728 (2006)

Butera, R.J., Wolfe, M.S., Bender, J. & Wagner, N.J., "Formation of a highly ordered colloidal microstructure upon flow cessation from high shear rates." *Phys. Rev. Lett*. 77, 2117–2120 (1997)

Brady, J. F., and Morris, J.F., "Microstructure of strongly sheared suspensions and its impact on rheology and diffusion" *J. Fluid Mech.,* vol. 348, 103-139 (1997)

Comba, S., Dalmazzo, D., Santagata, E., "Rheological characterization of xanthan suspension of nanoscale iron for injection in porous media", *Journal of Hazardous Materials,* 185, 598-605 (2011)

Choi, Y.J., Park, J.Y., Kim, Y.J., "Flow Characteristics of microbubble suspensions in porous media as an oxygen carrier", *Clean Soil Air Water,* 36, 59-65 (2008)

Chow, A.W., Sinton, S.W., Iwamiya, J.H. & Thomas, T.S. "Shear induced particle migration in couette and parallel-plate viscometers: Nmr imaging and stress measurements." *Phys. Fluids* 6, 2561–2576 (1994)

Cohen, I., B. Davidovitch, A. B. Schofield, M. P. Brenner, and D. A. Weitz, “Slip, Yield, and Bands in Colloidal Crystals under Oscillatory Shear”, *Phys. Rev Lett*. 97, 215502 (2006)

Datta, S., Redner, S., “Gradient Clogging in Depth Filtration” *Phys. Rev. E,* 58, 2 (1998)

Dhaene, P., Mewis, J., Fuller, G.G., “Scattering dichroism measurements of flow induced structure of a shear thickening suspension”, *Journal of Colloid & Interface Sci.* 156, 2, 350-358 (1993)

Drazer, G., Koplik, J., Khusid, B. & Acrivos, A., “Microstructure and velocity fluctuations in sheared suspensions.” *J. Fluid Mech*. 511, 237–263 (2004)
Einstein, A. “Eine neue, bestimmung der molecule-dimesioned. *Ann. Physik.* 19, 289-306 (1906)

Einstein, A. “Berichtigung zu meiner arbeit: Eine neue, bestimmung der molecule-dimesioned” *Ann. Physik 96*, 562-568 (1911)

Egres, R.G., Wagner, N.J., “The rheology and microstructure of acicular precipitated calcium carbonate colloidal suspensions through the shear thickening transition”, *Journal of Rheology,* 49, 719-746 (2005)

Foss, D., Brady, J.F., “Structure, Diffusion and Rheology of brownian suspensions by Stokesian dynamics simulations”, *Fluid Mech.,* vol 407, pp 167-200 (2000)

Frank, M., Anderson, D., Weeks, E.R., and Morris J.F., “Particle migration in pressure-driven flow of a Brownian suspension,” *Fluid Mech*., 493, 363-378 (2003)

Gadala-Maria, F. & Acrivos, A., “Shear-induced structure in a concentrated suspension of solid spheres.” *J. Rheology* 24, 799–814 (1980)

Gao, C., and Gilchrist, J.F., "Shear-Induced Particle Migration in 1D, 2D, and 3D Flows", *Physical Review E*, 77, 025301 (2008)

Gao, C., Xu, B,. and Gilchrist, J.F., "Mixing and segregation of microspheres in microchannel flows of mono- and bi-dispersed suspensions", *Physical Review E*, 79, 036311 (2009)

Gao, C., Kulkarni, S.D., Morris, J.F., and Gilchrist, J.F., "Direct investigation of anisotropic suspension structure in pressure-driven flow", *Physical Review E*, 81, 041403 (2010)

Giesekus, H., “Die bewegung von teilchen in stromungen nichtnewtonscher flussigkeiten. Z. Angew.” *Math. Mech.,* 58:T26-T37 (1978)

Giesekus, H., “Some new results in suspension rheology, F. Wendt (Ed.), Lect. Ser. 1981-1988, Non-Newt. *Flows, Von Karman Inst. for Fl. Dynamics, Rhode Saint Genese, Belgium* (1981)

Goldztein, G.H. and Santamarina, J.C. “Suspension extraction through an opening before clogging”, *Applied Phys. Letters,* Vol 85-20 (2004)

Gopalakrshnan, V., Zukoski, C.F., “Effect of attractions on shear thickening in dense suspensions”, *Journal of Rheology,* 48, 6, 1321-1344 (2004)

Gruesbeck, C., Collins, R.E., “Entrainment and Deposition of particles in Porous Media”, *SPEJ* 22, 6 (1982)

Hoffman, R.L., “Explanations for the cause of shear thickening in concentrated colloidal suspensions”, *Journal of Rheology*, 42, 111-123 (1998)

Hsu, T.T., Walker, T.W., Frank, C.W., Fuller, G.G., “Role of fluid elasticity on the dynamics of rinsing flow by an impinging jet”, *Phys. Fluids,* 23-033101 (2011)

Husband, D.M., and Gadala-Maria, F., “Anisotropic particle distribution in dilute suspensions of solid spheres in cylindrical Couette flow”, *J. Rheol*., 51:95–110, (1987)

Isa, L., Besseling, R., Poon, W.C., “Shear zones and wall slip in the capillary flow of concentrated colloidal suspensions”, *Phys. Rev. Letters,* 99(11): 119901 (2007)

Juarez, G. and Arratia, P., “Extensional rheology of DNA suspensions in microfluidic devices”, *Soft Matter,* 7, 9444 (2011)

Kalyon, D.M., “Apparent slip and viscoplasticity of concentrated suspensions”, *Journal of Rheology,* 49 (3), 621-640 (2005)

Kampel, G., Goldztein, G.H, and Santamarina, J.C., “Particle transport through porous media: the role of inertial effects and path tortuosity in the velocity of the particles”, *Applied Physics Letters,* Vol 95-194103 (2009)

Kampel, G., Goldztein, G.H, and Santamarina, J.C., “Plugging of porous media and filter: Maximum clogged porosity”, *Applied Physics Letters,* Vol 92-184101 (2008)

Kim, J. Y., Ahn, S. W., Lee, S. S., and Kim, J. M., "Lateral Migration and focusing of colloidal particles and DNA molecules under viscoelastic flow", *Lab Chip,* 12, 2807-2814 (2012)

Kriger, I.M., "Rheology of Monodisperse lattices" *Adv Colloid Interface Sci, 3, 111-136 (1972)*

Laun, H.M., "Rheological properties of aqueous polymer dispersions", *Angew. Makromol Chem.,*123, 335 (1984)

Laun, H.M., Bung, R., Hess, S., "Rheological and Small Angle Neutron scattering Investigation of shear induced particle structures of concentrated polymer dispersions submitted to plane poiseuille and couette flow" *Journal of Rheology,* 36, 743 (1992)

Lee, Y.S., Wagner, N.J., "Dynamic properties of shear thickening colloidal suspensions", *Rheologica Acta,* 42, 199-208 (2003)

Leighton, D.T. & Acrivos, A., "Measurements of the shear induced coefficient of self-diffusion." *J. Fluid Mech*. 181, 415–439 (1987)

Leighton, D.T. & Acrivos, A.,"The shear-induced migration of particles in concentrated suspensions." *J. Fluid Mech*. 181, 415–439 (1987)

Lyon, M.K. & Leal, L.G., "An experimental study of the motion of concentrated suspensions in twodimensional channel flow. i. monodisperse systems." *J. Fluid Mech*. 363, 25–56 (1998)

Maranzano, B.J., Wagner, N.J., "The effects of interparticle interactions and particle size on reversible shear thickening Hard sphere colloidal dispersions", *Journal of Rheology,* 45, 1205-1222 (2001)

Maranzano, B.J., Wagner, N.J., "Flow small angle neutron scattering measurements of colloidal dispersion microstructure evolution through the shear thickening transition", *Journal of Chemical Physics,* 117, 10291-10302 (2002)

Meeker, S. P., W. C. K. Poon, and P. N. Pusey, "Concentration dependence of the low-shear viscosity of suspensions of hard-sphere colloids", *Phys. Rev. E*, 55, 5718—5722 (1997)

Meeker, S. P., R. T. Bonnecaze, and M. Cloitre, "Slip and Flow in Soft Particle Pastes", *Phys. Rev. Lett*., 92, 198302 (2004)

Meeker, S. P., R. T. Bonnecaze, and M. Cloitre, "Slip and flow in pastes of soft particles: Direct observation and rheology", *J. Rheol*. 48, 1295–1320 (2004)

Melrose, J.R., VanVliet, J.H., Ball, R.C., "Continuous shear thickening and colloid surfaces", *Phys. Rev. Letters,* 77, 22, 4660-4663 (1996)

Melrose, J.R., Ball, R.C., "Continuous shear thickening transitions in model concentrated colloids- The role of interparticle forces", *Journal of Rheology,* 48, 5, 937-960 (2004)

Meyer, A., Marshall, A., Bush, B.G. and Furst, E.M., "Laser Tweezer microrheology of a colloidal suspension", *J. Rheology,* 50, 77 (2006)

Mewis, J. & Wagner, N. J., "Current trends in suspension rheology." *J. Non- Newtonian Fluid Mech.* 157, 147–150 (2009)

Mewis, J. and Wagner, N.J., "Colloidal Suspension Rheology", *Cambridge University Press, (*2012)

McCormick, R.M., Nelson, R.J., Alonso-Amigo, M.G., Benvegnu, D.J., and Hooper, H.H. "Microchannel Electrophoretic Separations of DNA in Injection-Molded Plastic Substrates,". *Analytical Chemistry*., 69(14), 2626-2630 (1997)

Michele J., Patzold R., Donis R., "Alignment and aggregation effects in suspensions of spheres in non-newtonian media." *Rheol. Acta*, 16:317-321 (1977)

Mooney M., "Explicit formulas for slip and fluidity*", J. Rheol.* 2 , 210–222 (1931)

Morris, J.F., "A review of microstructure in concentrated suspensions and its implications for rheology and bulk flow." *Rheol. Acta* 48, 909–923 (2009)

Morris, J.F. & Boulay, F., "Curvilinear flows of noncolloidal suspensions: The role of normal stresses." *J. Rheol*. 43, 1213–1237 (1999)

Morris, J.F., and Katyal, B., "Microstructure from simulated Brownian suspension flows at large shear rate", *Physics of Fluids.*, vol 14, 16 (2002)

Muangnapoh, T., Weldon, A.L., Gilchrist, J.F., "Enhanced monolayer deposition via vibration-assisted convective deposition", *Applied Physics Letters*, 103, 181603 (2013)

Muecke, T.W., "Formation fines and their factors controlling flows in Porous media" *JPT* 31, 1 (1979)

Nott, P. R. and J. F. Brady, ‘‘Pressure-driven flow of suspensions: simulation and theory,’’ *J. Fluid Mech.* 275, 157 199, (1994)

Parsi, F. & Gadala-Maria, F., “Fore-and-aft asymmetry in a concentrated suspension of solid spheres.” *J. Rheology*. 31, 725–732 (1987)

Pasquino, R., Snijkers, F., Grizzuti, N., Vermant, J., “Directed Self-Assembly of Spheres into a Two Dimensional Colloidal Crystal by Viscoelastic Stress”, *Langmuir*, 26 (5), 3016-3019 (2010)

Phung, T. N., ‘‘Behavior of concentrated colloidal dispersions by Stokesian dynamics,’’ *Ph.D. thesis*, California Institute of Technology (1993)

Phung, T.N., Brady, J.F., Bossis, G., “Stokesian Dynamics simulation of Brownian suspensions”, *Journal of Fluid Mech.* 313, 181-207 (1996)

Ramachandran, A. and Leighton, D.T., “Viscous re-suspension in a tube: The impact of secondary flows resulting from second normal stress differences.” *Phys. Fluids*, 19:053301, (2007)

Rampall, I., Smart, J.R., Leighton, D.T., “The influence of surface roughness on the particle-pair distribution function of dilute suspensions of non-colloidal spheres in simple shear flow” , *Journal of Fluid Mech*., 339:1–24, (1997)

Roberts, M.A., Rossier, J.S., Bercier, P., and Girault, H., “UV Laser Machined Polymer Substrates for the Development of Microdiagnostic Systems,” *Analytical Chemistry.*, 69(11), 2035-2042 (1997)

Sanderson, S.L., Cheer, A.L., Goodrich, J.S.,Graziano, J.D., Callan, G., “Cross Flow feeding in Suspension Feeding Fishes”, Nature (London), 412, 6845 (2001)

Scirocco R., Vermant J., Mewis J., “Effect of the viscoelasticity of the suspending fluid on structure formation in suspensions”, *J. Non-Newtonian Fluid Mech*., 117:183-192 (2004)

Seth, J.R., Cloitre, M., Bonnecaze, R.T., “Influences of short range on wall slip in microgel pastes”, *J. of Rheology*, 52, 1241-1268 (2008)
Sierou, A. & Brady, J.F., “Rheology and microstructure in concentrated noncolloidal suspensions.” *J. Rheology*. 46, 1031–1056 (2002)

Sherard, J.L., Dunnigan, L.P., Talbot, J.R., “Basic Properties of Sand and Gravel Filters” *J. Geotech. Engrg*. **110**, 6 (1984)

Stickel, J.J. & Powell, R.L., “Fluid mechanics and rheology of dense suspension.” *Annu. Rev. Fluid Mech.* 37, 129–149 (2005)

Stickel, J.J., Phillips, R.J., Powell, R.L., “Application of a constitutive model for particulate suspensions: Time dependent viscometric flows”, *J. Rheology*, Vol 51, 1271 (2007)

Soltani, F., and U. Yilmazer, ‘‘Slip velocity and slip layer thickness in flow of concentrated suspensions,’’ *J. Appl. Polym. Sci*. 70, 515–522 (1998)

Valdes, J.R. and Santamarina, J.C., “Clogging: bridge formation and vibration based destabilization”, *Can. Geotech. J*. **45**: 177–184 (2008)

Valdes, J.R. and Santamarina, J.C., “Particle clogging in radial flow: Microscale Mechanisms”, *SPE Journal*. (2006)

Vand, V., “Viscosity of solutions and suspensions. I. Theory”, *J. Phys. Colloid Chem*. 52, 277–314 (1948)

Vasin, S.I., “Cell models of porous media composed of impenetrable spherical particles”, *Colloid Journal*, 72, 307-314 (2010)

Wagner, N.J. & Brady, J.F., “Shear thickening in colloidal dispersions.” *Phys. Today* 62, 27–32 (2009)

Walls, H. J., Caines, S. B., Sanchez, A. M., Khan, S. A., “Yield stress and colloidal phenomena in colloidal silica gels”, *J. Rheology,* 47, 847 (2003)

Wang, W., Gu, B., Liang, L., Hamilton, W., “Fabrication of Two-Three Dimensional Silica nanocolloidal particle arrays”, *Journal of Physical Chemistry,*107, 3400-3404 (2003)

Wang, B., Weldon, A.L., Kumnorkaew, P., Xu, B., Gilchrist, J.F., and Cheng, X., "Effect of Surface Nanotopography on Immunoaffinity Cell Capture in Microfluidic Devices", *accepted in Langmuir*

Whitesides, G M., “The origins and the future of microfluidics,” *Nature (London, United Kingdom).,* 442(7101), 368-373 (2006)

Xia, Y., and Whitesides, G.M., “Soft lithography,” Annual *Review of Materials Science.*, (1998)

Xu. B., and Gilchirst, J.F., “Microstructure of sheared monosized colloidal suspensions resulting from hydrodymanic and electrostatic interactions”, *Journal of Chem. Physics*, 140, 204903 (2014)

Yoshimura, A. and Prud’homme, R.K., “Wall Slip corrections for Couette and Parallel disk viscometers”, *Journal of Rheology,* 32, 53 (1988)

Zarraga, I. E., Hill, D. A. & Leighton, D.T., “The characterization of the total stress of concentrated suspensions of noncolloidal spheres in Newtonian fluids.” *J. Rheology.* 44, 185–220 (2000)

Zhang, J.H., Zhan, P., Wang, Z.L., Zhang, W.Y., Ming, N.B., “Preparation of monodisperse silica particles with controllable size and shape”, *J. Mater. Res.,* Vol. 18, No. 3, 649-953 (2003)

Zhang, J., T. P. Lodge, and C. W. Macosko, “Interfacial morphology development during a PS/PMMA polymer-polymer coupling reaction,” *Macromolecules*, 38, 6586–6591 (2006)

Zhao, R., and C. W. Macosko, “Slip at polymer-polymer interfaces: rheology measurements on coextruded multilayers,” *J. Rheol*. 46, 145–167 (2002)

Vita

M. Tharanga D Perera
484-522-8932 (Cell)
mtp210@lehigh.edu, damayanthap@gmail.com

Work Address (Preferred Contact):
111 Research Drive
Department of Chemical Engineering
Bethlehem, PA 18015
18015

Current Address:
7 Duh Drive
Apt 112
Bethlehem, PA

EDUCATION

Lehigh University — Bethlehem, PA
Doctoral Candidate, P.C Rossin Fellow, Chemical Engineering — *Ph.D*
Advisor: Prof. James F. Gilchrist
Thesis Topic: Suspensions Rheology and Microstructure
GPA: 3.79/4.00

Texas A&M University — College Station, TX
Bachelor of Science, Chemical Engineering — May 2010
Cum Laude, Omega Chi Epsilon Honor Society
Process Safety Engineering Certificate
Overall GPA: 3.55/4.00 Major GPA: 3.66/4.00
100% of education financed through scholarships and part-time employment.

EXPERIENCE

Lehigh University
Doctoral Research/ Research Assistant — Sep 2010 - Current

- Suspensions Rheology, Microfluidic devices, Complex Fluids, Granular Flows, Colloidal Science and Particle Transport, Polymer Behavior in Fluids and Viscoelastic systems
- Techniques include Characterization of materials using Rheometry, Confocal Microscopy and Scanning Electron Microscopy, as well as automated image analysis using IDL, Matlab and ImageJ.

- ❖ Doctoral Coursework included Chemical Reaction Engineering, Transport Processes, Mathematical Methods, Colloidal Science and Surface Chemistry (audited) and Characterization of Complex Fluids (audited)

Teaching Assistant

- ❖ Assisted Professors in Grading Homework for Junior and Senior Level Chemical Engineering Undergraduate Classes
- ❖ Assisted Professors in Instructing the Unit Operations Laboratory for Junior ChE students

Texas A&M University Aug 2007 - April 2010

Supplemental Instructing Leader

- ❖ Worked part-time providing supplemental instruction for Chemistry Freshmen and sophomores
- ❖ Team lead for a group of chemistry instructors in planning, organizing and tutoring students

MacBertan Ltd, Sri Lanka May 2008 - Aug 2008

Intern/Trainee

- ❖ Assisted the Production line in the manufacturing plant of Polyethylene Foam for McFoil, McWrap and McFoam (Polyethylene based products for packaging and heat insulations marketed in Sri Lanka)

AWARDS AND HONORS

- ❖ P.C. Rossin Doctoral Fellow at Lehigh University, 2013-2014
- ❖ Best poster award, Polymer Nanocomposites Conference, Lehigh University, 2013
- ❖ Research highlighted in *Resolve Magazine*, 2013
- ❖ ConocoPhillips SPIRIT Scholar, 2009-2010
- ❖ Safety Engineering Student Scholarship, 2009-2010
- ❖ Rita and Bill Stout Outstanding International Student award at Texas A&M University, 2009
- ❖ Chemical Engineering Departmental Scholarship at Texas A&M University, 2008-2010
- ❖ Distinguished Student Award from the College of Engineering at Texas A&M University, 2007-2010

PUBLICATIONS

Articles in Preparation

- M. T. Perera and J. F. Gilchrist, "Particle chaining and microstructure of concentrated suspensions in model porous media", for submission to *Physical Review E.*
- M.T. Perera and J.F. Gilchrist, "Effect of Smooth and Rough Boundaries on Suspension Microstructure", for submission to *Soft Matter.*

CONFERENCE PRESENTATIONS

Research Presentations

- M.T Perera and J.F. Gilchrist, "Suspension Microstructure in a microporous flow", 66th Annual Meeting of the American Physical Society-Division of Fluid Dynamics, Pittsburgh, PA, November 2013
- M.T. Perera, B. Xu and J.F. Gilchrist, "Direct Investigation of Suspension flow in an Ideal micro-porous medium", 50th Annual Society of Engineering Science, Brown University, Providence, RI, July 2013
- M.T Perera, B. Xu and J.F. Gilchrist, "Suspensions Rheology and Microstructure", Graduate Student Seminar, Lehigh University, May 2013
- M.T. Perera, B. Xu and J.F. Gilchrist, "Direct Investigation of Suspension Structure in simple and complex flows using Confocal Microscopy", 85th Annual Meeting of the Society of Rheology, Pasadena, CA, February 2013

Student Poster Presentations

- M.T Perera, B. Xu and J.F Gilchrist, "Direct Investigation of Suspension structure under Hydrodynamic, Electrostatic and Viscoelastic effects", Emulsion Polymers Institute Annual Review Meeting, Lehigh University, Bethlehem, PA, May 2013
- M.T Perera, B. Xu and J.F Gilchrist, "Direct Investigation of Suspension structure under Hydrodynamic, Electrostatic and Viscoelastic effects", Society of Plastic Engineers- Polymer Nanocomposites Conference, Lehigh University, Bethlehem, PA, March 2013 (best poster award)
- M.T. Perera, B. Xu and J.F. Gilchrist, "Microstructure of Suspension Flow around an obstacle in a well-structured micro-porous medium", Gordon Research Conference on Granular and Granular Fluid Flow, Davidson, NC, July 2012

LEADERSHIP AND ACTIVITIES

- President of the Chemical Engineering Graduate Association at Lehigh University, 2013-2014
- Laboratory Safety Representative, 2012-2013
- Student President of Sri Lankan Students Association at Texas A&M University, 2008-2009
- Vice President of the Badminton Cub at Texas A&M University, 2009-2010
- Student Member of the Society of Rheology, 2013- Current
- Student Member of the American Physical Society, 2011-Current

EXTRA CURRICULAR ACTIVITIES

- Winner for the Pennsylvania State Badminton Tournament in both Singles and Doubles categories, 2013
- Member of the Lehigh Valley Badminton Club
- Member of the Lewis Tennis Center at Lehigh University